

COMPACT POWER CONDITIONING AND RF SYSTEMS FOR A HIGH POWER RF
SOURCE

A Thesis

Presented to

the Faculty of the Graduate School
at the University of Missouri-Columbia

In Partial Fulfillment

of the Requirements for the Degree

Master of Science

by

KEVIN A. O'CONNOR

Dr. Randy Curry, Thesis Supervisor

DECEMBER 2008

© Copyright by Kevin A. O'Connor 2008

All Rights Reserved

The undersigned, appointed by the Dean of the Graduate School, have examined the thesis entitled

COMPACT POWER CONDITIONING AND RF SYSTEMS FOR A HIGH POWER RF
SOURCE

presented by Kevin A. O'Connor, a candidate for the degree Master of Science, and hereby certify that, in their opinion, it is worthy of acceptance.

Dr. Randy Curry

Dr. Robert O'Connell

Dr. Tom Clevenger

This work is dedicated to those whose personal support makes it possible for me to continue in my educational and personal growth. I am especially grateful to my parents, my sisters and their families, Karen Visovsky, and all my close friends for their support and encouragement through this process.

ACKNOWLEDGEMENTS

First, I express my thanks Dr. Randy Curry for the great opportunities and continued support throughout this period of study. Without Dr. Curry's influence, I would not have found this interesting and challenging field of research. I would also like to thank the other committee members, Dr. Robert O'Connell and Dr. Tom Clevenger, for their service on the committee.

I am also grateful for the less formal education gained through working with fellow graduate students. In particular, I owe thanks to Peter Norgard for his patience and willingness to share his own experiences. Russell Burdt, Chris Yeckel, and Jason Smith are all due recognition for their insightful discussions.

I thank Mr. Mark Nichols for his continuous support in the construction of the test bed and experimental testing both in Columbia and Lubbock. Mrs. Linda Macon and Mr. Mike Fulca are appreciated for their aid in procurement and all other administrative processes. I also recognize the contributions of the undergraduate assistants and their willingness to learn and help throughout this project. In particular, I thank Mike Young for his assistance in the beginning stages of construction and experimentation.

TABLE OF CONTENTS

ACKNOWLEDGEMENTS	ii
LIST OF FIGURES	vii
LIST OF TABLES	xii
LIST OF SYMBOLS	xiii
Chapter 1: Introduction	1
1.1 The University Consortium for High Power Microwave Integration.....	1
1.2 Flux Compression Generator	2
1.3 Overview of the Power Conditioning System	4
References for Chapter 1	9
Chapter 2: FCG Simulator	10
2.1 Background.....	10
2.2 FCG Simulator Component Designs	15
2.2.1 Primary Energy Storage.....	15
2.2.2 Magnetic Switches.....	17
2.2.3 Air-Core Inductors.....	23
2.3 FCG Simulator Component Integration.....	25
2.4 FCG Simulator Results	26
2.4.1 PSpice Simulations of the FCG Simulator	26
2.4.2 FCG Simulator Experimental Results.....	31

References for Chapter 2	33
Chapter 3: Spiral-Strip Pulse Transformer	35
3.1 Pulse Transformer Design Constraints	35
3.2 Pulse Transformer Selection.....	37
3.3 Pulse Transformer Design Equations.....	39
3.4 Winding Analysis.....	43
3.5 Analysis of the Step-up Ratio	48
3.6 Pulse Transformer Construction	53
References for Chapter 3	55
Chapter 4: Exploding Wire Fuse.....	56
4.1 Opening Switch Background	56
4.2 Modeling the Dynamic Fuse Resistance.....	58
4.2.1 Action-Dependent Resistivity Equations	58
4.2.2 Fuse Resistance.....	64
4.2.3 Fuse Energy Dissipation	69
4.3 Exploding Wire Fuse Design	73
4.3.1 Fuse Cross-Sectional Area.....	73
4.3.2 Previous Standard for Fuse Length Design	74
4.3.3 Proposed Method for Fuse Length Design	77
4.3.4 Fuse Inductance	85
4.4 Exploding Wire Fuse Construction.....	86

4.5 Crowbar Switch	88
4.5.1 Theory for Use of Crowbar Switch.....	88
4.5.2 Crowbar Switch Implementation	98
References for Chapter 4	99
 Chapter 5: High Voltage RF Source	 101
5.1 High Voltage Capacitor	101
5.1.1 Tri-Plate Capacitor.....	106
5.1.2 Spiral-Strip Capacitor	109
5.1.3 Coaxial Cylindrical Capacitor.....	112
5.2 Aqueous-Electrolyte Load Resistor	115
5.3 Secondary Low Inductance Switch.....	117
References for Chapter 5	119
 Chapter 6: Experimental Results	 120
6.1 Diagnostics.....	120
6.2 Experimental Results of the Power Conditioning System and FCG Simulator....	124
6.2.1 Experimental Results of the Tri-Plate Capacitor and FCG Simulator	125
6.2.2 Experimental Results of the Spiral-Strip Capacitor and FCG Simulator	129
6.2.3 Experimental Results of a Coaxial-Cylinder Capacitor and FCG Simulator	135
6.3 Experiments Results of the Power Conditioning System with FCGs.....	138
6.3.1 Experimental Results with an FCG and Non-Radiating Load.....	140
6.3.2 Experimental Results with an FCG and Dipole Antenna	143

References for Chapter 6	149
Chapter 7: Summary and Conclusions.....	151
APPENDIX A: Equations for Dynamic Resistance Modeling.....	158
A.1 Power Conditioning System with a Resistive Load.....	158
A.1.1 Resistive Load During FCG Operation.....	158
A.1.2 Resistive Load After FCG Operation.....	161
A.1.3 Resistive Load with Stray Inductance After FCG Operation	166
A.2 Power Conditioning System with an RF Source.....	168
References for Appendix A	172
APPENDIX B: Computer Code for Numerical Analyses	173

LIST OF FIGURES

Figure	Page
1. Full power conditioning system and RF systems	5
2. Power conditioning system with resistive load.....	7
3. Schematic of the FCG simulator driving the power conditioning circuit.....	11
4. Example of FCG simulator current in four stages	15
5. The range of primary energy storage in the FCG capacitor bank.....	17
6. Example hysteresis loop of a magnetic material.....	18
7. Simple model of a magnetic switch	21
8. Magnetic switch. White: switch winding. Red: reset winding	23
9. Magnetic switch. White: switch windings. Red: reset windings	23
10. Air core solenoid.....	25
11. FCG simulator.....	26
12. FCG simulator components in foreground	26
13. PSpice schematic for design simulations of the FCG simulator.....	28
14. PSpice output current waveform of FCG simulator driving 1 μ H load.....	29
15. Magnetic switch voltages during FCG simulator operation	30
16. Flux change in magnetic switches	30
17. FCG simulator operation into inductive load with 20 kV initial voltage	32
18. FCG simulator operation into inductive load with 25 kV initial voltage	33
19. Right circular cylinder geometry of conductive windings.....	39
20. Typical primary circuit component arrangement.....	44
21. Simplified circuit with labeled transformer terminals	45

22. Equivalent circuit with voltage polarities before fuse opening	45
23. Equivalent circuit with voltage polarities after fuse opening	46
24. Transformer cross-section of winding orientation and terminal locations	48
25. Power conditioning circuit after FCG operation with transformer T-equivalent	50
26. Power conditioning circuit after FCG operation with ideal transformer coupling	50
27. Peak capacitor voltage for multiple turn ratios	51
28. Spiral-strip pulse transformer	54
29. Transformer with center high voltage output connection	55
30. Illustrative plot of the resistivity rise and fall about the maximum	62
31. Power conditioning system used for numerical simulations.....	64
32. Fuse resistance without restrike	65
33. Fuse current without restrike	66
34. Fuse resistance with restrike	67
35. Fuse current with restrike.....	67
36. Fuse resistance after action limit for different initial fuse resistances.....	69
37. Energy distribution normalized to total source energy	70
38. Energy distribution normalized to peak inductively-stored energy	72
39. Percentage of initially stored energy dissipated in load.....	72
40. Specific energy dissipated in the fuse after the action limit	84
41. Fuse resistance after action limit for minimal length fuse.....	85
42. Central form of the fuse supporting angled fuse wires	87
43. Fuse housing being packed with fine glass beads.....	87
44. Primary circuit with non-negligible stray inductance and crowbar switch.....	89

45. Primary current for multiple primary stray inductance values	91
46. Fuse resistance for multiple primary stray inductance values	92
47. Specific energy dissipated in the fuse after current source operation.....	93
48. Simplified schematics with and without stray inductance	94
49. Fuse voltage after action limit for multiple primary stray inductance values.....	96
50. Electric field across fuse after action limit	97
51. Dependence of resonant frequency and energy storage on capacitance	103
52. Tri-plate capacitor.....	108
53. Tri-plate RF source in oil.....	109
54. Simplified cross-section of winding pattern	110
55. Cylindrical capacitor with axial high voltage connection.....	111
56. Full system load with pulse transformer at upper left.....	112
57. Simplified cross-section representing the coaxial cylinder geometry	112
58. Assembled coaxial cylinder capacitor	114
59. Simple voltage divider for high voltage measurements.....	121
60. Experimental arrangement with diagnostics.....	124
61. Power conditioning system at lower right with FCG simulator at upper left	125
62. Full view of primary current rise and interruption.....	126
63. Detailed view of current interruption by fuse	127
64. Load voltage at time of fuse opening.....	127
65. Load power and energy dissipated at load.....	128
66. Frequency content of load voltage oscillations.....	128
67. Detailed view of primary current waveform.....	131

68. Detailed view of load voltage RF oscillations	132
69. FFT of load voltage RF oscillations.....	133
70. Detailed view of load voltage after dielectric breakdown	134
71. Full view of primary current for the test of coaxial-cylinder RF load.....	135
72. Detailed view of primary current in test of coaxial-cylinder RF load	136
73. Full view of load voltage for coaxial-cylinder RF load.....	137
74. Full view of load voltage for coaxial-cylinder RF load.....	137
75. Frequency content of coaxial cylinder load voltage oscillations	138
76. The power conditioning system, explosives chamber, and receiving antennas.....	139
77. A fuse, packed in sand, is positioned next to the oil bath.....	139
78. Load voltage during fuse operation	141
79. Detailed view of capacitor voltage at time of oil gap closure.....	141
80. Frequency content of capacitor voltage	142
81. Transformer primary current.....	143
82. Detailed view of fuse current and voltage	143
83. Transformer primary and fuse current	145
84. Load voltage from capacitive probe	146
85. Modeled fuse resistance for analysis of peak charging voltage.....	147
86. Simulated peak charging voltage.....	147
87. Load voltage and fuse current.....	148
88. Electric field measured by receiving antenna 5.5 m from dipole antenna [8]	148
89. Frequency content of the received signal [8].....	149
90. Equivalent s-domain circuit for an HPM load during FCG operation.....	159

91. Equivalent s-domain circuit for an HPM load after FCG operation.....	161
92. Equivalent s-domain circuit for an RF load after FCG operation.....	168

LIST OF TABLES

Table	Page
1. Magnetic Core Parameters	22
2. Core Reset Parameters	23
3. Air Core Solenoid Parameters	24
4. Summary of Inductor Values for Simulation of the FCG Simulator	28
5. Terminal Voltages with Respect to Ground.....	47
6. Pulse Transformer Winding Parameters	53
7. Fixed Simulation Parameters	65
8. Parameters for Simulation of Ideal Minimum Fuse Length	83
9. Fuse Parameters for Inductance Calculation.....	86
10. Parameters Used for Stray Inductance Analysis with Equal Energy Storage.....	90
11. Percentage of Inductively-Stored Energy Dissipated in Fuse After Action Limit	93
12. Parameters for Analysis with Equal Peak Currents and Identical Fuse.....	95
13. Fuse Parameters for Analysis with Equal Peak Currents and Identical Fuses.....	95
14. Percentage of Inductively-Stored Energy Dissipated in Fuse After Action Limit	96
15. Energy Stored and Resonant Frequency at Min. and Max. Capacitance.....	104
16. High Voltage Capacitor Parameters.....	108
17. Tri-Plate Shunt Inductance	109
18. Coaxial Cylinder Capacitor Parameters.....	115
19. Parameters for Aqueous-Electrolyte Solutes [14].....	116
20. Typical Secondary Switch Parameters.....	118

LIST OF SYMBOLS

Symbol	Definition	Units
MU	The University of Missouri-Columbia	
TTU	Texas Tech University	
FCG	Flux compression generator	
HPM	High power microwave	
L_{FCG}	The variable inductance of a flux compression generator	[H]
I_{FCG}	The output current of a flux compression generator	[A]
L_{pri}	Self-inductance of the primary transformer winding	[H]
L_{sec}	Self-inductance of the secondary transformer winding	[H]
R_{fuse}	The variable resistance of the exploding wire fuse	[Ω]
S_C	Crowbar switch	
C_S	The capacitance of the secondary circuit	[F]
S_G	Secondary spark gap switch	
L_{shunt}	The inductance of the secondary shunt	[H]
Z_L	The load impedance of the RF source	[Ω]
v_c	The instantaneous voltage across the secondary capacitance	[V]
i_s	The instantaneous current in the secondary circuit	[A]
t	Time	[s]
R_{load}	The impedance of a high power microwave source	[Ω]
Vircator	Virtual cathode oscillator	
PFN	Pulse forming network	
L_1, L_2, L_3, L_4	Inductance of the air-core inductors of the FCG simulator	[H]
L_{S1}, L_{S2}, L_{S3}	Inductance of the magnetic switches of the FCG simulator	[H]
C	Capacitance of the FCG simulator capacitor bank	[F]
$i_{p,m}$	The instantaneous current of the FCG simulator in stage m	[A]
I_m	The FCG simulator current at the beginning of stage m operation	[A]
V_m	The voltage of the FCG simulator primary energy store at the beginning of stage m operation	[V]
W_m	System energy of the FCG simulator	[J]
$L_{eff,m}$	Total FCG simulator circuit inductance during stage m operation	[H]

$L_{S1,sat}, L_{S2,sat}, L_{S3,sat}$	Saturated inductance of the magnetic switches of the FCG simulator	[H]
$L_{S1,unsat}, L_{S2,unsat}, L_{S3,unsat}$	Unsaturated inductance of the magnetic switches of the FCG simulator	[H]
R_m	Total FCG simulator circuit resistance during stage m operation	[Ω]
α_m	The damping factor for stage m operation of the FCG simulator	[Ω /H]
ω_m	The natural resonant frequency during stage m of FCG simulator operation	[rad/s]
$t_{sat1}, t_{sat2}, t_{sat3}$	The saturation time of the FCG simulator magnetic switches	[s]
H	Magnetic field	[A/m]
B	Magnetic flux density	[T]
μ	Permeability	[H/m]
μ_0	Permeability of free space ($4\pi \times 10^{-7}$)	[H/m]
μ_r	Relative permeability	
H_{sat}	Saturation value of the magnetic field	[A/m]
ΔB_{max}	Maximum change in magnetic flux density	[T]
L	Inductance of a solenoid	[H]
N	Number of windings forming a solenoid	
A	Area enclosed by a solenoid	[m ²]
l	Length of a solenoid	[m]
I_{reset}	Minimum current to reset a magnetic core	[A]
l_m	Magnetic path length in a magnetic core	[m]
N_r	Number of reset windings	
r	Average radius of the windings in a spiral-strip transformer winding	[m]
w	Width of foils in a spiral-strip geometry	[m]
t_w	Total thickness of a winding in a spiral-strip geometry	[m]
n_w	Number of turns in a spiral-strip geometry	
n_p	Number of turns of a primary transformer winding	
n_s	Number of turns of a secondary transformer winding	
i	Instantaneous current in a spiral-strip winding	[A]
i_p	Instantaneous primary current in a spiral-strip winding	[A]
i_s	Instantaneous secondary current in a spiral-strip winding	[A]
ϕ	Magnetic flux	[Wb]
λ	Flux linkage in a transformer winding	[Wb]
L	Inductance of a transformer winding	[H]

H_{peak}	The peak magnetic field	[A/m]
v_{tw}	Volume of a transformer winding	[m ³]
W_H	Energy stored in the transformer magnetic field	[J]
L_l	Leakage inductance	[H]
V_{peak}	Maximum voltage across a transformer winding	[V]
E_{max}	Maximum electric field in a transformer winding	[V/m]
N	Number of dielectric sheets	
t_c	Thickness of conducting foil	[m]
t_d	Thickness of dielectric film	[m]
$T1, T2, T3, T4$	Transformer terminals	
I_{pri}	Current in the primary circuit	[A]
I_{sec}	Current in the secondary circuit	[A]
v_{FCG}	Output voltage of the FCG	[V]
v_{pri}	Voltage across the primary winding	[V]
v_{sec}	Voltage across the secondary winding	[V]
v_{fuse}	Voltage across the fuse	[V]
n	Turn ratio	
L_s	Inductance of the secondary winding	[H]
L_p	Inductance of the primary winding	[H]
k	Transformer coupling coefficient	
L_{lp}	Primary leakage inductance	[H]
L_{ls}	Secondary leakage inductance	[H]
L_{mp}	Magnetizing inductance	[H]
R_s	Instantaneous fuse resistance	[Ω]
C	Secondary capacitance	[F]
I_p	Instantaneous primary current	[A]
I_s	Instantaneous secondary current	[A]
h	Instantaneous integral of current action	[A ² ·s]
h_e	Action limit	[A ² ·s]
ρ	Resistivity	[Ω·m]
ρ_0	Initial resistivity of the fuse	[Ω·m]
D_1, D_2, D_3	Material constants from curve-fit resistivity data	
R	Instantaneous fuse resistance	[Ω]
R_0	Initial fuse resistance	[Ω]
w_{sp2}	The specific energy dissipated in the fuse at which the fuse resistivity is maximum	[J/kg]

h_b	The integral of current action at full vaporization of the fuse	$[\text{A}^2 \cdot \text{s}]$
I_{p0}	Primary circuit current at the end of FCG operation	$[\text{A}]$
t_r	FCG operating time	$[\text{s}]$
ε	Exponential value to fit FCG data	
l_r	Length of a resistive element	$[\text{m}]$
A_r	Area of a resistive element	$[\text{m}^2]$
t_{eq}	Equivalent action timescale	$[\text{s}]$
t_0	Time at the end of generator operation	$[\text{s}]$
A_f	Cross-sectional area of a fuse	$[\text{m}^2]$
α_l	Fuse length proportionality constant	$\left[\frac{\text{m}^2}{\text{As}^{0.5}} \right]$
l_f	Fuse length	$[\text{m}]$
W_{fuse}	Total energy dissipated in the fuse during system operation	$[\text{J}]$
γ_m	Mass density of fuse material in solid state	$[\text{kg}/\text{m}^3]$
w_v	Specific energy for full fuse vaporization	$[\text{J}/\text{kg}]$
W_{ISE0}	Inductively-stored energy at the end of FCG operation	$[\text{J}]$
w_b	Specific energy at fuse burst	$[\text{J}/\text{kg}]$
w_{total}	Specific energy required to transition fuse from solid to vapor	$[\text{J}/\text{kg}]$
W_{source}	Total electrical energy output by an FCG	$[\text{J}]$
$W_{fuse, t < t_r}$	Energy dissipated in the fuse during FCG operation	$[\text{J}]$
$W_{load, t < t_r}$	Energy dissipated in the load during FCG operation	$[\text{J}]$
w_{spl}	Specific energy dissipated in fuse at action limit	$[\text{J}/\text{kg}]$
I_{s0}	Secondary circuit current at the end of FCG operation	$[\text{A}]$
I_{m0}	Magnetizing current at the end of FCG operation	$[\text{A}]$
R_L	Load impedance	$[\Omega]$
m_{fuse}	Total mass of the fuse wires	$[\text{kg}]$
l_{min}	Minimum fuse length	$[\text{m}]$
L_{fuse}	Inductance of the fuse	$[\text{H}]$
r_0	Radius of a fuse wire array	$[\text{m}]$
R_r	Radius of the return current conductor	$[\text{m}]$
a_w	Diameter of a single fuse wire	$[\text{m}]$
l_w	Length of the fuse wires	$[\text{m}]$
N_w	Number of fuse wires	

V_{LS}	Voltage across the stray inductance	[V]
x	Factor relating stray inductance as a multiple of the primary leakage inductance	[H]
W_C	Energy stored in the secondary capacitance	[J]
V_C	Voltage across the secondary capacitance	[V]
ω	Natural frequency of the RF oscillator	[rad/s]
$C_{tri-plate}$	Capacitance of the tri-plate geometry	[F]
ϵ_0	Permittivity of free space (8.854×10^{-12})	[F/m]
ϵ_r	Relative permittivity	
w_p	Width of a conductor in a parallel-plate geometry	[m]
l_p	Length of a conductor in a parallel-plate geometry	[m]
d_p	Distance between parallel plates	[m]
C_{ss}	Capacitance of the spiral-strip geometry	[F]
r_{ss}	Average radius of the first turn of the spiral-strip capacitor	[m]
C_{CC}	Capacitance of the coaxial-cylinder geometry	[F]
l_C	Length of the coaxial cylinders	[m]
r_{out}	Inner radius of the outer conductor in a coaxial structure	[m]
r_{in}	Outer radius of the inner conductor in a coaxial structure	[m]
$R1, R2, R3, R4$	The smallest to largest radii of the coaxial conductors	[m]
c	Concentration of a solute in water	[g/L]
$K1, K2$	Curve-fit constants for a given solute	
r_{aq}	Radius of a cylindrical aqueous-electrolyte resistor	[m]
δ	Skin depth	[m]
L_{aq}	Inductance of an aqueous-electrolyte resistor	[H]
l_{aq}	Length of an aqueous-electrolyte resistor	[m]
L_g	Inductance of a spark gap	[H]
l_g	Distance between electrodes in spark gap	[m]
r_a	Arc radius	[m]
v_0	Actual voltage to be measured	[V]
v_m	Measured voltage through a resistive voltage divider	[V]
R_1, R_2	Resistances in a resistive voltage divider	[Ω]
a	Attenuation	[dB]

Chapter 1: Introduction

1.1 The University Consortium for High Power Microwave Integration

The University Consortium for High Power Microwave Integration was a collaborative effort including the University of Missouri-Columbia (MU), Texas Tech University (TTU), and the University of New Mexico (UNM). The consortium collaborated on the integration of flux compression generators (FCGs), power conditioning components, and RF or high power microwave (HPM) sources. The program operated between October 2006 and May 2007. Independent testing was conducted at the three University campuses during this period. Integrated system tests were conducted between Texas Tech University and the University of Missouri-Columbia in Lubbock, TX April 18-22, 2007. Texas Tech University was the lead member of the consortium under the direction of Dr. Magne Kristiansen and Dr. Andreas Neuber. Texas Tech University focused its efforts on further developing and testing flux compression generators. Dr. Randy Curry was the principal investigator at the University of Missouri-Columbia. The University of Missouri-Columbia focused on a full power conditioning system from the input of the second stage of the flux compression generator to the output of a high voltage, high frequency signal that could be radiated by an antenna. The effort at the University of New Mexico was led by Dr. Edl Schamiloglu and focused on unique microwave oscillators and radiating methods.

The focus areas of the three Universities combine to form an integrated high power microwave system. The ultimate goal of the consortium was to produce electromagnetic radiation that could be measured at a distance. The program constraints included the

necessity for the full system to be as compact as possible. Therefore, the diameter of the components was limited to 15.24 cm, and each University was allotted approximately 0.5 m in length for their system.

This thesis presents the results of the MU effort focused on power conditioning components with a high power RF source. It includes the operating theory of the system components, analysis of circuit behavior, development of a non-destructive test stand, and details of component design and construction. Several novel analyses have been conducted, including the optimal transformer winding, fuse resistance modeling, a derivation of the optimum fuse length, an analysis of the effects of stray inductance, the development of the governing circuit equations, and the numerical modeling of system operation. Experimental data is provided for system testing performed on the non-destructive test stand at MU and integrated system testing with explosive components from the coordinated tests in Lubbock. Finally, a summary is presented. Before examining the FCG simulator and power conditioning components in detail, it is necessary to have a general understanding of system operation. An overview of the basic principles of flux compression generators and the power conditioning system is provided in sections 1.2 and 1.3, respectively.

1.2 Flux Compression Generator

A classification of pulsed power generators, which provides motivation for compact and portable HPM and RF systems, is the explosive magnetic generator (EMG). Explosive magnetic generators are compact pulsed power sources that use explosives as their prime power source. Due to the high energy density of explosives, EMGs can be applied as high energy pulsed power sources in much more compact and portable forms

than traditional systems consisting of capacitors, batteries, rotating machines, or inductive energy stores [1]. Five sub-classifications of EMGs include ferroelectric generators (FEGs), ferromagnetic generators (FMGs), magnetoelectric generators (MEGs), magnetohydrodynamic generators (MHDGs), and magnetocumulative generators (MCGs), which are also commonly referred to as flux compression generators (FCGs) [1]. Among these classifications of EMGs, flux compression generators are the most fully-developed technologies, and Texas Tech University has a history of experimental investigation and advancement of FCGs [2]. Therefore, the flux compression generator was chosen as the pulsed power driver for the University Consortium for High Power Microwave Integration.

The flux compression generator converts the chemical energy of explosives to an electromagnetic pulse through a field interaction process. The transfer of energy occurs as the chemical energy of the explosives is converted to kinetic energy as the high pressure detonation products accelerate the generator armature. The armature is accelerated through a magnetic field, compressing it. Through the interaction of the armature and the magnetic field, kinetic energy is converted to electromagnetic energy [2].

Although flux compression generators can take several forms, a cylindrical geometry of coaxial conductors is called a helical FCG, due to the helix that forms the outer conductor. At the beginning of FCG operation, an initial magnetic field is present between an inner conductor, the armature, and an outer conducting helix, the stator. The seed current can be established by permanent magnets or a seed current through an inductor. Explosives within the armature, along the cylindrical axis, accelerate the

armature radially outwards upon detonation. As the armature expands outwards, the stator coil is shorted, resulting in the trapping of magnetic flux. The detonation begins at one end, resulting in the crowbar action of the armature on the stator moving along the helix coil in time. This action results in electrical energy gain and current multiplication at the output of the FCG. The output waveform from the FCG is a high current with a nearly exponential rise [2]. Although the helical FCG is a high energy, compact pulsed power source, the long risetime, high current output pulse is insufficient for driving many HPM and RF loads. Therefore, conditioning of the FCG output is required to obtain a high power RF signal.

1.3 Overview of the Power Conditioning System

The University of Missouri-Columbia developed and tested an augmented version of a power conditioning system detailed by Reinovsky, Lindermuth, and Vorthman [3]. The full system is pictured in Figure 1. The system is driven by a flux compression generator or, for non-destructive testing purposes, an FCG simulator. The current source is represented schematically in Figure 1 as a variable inductance, L_{FCG} , through which a current, I_{FCG} , flows. The core elements of the power conditioning system consist of the pulse transformer, represented by L_{pri} and L_{sec} , and the exploding wire fuse opening switch, R_{fuse} . The closing switch, S_C , is a crowbar switch, which was added to limit excessive voltages from appearing across the fuse due to L_{FCG} or any stray circuit inductances. Additionally, a system capable of producing high power RF to be radiated by an antenna was added to the power conditioning system. The RF system consists of a low inductance, high voltage capacitor, C_S , a low inductance shunt, L_{shunt} , a self-breaking closing switch, S_G , and an antenna or dummy load, Z_L .

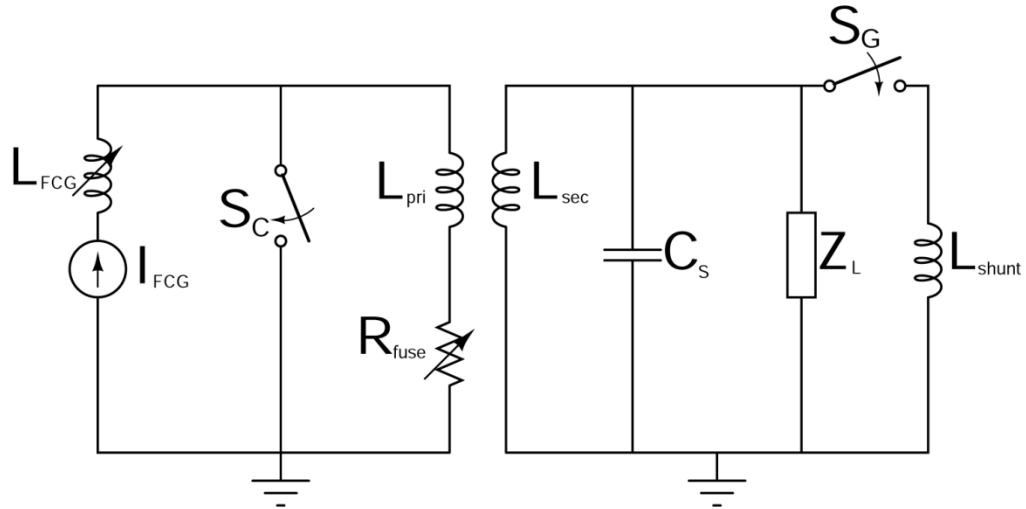


Figure 1. Full power conditioning system and RF systems

System operation can be described in three stages. The first stage corresponds to operation of the FCG or FCG simulator. As the current input to the power conditioning system increases, the energy is inductively stored in the inductance of the pulse transformer. At the same time, resistive heating of the fuse brings the fuse wires to the point of vaporization. The time of the first stage of system operation is the risetime of the current from the FCG or FCG simulator, which is usually 6 – 12 μ s. At the conclusion of the first stage of operation, the current from the source has reached its maximum, and the inductance of the FCG or FCG simulator is at a minimum. Ideally, the fuse wires reach the point of vaporization at the end of the FCG or FCG simulator operation. The second stage of operation corresponds with the vaporization of the fuse wires, resulting in a dramatic increase in fuse resistance. The rise in fuse resistance results in a fast decrease of current in the primary circuit. As the primary current decreases, the flux change in the transformer windings results in large voltages across the transformer terminals and energy transfer to the secondary circuit. The capacitor across the transformer secondary terminals, C_S , is charged to high voltage. The end of the second stage of operation occurs when the switch on the secondary, S_G , closes due to an arc breakdown of the switch

dielectric. Ideally, the closing of the secondary switch also corresponds with the primary current reaching zero amps. During the third stage of operation, the high voltage capacitor forms an underdamped oscillator with the shunt inductance, L_{shunt} . An RF signal is thus applied across the antenna or dummy load, Z_L , which can then be radiated or dissipated as desired.

Some power conditioning systems with RF sources include a peaking switch before the source components. The peaking switch prevents the development of a voltage across the secondary components until the main voltage pulse reaches a magnitude great enough to cause breakdown of the peaking switch. Since the capacitor voltage during the operation of the FCG or FCG simulator is the opposite polarity as the voltage after generator operation, the inclusion of a peaking switch warrants consideration. When a peaking switch is implemented, the capacitor voltage, v_c [V], can be described as a function of time, t [s], by equation (1) [4]. The secondary current is represented as i_s [A], and the time at which the peaking switch is closed is given by t_{peak} [s]. There is no initial voltage on the capacitor before the peaking switch is closed.

$$v_c(t) = \frac{1}{C_S} \int_{t_{peak}}^t i_s(t) dt \quad (1)$$

Implementing a peaking switch until the time of peak fuse voltage increases the lower limit of the integral. If the transformer coupling is non-ideal, the time constant for the secondary current is increased, resulting in a slowly increasing secondary current. A slow secondary current rise can result in a lower peak value to the integral of equation (1). Alternatively without a peaking switch, the capacitor voltage may be charged to several 10s of kV at the end of generator operation. The voltage is of the opposite polarity as the main pulse. However, if the RF source capacitance is on the order of hundreds of

picofarads, the charge and energy stored are only on the order of tens of microcoulombs and hundreds of millijoules, respectively. The relatively high energy transfer of the second stage of system operation can compensate for this initial charge. Additionally, there are very low losses associated with allowing current to flow in the secondary circuit without a peaking switch. The energy stored in the secondary leakage inductance and the capacitor during generator operation is minimal. Elimination of the peaking switch allows the secondary current to increase throughout the second stage of operation and results in higher peak capacitor voltages. Therefore, it is unnecessary to isolate the RF load during FCG operation, and a peaking switch is not included in the system design.

There are two fundamental differences between the system investigated in this thesis and most previous studies of high power RF sources driven by inductive energy storage systems. The first difference is in the choice of the high power RF source. Many compact power conditioning systems implement an HPM source. An example of an HPM source for compact power conditioning systems is a virtual cathode oscillator, which is commonly referred to as a vircator [5]. Figure 2 shows the schematic of the system with the RF source of Figure 1 replaced by a resistance, which approximates the impedance of the HPM source.

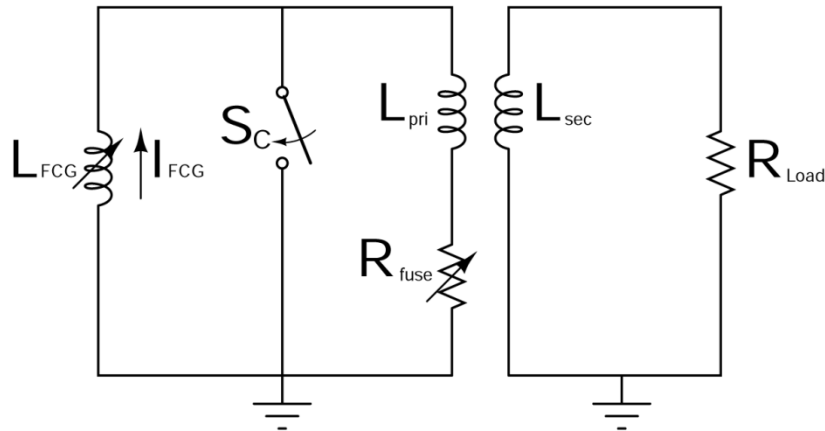


Figure 2. Power conditioning system with resistive load

The system shown in Figure 2 is also driven by an FCG or FCG simulator, L_{FCG} . The fundamental power conditioning components again form the basis of the system, including the pulse transformer, L_{pri} and L_{sec} , exploding wire fuse, R_{fuse} , and crowbar switch, S_C . The impedance of the load, R_{Load} , represents the HPM source. Some versions of the circuit of Figure 2 include a peaking switch between the transformer and load to prevent a voltage pre-pulse from degrading the HPM source operation. The power conditioning system in Figure 2 operates similarly to the previously described system, but the power conditioning system operates in only two stages. The first stage of operation again corresponds to operation of the FCG or FCG simulator. A voltage across the secondary of the transformer results in some energy dissipation in the load if it is not isolated by a peaking switch. In stage two, the sudden increase of fuse resistance in the primary circuit results in a rapid decrease in primary current and a large voltage across the transformer terminals. The voltage across the load is of opposite polarity and several times greater in magnitude as compared to the first stage, and energy is transferred to the load in a large pulse. The high voltage pulse drives high power microwave production in the load, thus eliminating the need for a third stage of operation.

This investigation focuses on the implementation of the RF source of Figure 1. However, similarities between the system investigated in this thesis and a system with an HPM load allow much of this work to also apply for HPM systems. Additionally, the circuit of Figure 2 is utilized in Chapter 4 to perform numerical analyses of the dynamic fuse resistance in a full system.

The second fundamental difference between the system of Figure 1 and most previous studies of inductive energy storage systems driving RF sources is the utilization of a

transformer as the inductive energy storage element. Previous studies have implemented an inductor rather than a transformer as the inductive energy storage element [2, 6, 7]. It should be noted that the operation of those systems is very similar as the energy from the current source is inductively-stored and transferred to the load through the use of an opening switch. Therefore, much of the work from this investigation can be applied to systems with an inductor rather than a transformer. The systems are equivalent when the transformer turn ratio and coupling factor are equal to one [3].

References for Chapter 1

- [1] L. L. Altgilbers, I. Grishnaev, I. R. Smith, Y. Tkach, M. D. J. Brown, B. M. Novac, and I. Tkach, *Magnetocumulative Generators*. New York, NY: Springer-Verlag, 2000.
- [2] A. A. Neuber, "Explosively Driven Pulsed Power," Berlin: Springer-Verlag, 2005.
- [3] R. E. Reinovsky, I. R. Lindemuth, and J. E. Vorthman, "High voltage power condition systems powered by flux compression generators," in *Proc. 7th Pulsed Power Conference*, R. White and B. Bernstein, Eds. Monterey, CA, 1989.
- [4] C. K. Alexander and M. N. O. Sadiku, *Fundamentals of Electric Circuits*: McGraw-Hill Higher Education, 2000.
- [5] J. Benford, J. A. Swegle, and E. Schamiloglu, *High Power Microwaves*, 2 ed. Boca Raton, FL: CRC Press, 2007.
- [6] M. Giesselmann, T. Heeren, E. Kristiansen, J. G. Kim, J. C. Dickens, and M. Kristiansen, "Experimental and analytical investigation of a pulsed power conditioning system for magnetic flux compression generators," *IEEE Trans. on Plasma Science*, vol. 28, pp. 1368-1376, 2000.
- [7] A. Larsson, P. Appelgren, G. Bjarnholt, T. Hultman, and S. E. Nyholm, "Energy flow in a pulsed-power conditioning system for high-power microwave applications," in *Proc. 14th IEEE International Pulsed Power Conference* Dallas, TX, 2003.

Chapter 2: FCG Simulator

2.1 Background

An on-campus test stand at the University of Missouri-Columbia was necessary for the power conditioning components to be cost-effectively and non-destructively tested. The test stand was designed to approximate the nearly exponential current rise of an FCG. To approximate the expected waveform from the FCG, peak currents from 20 kA to 40 kA were desired with risetimes in the range of 7 μ s to 14 μ s. Unlike a simple capacitive discharge in which the peak current occurs when the rate of current change is zero, it is desirable for the current to reach the desired value while the rate of current rise is still high. Two methods of simulating this waveform were demonstrated by Belt, and a system based upon magnetically switched parallel inductors was built at MU [1]. The FCG simulator utilizes a decreasing inductance in time to increase the rate of capacitive discharge in time. Figure 3 displays the basic schematic of the FCG simulator. There are two significant differences between the FCG simulator investigated by Belt and the simulator built at MU, which will be further explained in the component sections. First, the simulator used by Belt was designed primarily to test fuses without an external inductive storage element [1]. The inductive store of the system was designed to be the final inductance of the FCG simulator. However, the system at MU was required to drive the full power conditioning system, including the pulse transformer. Therefore, the final inductance of the FCG simulator was designed to be minimal at the end of operation. Second, the system investigated by Belt used a type E pulse forming network (PFN) as the primary energy storage component [1]. However, as will be detailed later, the

impedance mismatch between a PFN and the power conditioning circuit negated the benefits of using a PFN. A capacitor bank was chosen as the primary energy store for the simulator at MU.

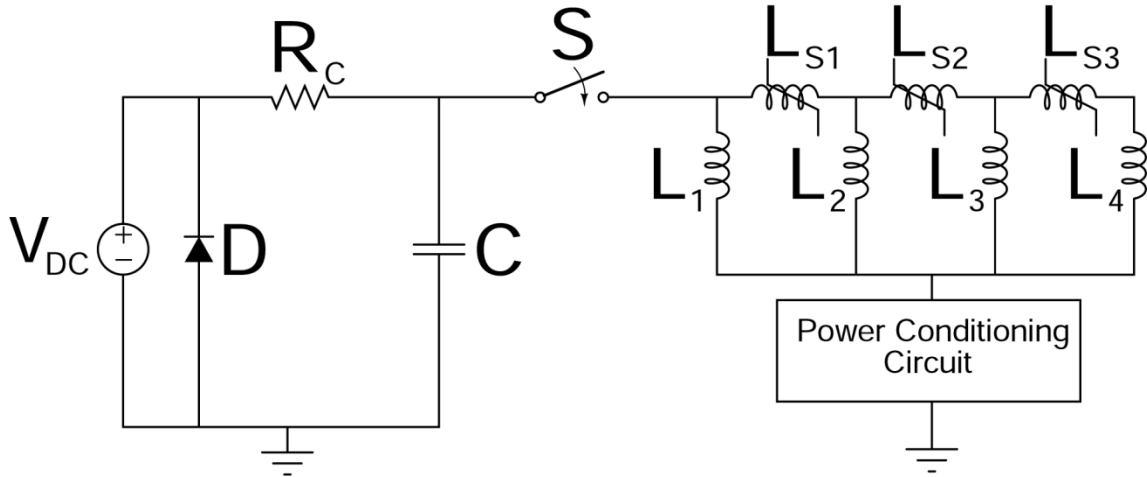


Figure 3. Schematic of the FCG simulator driving the power conditioning circuit

A DC charged high voltage capacitor bank serves as the primary energy storage. Upon closure of the spark gap switch, S , the capacitor bank is discharged through a network of parallel inductors in which $L_1 > L_2 > L_3 > L_4$. Components L_{S1} , L_{S2} , and L_{S3} are magnetic switches that sequentially saturate to switch the parallel inductors into the circuit. As each magnetic switch closes, the inductance in series with the capacitor bank is decreased, and the rate of current rise increases. The increasing current signal drives the primary circuit of the power conditioning system similarly to an FCG.

Operation of the FCG simulator can be considered in four stages, corresponding to the four impedances of the inductor network between the closure of each magnetic switch. The circuit operation in each stage can be approximated by a capacitive discharge with constant parameters. Chapter 4 will describe how the fuse resistance increases during the operation of the FCG or FCG simulator. However, since the change of the fuse resistance during generator operation is relatively small and the impedance of the inductance is

dominant, the change in the fuse resistance during each stage of FCG simulator operation can be neglected except in detailed simulations. The primary circuit current during each stage of operation, $i_{p,m}$ [A], can be described as a function of time, t [s], as an underdamped capacitive discharge, described by equation (2) [2]. The subscript m is an integer between 1 and 4, corresponding to the stage of FCG simulator operation.

$$i_{p,m}(t) = (I_{1,m} \cos(\omega_m(t - t_m)) + I_{2,m} \sin(\omega_m(t - t_m)))e^{-\alpha_m(t-t_m)} \quad (2)$$

The circuit energy at the beginning of each stage of operation, W_m [J], can be calculated with equation (3). The capacitance of the primary energy store is represented by C [F], and the effective primary circuit inductance for each stage is represented by $L_{eff,m}$ [H]. The capacitor voltage and primary circuit current at the beginning of each stage of operation are symbolized as V_m [V] and I_m [A], respectively [2].

$$W_m = \frac{1}{2}(CV_m^2 + L_{eff,m}I_m^2) \quad (3)$$

At the beginning of simulator operation, V_m is the initial charging voltage of the capacitor bank, and I_m is zero. The capacitance, C , is the same for each stage of operation. The value of $L_{eff,m}$ is determined by the network of inductors, as given by equations (4)-(7). As described later in this chapter, the inductance of the magnetic switches can be described with a very high value while unsaturated and a much lower value while saturated. Although the unsaturated inductance value is finite, it is considered high enough to be omitted in calculations while in parallel with a much lower inductance air-core or saturated inductor. The saturated inductance of the magnetic switch should be considered in determining $L_{eff,m}$, so the saturated values for magnetic switches L_{S1} , L_{S2} , and L_{S3} are included as $L_{S1,sat}$, $L_{S2,sat}$, and $L_{S3,sat}$, respectively.

$$L_{eff,1} = L_p + L_1 \quad (4)$$

$$L_{eff,2} = L_p + \frac{L_1(L_{S1,sat} + L_2)}{L_1 + L_{S1,sat} + L_2} \quad (5)$$

$$L_{eff,3} = L_p + \frac{L_1 \left(L_{S1,sat} + \frac{L_2(L_{S2,sat} + L_3)}{L_2 + L_{S2,sat} + L_3} \right)}{L_1 + L_{S1,sat} + \frac{L_2(L_{S2,sat} + L_3)}{L_2 + L_{S2,sat} + L_3}} \quad (6)$$

$$L_{eff,4} = L_p + \frac{L_1 \left(L_{S1,sat} + \frac{L_2 \left(L_{S2,sat} + \frac{L_3(L_{S3,sat} + L_4)}{L_3 + L_{S3,sat} + L_4} \right)}{L_2 + L_{S2,sat} + \frac{L_3(L_{S3,sat} + L_4)}{L_3 + L_{S3,sat} + L_4}} \right)}{L_1 + L_{S1,sat} + \frac{L_2 \left(L_{S2,sat} + \frac{L_3(L_{S3,sat} + L_4)}{L_3 + L_{S3,sat} + L_4} \right)}{L_2 + L_{S2,sat} + \frac{L_3(L_{S3,sat} + L_4)}{L_3 + L_{S3,sat} + L_4}}} \quad (7)$$

The damping factor in each stage of operation, α_m [s⁻¹], can be calculated by equation (8) [2]. The series circuit resistance in each stage of FCG simulator operation, including the fuse and stray circuit resistances, is represented as R_m [Ω].

$$\alpha_m = \frac{R_m}{2L_{eff,m}} \quad (8)$$

The symbol ω_m is the natural angular frequency described by equation (9) [2].

$$\omega_m = \sqrt{\frac{1}{L_{eff,m}C} - \alpha_m^2} \quad (9)$$

The constant $I_{1,m}$ [A] can be determined from initial conditions to simply be I_m [A]. The constant $I_{2,m}$ can then be calculated from equation (10).

$$I_{2,m} = \frac{1}{\omega_m L_{eff,m}} \left[V_m + \frac{R_m I_m}{2} \right] \quad (10)$$

Since the primary current is continuous, the initial current of a stage is equal to the final current of the previous stage. The transition times, t_m [s], from one stage of operation to

the next occur at $t_{sat,1}$, $(t_{sat,1} + t_{sat,2})$, and $(t_{sat,1} + t_{sat,2} + t_{sat,3})$, where $t_{sat,1}$ [s], $t_{sat,2}$ [s], and $t_{sat,3}$ [s] are the saturation times of magnetic switches L_{S1} , L_{S2} , and L_{S3} , respectively. The saturation times of the magnetic switches can be predicted, as described later in this chapter. The beginning of stage 1 can be considered $t = 0$, so $t_l = 0$. The current at which the simulator transitions between stages of operation can be calculated with equation (11).

$$I_m = \left(I_{1,m-1} \cos(\omega_{m-1}(t_{sat,m-1})) + I_{2,m-1} \sin(\omega_{m-1}(t_{sat,m-1})) \right) e^{-\alpha_{m-1}(t_{sat,m-1})} \quad (11)$$

Equations (2)-(11) can be used to describe the operation of the FCG simulator up to the point at which the fuse resistance increases rapidly and can no longer be approximated as constant. The point at which the fuse resistance rapidly rises coincides with the end of FCG or FCG simulator operation, so the equations presented here completely describe the operation during the period of interest. Figure 4 shows an example of the FCG simulator current as the product of four stages of operation described by equation (2). Stages 1-4 correspond to the RLC discharge with successively lower circuit inductance. The waveform for each stage is shown, and the FCG simulator current is shown as the black waveform.

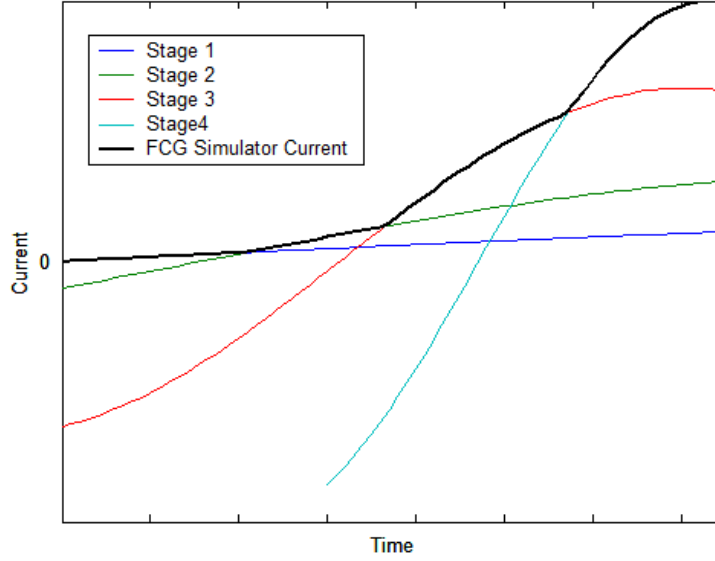


Figure 4. Example of FCG simulator current in four stages

Since the rate of current rise is of particular interest in the design of the simulator components, it is useful to understand the effects of component values on the rate of current rise. The maximum rate of current rise for each stage occurs at the beginning of the stage operation. The maximum rate of current rise for each stage is given by equation (12) [2].

$$\frac{di_{p,m \max}}{dt} = \frac{1}{L_{eff,m}} (V_m - R_m I_m) \quad (12)$$

The preceding equations aid in the design of the capacitor bank, charging voltage, inductors, and magnetic switches. The following section describes the design of each critical component.

2.2 FCG Simulator Component Designs

2.2.1 Primary Energy Storage

Design of the capacitance and charging voltage of the primary energy storage is critical in adjusting the amount of energy available to the power conditioning system and the risetime of the current signal. The primary energy storage implemented by Belt was a

type E pulse forming network [1]. A type E PFN can supply a matched load with an approximately square voltage pulse [3]. A constant applied voltage across the network of inductors in Figure 3 could be beneficial in the design of the magnetic switches and other components. However, the PFN implemented by Belt was intentionally mismatched to the low impedance load, so the output current of the PFN without the inductor network approximately had a 4 μs risetime without a constant pulse peak [1]. Given the mismatch of the PFN with the inductor network and power conditioning circuit, the benefits of implementing a PFN as the primary energy store were seen as minimal, and a simple capacitive store was selected for the MU FCG simulator.

Through circuit simulations, which will be described later in this chapter, the primary energy storage was designed for a capacitance of approximately 11 μF and a charging voltage between 15 kV and 30 kV, depending upon the desired peak current. Five 2.2 μF Aerovox capacitors rated at 100 kV were utilized as the primary energy storage. The capacitor bank was charged by a 50 kV, 6 mA peak Glassman High Voltage power supply, V_{DC} , through a 100 k Ω resistor, R_C . A diode stack, D , was placed in parallel with the power supply to protect it from transient conditions that could damage it. For safety, the capacitor bank was shorted through a relay and 100 k Ω resistor when not in use. The relay, rated at 45 kV, was opened during system operation. Figure 5 shows the stored energy of the capacitor bank up to the peak rated voltage of the relay.

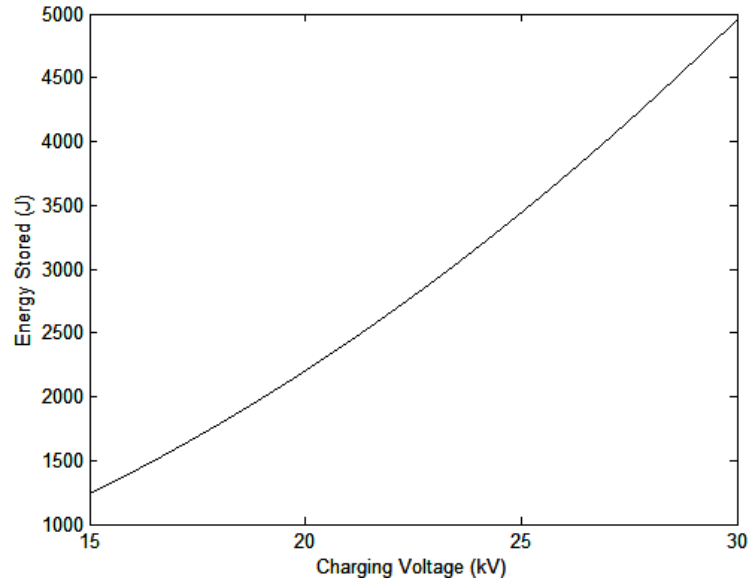


Figure 5. The range of primary energy storage in the FCG capacitor bank

The capacitor bank is discharged through a spark gap switch, S . Precise time triggering of the switch was not required, so the spark gap was triggered by adjusting the gas pressure in the switch. The spark gap was a model T-670 from L-3 Pulse Sciences with modified stainless steel electrodes [4]. The gap spacing was less than 0.5 cm to allow breakdown in the switch in atmospheric pressure air at voltages greater than 15 kV. The spark gap was pressurized to 70 psig with SF₆ to prevent closure of the switch during charging of the primary energy store. When the capacitor bank had been fully charged, the gas lines were opened to allow the gas pressure to decrease, resulting in electrical breakdown and closure of the switch.

2.2.2 Magnetic Switches

Since Melville first detailed the use of saturating magnetic materials in 1951, magnetic switches have been a unique option for transient switching [5]. Magnetic switches have been widely used in magnetic pulse compression circuits for laser drivers and

accelerators [6-8]. The magnetic switches of the FCG simulator enable the sequential switching of the fixed parallel inductors, $L_1 - L_4$, to provide a decreasing circuit inductance during the simulator operation. A simple magnetic switch can be formed by winding a conductor around a magnetic core. Current through the conductor creates a magnetic field, which is coupled in the magnetic core material. As the magnetic domains in the core align, the magnetic field, H [A/m], and the magnetic flux density, B [T], in the core material are changed [9]. The magnetic field and the magnetic flux density are related by the permeability of the magnetic material, μ [H/m]. The permeability is the product of the permeability of free space, μ_0 [H/m], and the relative permeability of the material, μ_r . Equation (13) shows the relation between the magnetic flux density, magnetic field, and permeability [10].

$$B = \mu_0 \mu_r H \quad (13)$$

A plot of the magnetic flux density versus the magnetic field is known as a hysteresis loop [9]. An example of a hysteresis loop is shown in Figure 6.

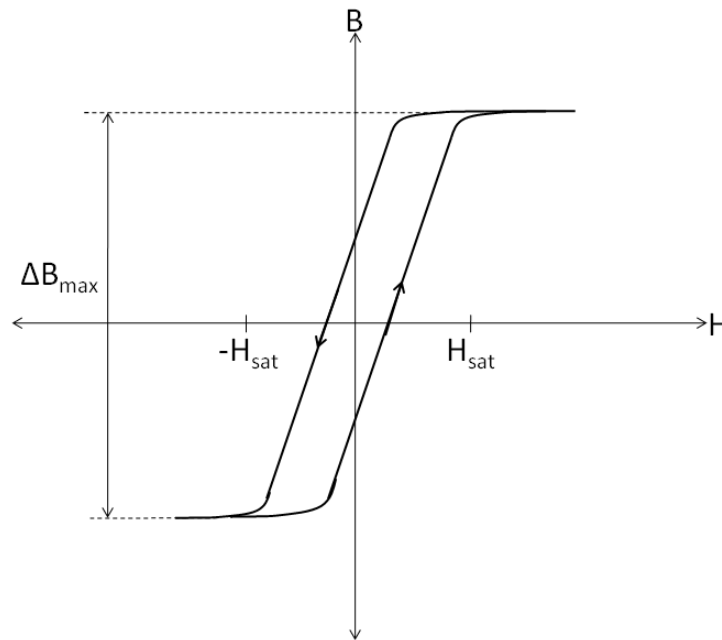


Figure 6. Example hysteresis loop of a magnetic material

When examining Figure 6 with consideration of equation (13), it is evident that the permeability of a magnetic material can vary. Since the permeability of free space is a constant, the relative permeability is the factor that varies with the magnetic field in the material. When the absolute value of the magnetic field in the magnetic material is less than the saturation value, H_{sat} [A/m], the magnetic field and magnetic flux density have approximately a linear relation. Additionally, a small change in the magnetic field results in a large change in the magnetic flux density in this region. This relation corresponds to a constant relative permeability with a high value. This region corresponds to the unsaturated state of the magnetic core. As the magnetic field increases, more magnetic domains align in the magnetic field. When the absolute value of the magnetic field is greater than H_{sat} , relatively large changes in the magnetic field result in small changes in the magnetic flux density. This region corresponds to the saturated state of the magnetic core. The magnetic domains are aligned in the magnetic field and further increases in the magnetic field do not change the state of the magnetic material. Magnetic switches utilize the differences between the unsaturated and saturated states to change the impedance of a winding coupled to the core material.

The current-carrying winding around the magnetic core has an inductive impedance directly proportional to the relative permeability of the magnetic material. The equation for solenoid inductance, L [H], is given as equation (14) [11]. The symbol N represents the number of turns. The symbol A [m²] is the cross-sectional area of the magnetic core, and the length of the solenoid is given as l [m].

$$L = \frac{\mu_0 \mu_r N^2 A}{l} \quad (14)$$

When the core is unsaturated, the relative permeability is relatively high, and the inductance of the solenoid is proportionally increased. The high impedance of the winding results in a very slow rate of current rise. If a lower impedance parallel current path is present, the current path through the winding can approximately be considered to be open. When the core is saturated, the relative permeability is approximately one, and the inductance of the winding is much lower than its unsaturated value. Impedance to current in the winding is much lower, and the current path through the winding can no longer be considered open. This is the closed state of the magnetic switch. In this way, the magnetic switch operates by transitioning from a high inductive impedance while the core is unsaturated to a low inductive impedance after saturation of the core [12].

Modeling a magnetic material can include eddy currents, magnetic losses, and other effects [13]. For the purposes of modeling a magnetic switch in a single-shot system, these effects have minor influence on the behavior of the FCG simulator output and can be considered negligible. The primary parameters that must be modeled are the unsaturated and saturated inductance values. The magnetic switch can be replaced by the inductors and switch in Figure 7 [5]. The impedance of the magnetic switch is initially a relatively high inductance, L_{unsat} [H]. After the core has saturated, the inductance of the switch decreases to a relatively low value, L_{sat} [H]. If the switch of Figure 7 closes when the magnetic switch saturates and L_{unsat} is much greater than L_{sat} , the parallel impedance of the two inductors will be approximately equal to L_{sat} .

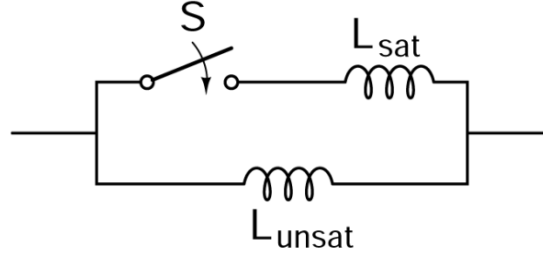


Figure 7. Simple model of a magnetic switch

The design of the magnetic switches in the FCG simulator is primarily dependent upon the change in flux density in the magnetic core. The change in flux density, ΔB [Wb/m²], due to a single winding turn is equivalent to the integral of the applied voltage per unit area. Expressing this relationship mathematically, the required area of the core can be determined based upon the maximum change in flux density, the number of turns, and the integral of the applied voltage [7].

$$A = \frac{1}{\Delta BN} \int_0^{t_{sat}} V(t) dt \quad (15)$$

The voltage across the inductance is V [V], and the symbol t_{sat} [s] is the time of core saturation. The number of turns on the core is N , and the area of the core is represented as A [m²]. Due to the high voltage applied at the beginning of FCG simulator operation, the cores required a large area and high change in magnetic flux density to remain unsaturated for a time on the order of microseconds. The number of turns could also be increased. However, the N^2 term of equation (14) shows how the inductance of the winding increases with more turns. Therefore, to minimize the saturated inductance of the winding, the number of turns was limited. Each of the three magnetic switches was formed from stacks of identical magnetic cores to increase the cross-sectional area. Magnetic switches L_{S1} and L_{S2} were both formed with two Metglas AMCC1000 cores

[14]. Magnetic switch L_{S3} was formed with three square orthonol cores. The parameters of the three magnetic cores are given in Table 1.

Table 1. Magnetic Core Parameters

Magnetic Switch	N	A (cm ²)	ΔB (T)	Volt-Second Product (V·s)
L_{S1}	4	42	2.5	0.042
L_{S2}	4	42	2.5	0.042
L_{S3}	4	19.9	2.5	0.0199

After operation of the FCG simulator, the cores of the magnetic switches will relax to a state such that the maximum ΔB to saturation with the next applied voltage is substantially reduced. Therefore, the cores must be reset, or saturated with the opposite bias, to enable a large change in flux density [15]. The minimum reset current, I_{reset} [A], can be produced in the magnetic switch winding in the opposite direction as the FCG simulator current, or a separate winding can be implemented. The reset current is determined by the number of reset windings, N_r , the magnetic path length of the core, l_m [m], and the saturation magnetic field, H_{sat} [A/m], as shown in equation (16) [15].

$$I_{reset} \geq \frac{l_m H_{sat}}{N_r} \quad (16)$$

The parameters l_m and H_{sat} are dependent upon the magnetic core. Since the FCG simulator is not repetitively operated, the number of windings and reset current supply were not critical design factors. A 9 A DC current supply was implemented as the reset current source. Table 2 summarizes the parameters for current reset. The value of the saturation magnetic field is overestimated for L_{S1} and L_{S2} to ensure enough turns were in place to reset the core.

Table 2. Core Reset Parameters

Magnetic Switch	l_m (m)	H_{sat} (A/m)	I_{reset} (A)	N_r
L_{S1}	0.427	100	9	6
L_{S2}	0.427	100	9	6
L_{S3}	0.288	10	9	2

Figure 8 and Figure 9 show the magnetic switches formed by the Metglas and square orthonol cores, respectively.



Figure 8. Magnetic switch. White: switch winding. Red: reset winding



Figure 9. Magnetic switch. White: switch windings. Red: reset windings

2.2.3 Air-Core Inductors

The design of inductors $L_1 - L_3$ of the FCG simulator, as seen in Figure 3, is critical for optimizing the risetime of the current signal. As in a typical capacitive discharge and seen in equation (12), higher circuit inductance will slow the rate of current rise. As each

of the air-core inductors is switched into the circuit, the circuit inductance, $L_{eff,m}$, is reduced, and the rate of current rise increases. Circuit simulations, which will be presented later in this chapter, were utilized to tune the inductor values to allow for an 8 μ s current risetime. These values would ensure that the FCG simulator could operate within the range of desired peak currents and current risetimes simply by adjusting the charging voltage of the primary energy store. The inductors were implemented as air-core solenoids, so the inductance of each could be designed by applying equation (14) with a relative permeability equal to one. Table 3 lists the parameters for each inductor.

Table 3. Air Core Solenoid Parameters

Inductor	Inductance (μH)	Solenoid Area (cm^2)	N	Length (cm)
L_1	25	218.0	15	17.44
L_2	10	62.2	18	20.93
L_3	0.5	62.2	3	3.49

Unlike the system investigated by Belt, the FCG simulator was implemented to drive a full power conditioning system with an external inductive store. Therefore, the final effective inductance of the inductor network needed to be as low as possible. The inductance of the final inductor to be switched into the circuit during FCG simulator operation, L_4 , was designed to minimize the final effective inductance of the network. The implementation of L_4 was simply a short with no turns for a minimal inductance.

The fixed inductors of the FCG simulator were constructed with 0.635 cm diameter copper tubing wound on cylindrical forms. Turns of the copper tubing were separated by a corresponding winding of insulating O-ring material. Figure 10 shows inductor L_1 as an example of a constructed air core solenoid.



Figure 10. Air core solenoid

2.3 FCG Simulator Component Integration

The FCG simulator was built with safety of the operator in mind. The capacitor bank is housed within a steel enclosure topped by garolite sheets that support many of the other FCG simulator components. Two wooden shields 2.44 m tall and 1.22 m wide stand between the FCG simulator and the operator for protection. From behind the protective barriers the operator can cut off electrical power to the system, control the power supply, activate and deactivate the safety charging relay, reset the magnetic cores, and release the pressurized gas from the main spark gap switch. A safety relay rated for 45 kV is open while charging and can be closed to discharge the capacitor bank through a resistor at any time. Figure 11 shows the initial construction of the FCG simulator without protective shielding for testing with inductive loads. Figure 12 shows the FCG simulator prepared for testing with the power conditioning circuit and RF load.

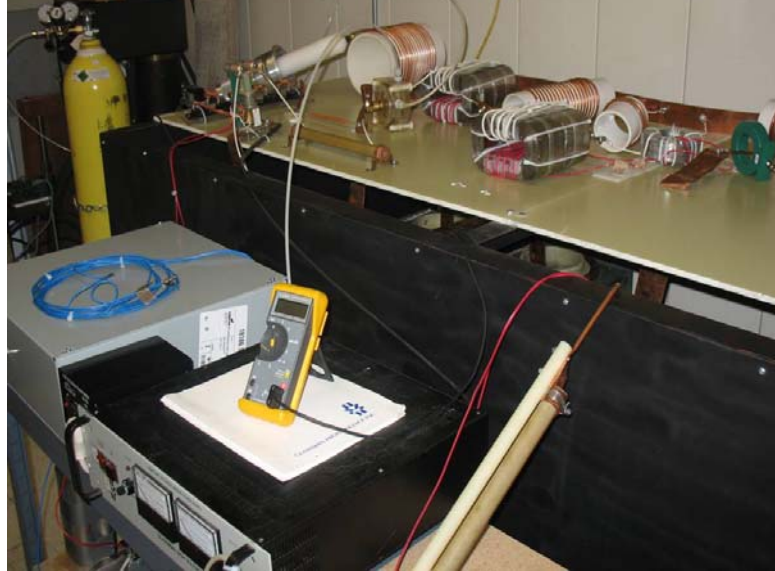


Figure 11. FCG simulator

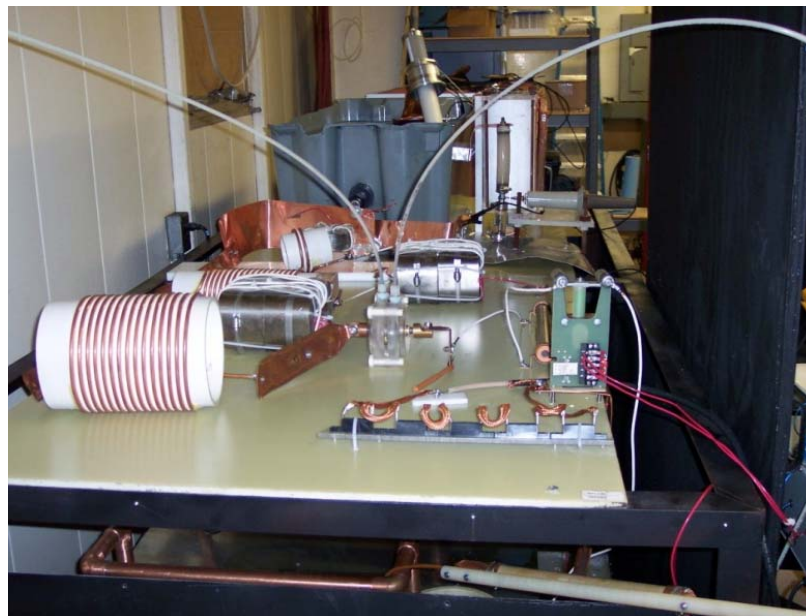


Figure 12. FCG simulator components in foreground

2.4 FCG Simulator Results

2.4.1 PSpice Simulations of the FCG Simulator

Figure 13 shows the schematic developed for design and simulation of the FCG simulator with OrCAD PSpice [16]. Near the bottom of the figure, the capacitor bank is represented as $C2-C6$. The charging circuit, $V6$ and $R13$, and safety circuit, $S6$ and $R13$,

are represented for the schematic but have negligible effects on the transient circuit simulation. The switch $S5$ represents the main spark gap switch through which the FCG simulator is triggered. Each of the magnetic switches is represented as a large inductance in parallel with a small inductance and switch, as in Figure 7. Magnetic switch L_{S1} is represented in the schematic by inductors $L2$ and $L9$ with switch $S1$. Similarly, magnetic switch L_{S2} is represented by inductors $L4$ and $L10$ with switch $S2$, and magnetic switch L_{S3} is shown as $L6$, $L11$, and $S3$. Each of the switches in the model is controlled by a timed voltage source, which manipulates the switch resistance from a high value, R_{off} , to a low value, R_{on} , during a programmable switching time, TR . The timing of the voltage-controlled switches for each magnetic switch is adjusted to match the predicted maximum volt-second product across each switch from Table 1. The inductors $L1$, $L3$, $L5$, and $L7$ represent the air-core inductors L_1 , L_2 , L_3 , and L_4 from Figure 3. A few inductances and resistances are included to include the effects of stray impedances and prevent inductive loops in the magnetic switch models. Lastly, the simulations and initial tests of the FCG simulator were designed to evaluate the current produced into the inductive energy storage element. The inductive-storage element is represented by the 1 μH inductor $L19$.

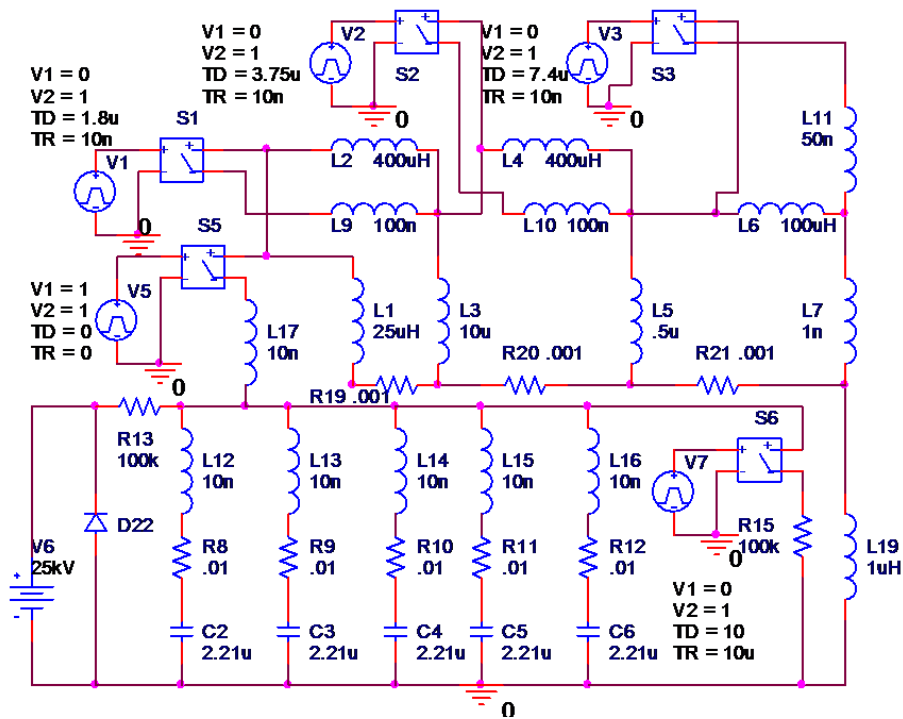


Figure 13. PSpice schematic for design simulations of the FCG simulator

Table 4 summarizes the inductive elements of the FCG simulator. Using 11 μF as the total capacitance of the primary energy store and assuming a total series resistance of 10 $\text{m}\Omega$, the values for $L_{\text{eff},m}$, α_m , and ω_m are calculated based upon the previously-derived equations. As the magnetic switches saturate, the effective inductance approaches the inductance of the inductive energy storage element, 1 μH .

Table 4. Summary of Inductor Values for Simulation of the FCG Simulator

$L19$ [H]	$L2$ [H]	$L9$ [H]	$L4$ [H]	$L10$ [H]	$L5$ [H]	$L11$ [H]
1.00E-06	4.00E-04	1.00E-07	4.00E-04	1.00E-07	1.00E-04	5.00E-08
$L1$ [H]	$L3$ [H]	$L5$ [H]	$L7$ [H]			
2.50E-05	1.00E-05	5.00E-07	1.00E-09			
m	$L_{\text{eff},m}$ [H]	ω_m [rad/s]	α_m [Ω/H]			
1	2.60E-05	5.91E+04	1.92E+02			
2	2.37E-05	6.19E+04	2.11E+02			
3	1.65E-06	2.35E+05	3.03E+03			
4	1.24E-06	2.70E+05	4.02E+03			

The initial conditions of the capacitors are set to the peak charging voltage. For the simulation presented in this section, the charging voltage is 25 kV. All of the inductors have no initial current. The switch $S5$ can be programmed to initiate the capacitive discharge at any time, but no delay is included in this simulation. Figure 14 shows the simulated current rise in the inductive store, $L19$. The effects of the saturating magnetic cores can be seen on the change in the rate of current rise at approximately 1.8 μs , 3.75 μs , and 7.4 μs . At 8 μs into the simulator operation, the current in the inductive store is 56.4 kA. The peak current reaches approximately 63.75 kA.

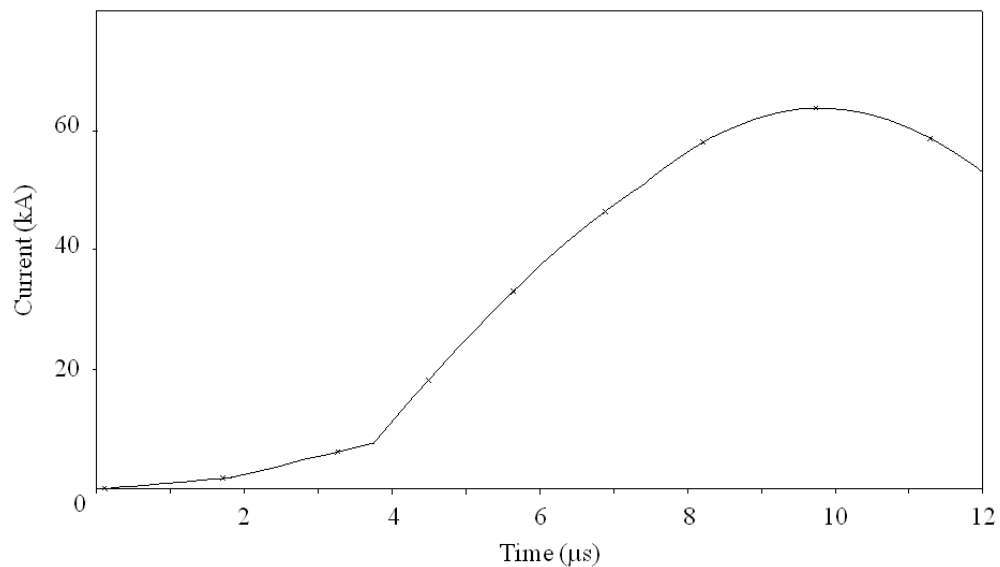


Figure 14. PSpice output current waveform of FCG simulator driving 1 μH load

One of the crucial aspects of the simulation of the FCG simulator is the modeling of the magnetic switches. The switching behavior of the magnetic switch models is demonstrated by examination of the voltages across the magnetic switches. Figure 15 shows the voltages across each of the magnetic switches. The voltage drop across each switch corresponds to the decrease in the inductance of the magnetic switch upon saturation.

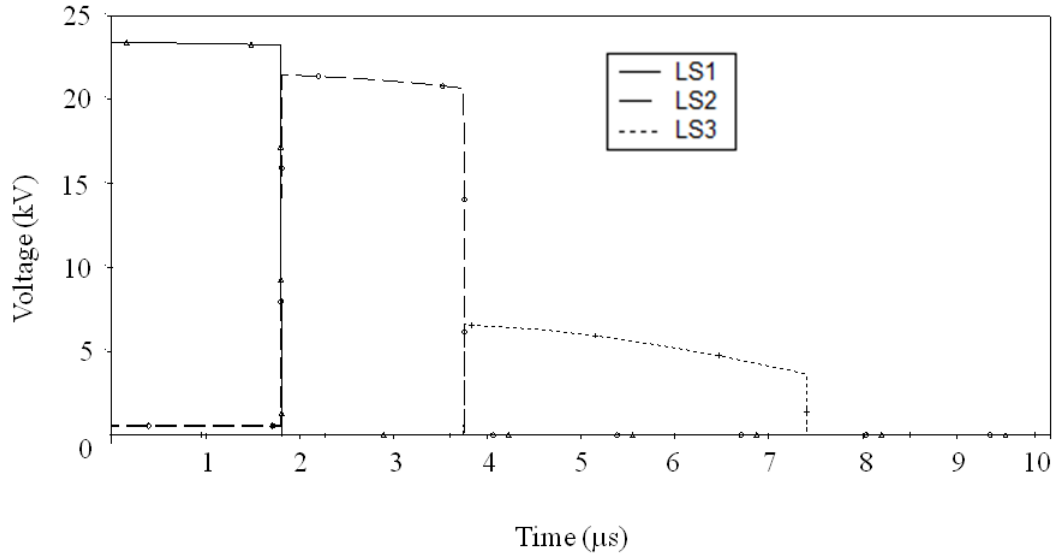


Figure 15. Magnetic switch voltages during FCG simulator operation

Finally, the accuracy of the magnetic switch models and the voltage curves of Figure 15 are confirmed by comparison of the simulated flux change in each magnetic switch core with the calculated values of Table 1. The flux change in each core can be calculated as the integral of the voltage across the switch, which results in the volt-second product. Figure 16 verifies the flux change of 0.042 V·s, 0.042 V·s, and 0.02 V·s for switches L_{S1} , L_{S2} , and L_{S3} , respectively.

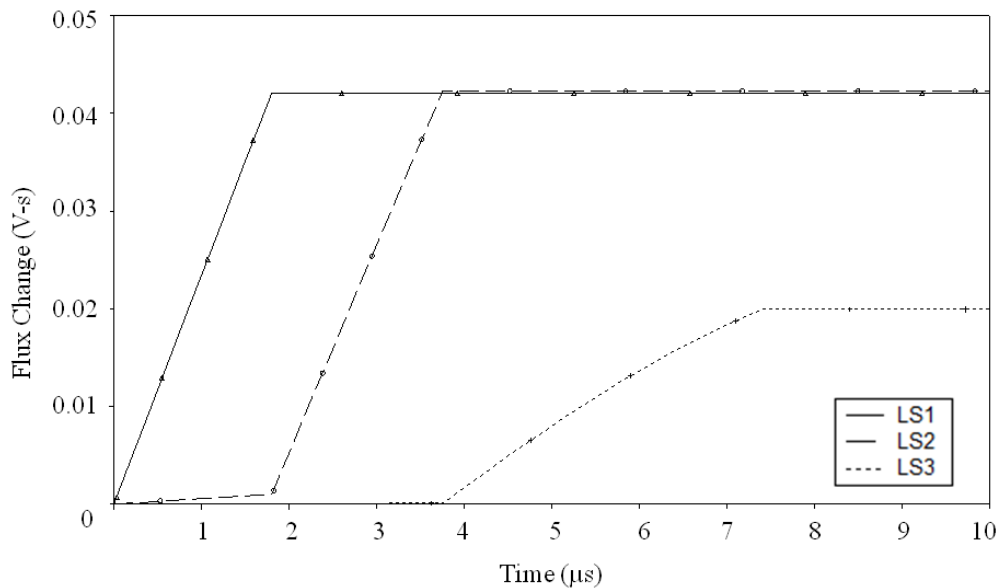


Figure 16. Flux change in magnetic switches

2.4.2 FCG Simulator Experimental Results

The FCG simulator was extensively tested into inductive loads of approximately 1 μH prior to implementing the pulse transformer, exploding wire fuse, and HV RF source. The system was tested for safety, reliability, and characterization purposes. The typical charging voltages of the primary energy store were 20 kV – 25 kV. A North Star High Voltage PVM 6 high voltage probe rated at 100 kV monitored the voltage at the inductor network, and a Pearson 101 current transformer monitored the current through the inductive load [17, 18]. Additional details on the diagnostics are provided in Chapter 6.

Figure 17 shows the FCG simulator output with a 20 kV initial charging voltage. The effect of the decreasing circuit inductance on the rate of current rise can be clearly seen in the concave up shape of the current waveform. A line is included after an 8 μs risetime to designate an example point at which the fuse resistance would open the circuit. The current after an 8 μs risetime is greater than 40 kA. The voltage on the capacitor bank after the 8 μs risetime is approximately 15 kV. With the remaining charge on the capacitor bank at the normal time the fuse would open the circuit, a significant amount of energy is expected to still be stored in the capacitor bank.

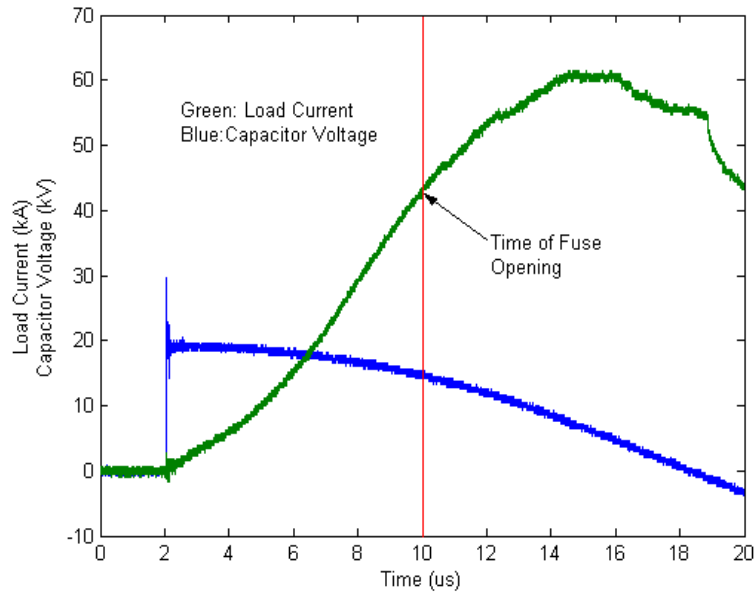


Figure 17. FCG simulator operation into inductive load with 20 kV initial voltage

Figure 18 shows the FCG simulator output produced with a 25 kV initial charge voltage. Again, the effect of the decreasing circuit inductance can be seen in the concave upward shape of the current rise. After an 8 μ s risetime, the current has reached a peak between 55 kA and 60 kA. At this point, the current in a system with a fuse would be interrupted by the rapid increase in fuse resistance. The capacitor bank voltage after the 8 μ s risetime is greater than 15 kV, meaning more than 1.2 kJ is still stored in the capacitor bank at the desired end of FCG simulator operation. The dissipation of this remaining energy and its effects on the system performance are one reason to implement the crowbar switch, as will be described in Chapter 4. It is noted that the addition of the fuse typically reduces the peak current to between 30 kA and 40 kA. Additional results of the FCG simulator performance with a full power conditioning system are included in the results of Chapter 6.

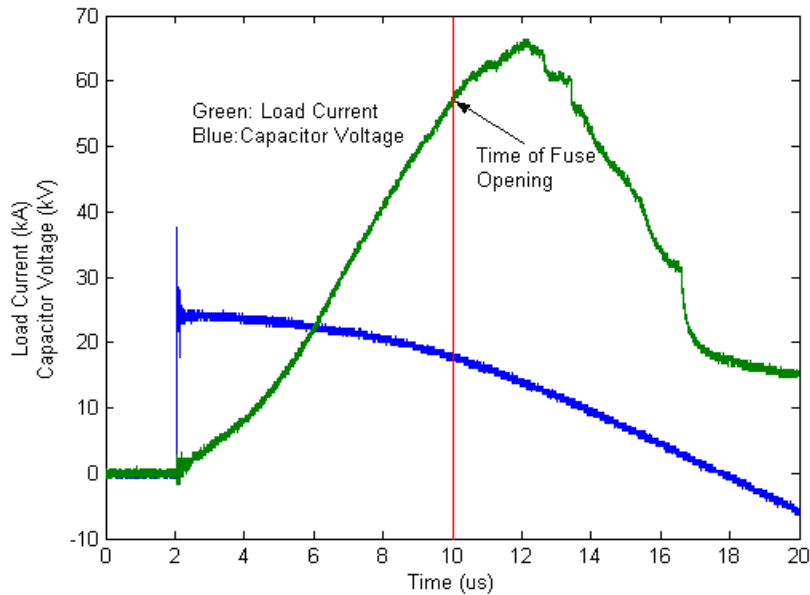


Figure 18. FCG simulator operation into inductive load with 25 kV initial voltage

References for Chapter 2

- [1] D. Belt, "Non-explosive test bed for flux compression generator fuses," M.S. Thesis, Elec. and Comp. Engr., Texas Tech University, Lubbock, TX, 2006.
- [2] C. K. Alexander and M. N. O. Sadiku, *Fundamentals of Electric Circuits*: McGraw-Hill Higher Education, 2000.
- [3] G. N. Glasoe and J. V. Lebacqz, *Pulse Generators*. New York, NY: McGraw-Hill Book Co., 1948.
- [4] L-3 Communications Pulse Sciences (2006, Nov.). Series T-670 high precision spark gap switches. [Online]. Available: <http://www.titanpsd.com/PDFs/T-670.pdf>.
- [5] W. S. Melville, "The use of saturable reactors as discharge devices for pulse generators," *IEE Proceedings (London), Part 3: Radio and Communication*, vol. 98, pp. 185-207, 1951.
- [6] H. C. Kirbie, M. A. Newton, and P. D. Siemens, "International Magnetic Pulse Compression Workshop," 1991, p. 341.
- [7] W. C. Nunnally, "Stripline magnetic modulators for lasers and accelerators," in *Proc. 3rd IEEE International Pulsed Power Conference Albuquerque, NM*, 1981, pp. 210-213.
- [8] D. Bix, E. Cook, S. Hawkins, S. Poor, L. Reginato, J. Schmidt, and M. W. Smith, "Magnetic switching, final chapter book I: the ATA upgrade prototype," Lawrence Livermore National Laboratory, Livermore, CA 1983.
- [9] D. J. Craik and R. S. Tebble, *Ferromagnetism and Ferromagnetic Domains* vol. 4. New York, NY: John Wiley and Sons, Inc., 1965.
- [10] F. T. Ulaby, *Fundamentals of Applied Electromagnetics*. Upper Saddle River, NJ: Prentice Hall, 2001.

- [11] F. W. Grover, *Inductance Calculations, Working Formulas and Tables*. New York: D. Van Nostrand, 1946.
- [12] W. C. Nunnally, "Magnetic switches and circuits," in *Pulsed Power Lecture Series*: Texas Tech University, 1981.
- [13] J. B. Goodenough, "Summary of losses in magnetic materials," *IEEE Trans. on Magnetics*, vol. 38, pp. 3398-3408, 2002.
- [14] Metglas (2006, Sept.). Powerlite high frequency distributed gap inductor cores: Technical bulletin. [Online]. Available: <http://metglas.com/downloads/powerlite.pdf>.
- [15] D. M. Barrett, "Core reset considerations in magnetic pulse compression networks," in *Proc. of 10th IEEE International Pulsed Power Conference*. vol. 2, 1995, pp. 1160-1165.
- [16] "OrCAD PSpice," 9.10.157 CIS ed Beaverton, OR: OrCAD, Inc., 1999.
- [17] North Star High Voltage (Access Confirmed Nov. 2008). PVM series portable high voltage probes to 60 kV DC. [Online]. Available: <http://www.highvoltageprobes.com/PDF/Vmonad.pdf>.
- [18] Pearson Electronics Inc. (Access Confirmed Nov. 2008). Pearson Current Monitor Model 101. [Online]. Available:<http://www.pearsonelectronics.com/datasheets/standard-ct/101.pdf>.

Chapter 3: Spiral-Strip Pulse Transformer

3.1 Pulse Transformer Design Constraints

The pulse transformer is a critical element to the power conditioning circuit operation for its roles in inductively-storing the energy input from the FCG, stepping up the voltage from the primary winding to the secondary winding, and electrically isolating the primary and secondary circuits. Failure of the transformer can result in poor energy delivery to the secondary circuit and failure of the overall system operation. Several design constraints were in place for the transformer to be compatible with the other system components.

First, the transformer must be capable of charging the high voltage capacitor of the RF source. The risetime of the secondary current is significantly increased for low impedance loads. The current risetime is further increased for a transformer with a large secondary self-inductance and a non-ideal coupling factor. A slow current and voltage rise is detrimental to the energy delivery to the load. Therefore, a low load impedance requires the secondary self inductance to also be low if the coupling factor is non-ideal. This constraint places limitations on the type of transformer selected and the step-up ratio of the transformer.

The second design constraint limits the lower value of the primary inductance. This constraint provides compatibility with the current source, the FCG. The FCGs under development by TTU are designed to drive inductive loads on the order of microhenries. Therefore, the minimal primary inductance of the pulse transformer was mutually agreed upon between MU and TTU to be 1 μH .

The third constraint involves the input energy from the FCG. Previous experiments had been conducted for the FCGs driving 3 μH loads. No data was initially available for the FCGs driving a 1 μH load, so a working assumption was to expect between 30-60 kA from the FCG, corresponding to an energy range of 450-1800 J.

The high voltage output of the transformer secondary provides the fourth constraint. The secondary must be capable of withstanding voltages on the order of 100s of kV. Adequate insulation techniques are required to enable the transformer to hold off these voltages between its secondary windings without electrical breakdown.

The final constraints involve compliance with the overall system requirements. The transformer must be light, compact, and robust. Unnecessary weight in the transformer greatly increases the cost and complexity of transporting and delivering the overall system. The transformer must fit within the system size constraints. In particular, the diameter of the transformer is limited to 15.24 cm, and the transformer length must be limited to allow space for the other power conditioning components without exceeding the allotted system length. Finally, the transformer must be robust enough to be transported or stored for long periods without loss of functionality. This requires the transformer to be relatively simply constructed and mechanically sound.

While the first and second constraints require low inductance windings, the third and fourth constraints require the transformer to be large enough to handle large currents in the primary winding and large voltages across the secondary. These opposing requirements, combined with the overall system size requirements, make the geometry of the transformer a significant design factor.

These five constraints form the basis upon which the transformer design is based. From these constraints, the transformer was designed and modeled, and a manufacturing process for experimental characterization and implementation with a full system was developed.

3.2 Pulse Transformer Selection

Several of the design constraints outlined in the previous section impact the selection of the type of pulse transformer. In particular, the constraints for low winding inductances and light weight greatly influence the selection of a transformer concept. First, the lower limit for the primary self inductance was set at 1 μH for compatibility with the FCG. The secondary self-inductance is also limited to reduce the leakage inductance that could slow the increase of the output current. The inductance of the transformer windings is proportional to $\mu_0\mu_r$. Choosing a transformer core with a low μ_r can greatly reduce the winding inductances to values on the order of microhenries. Second, the long risetime of the FCG output pulse and large amount of inductive energy storage would require a very large ferromagnetic core to prevent core saturation. Based upon the discussion of the saturating magnetic cores from the previous chapter, a voltage on the order of tens of kilovolts applied during the several microseconds of FCG operation would require a transformer core even larger than those used in the magnetic switches to avoid saturation. The number of windings cannot be increased significantly to reduce the core size due to the limitations on the winding inductances. Third, a ferromagnetic core can contribute a significant amount of the total weight of a pulse transformer. A transformer without a ferromagnetic core very clearly reduces the transformer weight and also facilitates for the construction of transformer windings of

low inductance. A non-magnetic core transformer can also be designed large enough to handle the high currents and high voltages of the system while meeting the space requirements of the system. A significant disadvantage of removing a ferromagnetic core from the transformer is reduced flux coupling between the primary and secondary windings, increasing the leakage inductance. Despite the reduced coupling, a non-magnetic core is necessary for this system.

Unique designs were previously developed for high power pulse transformers that eliminated the ferromagnetic core for low weight and high frequency response while compensating for coupling issues. The concepts behind these designs are often attributed to Martin and Rohwein [1]. The transformers utilize a spiral-strip geometry with a non-magnetic core [2, 3]. The windings are formed by wide conducting foils rather than wires. Improved coupling is achieved by overlaying the foil strips in a spiral geometry. The coupling will still be non-ideal, but it can be improved by including ferrite bars in or around the transformer to form a partial magnetic core that does not present many of the disadvantages of a full magnetic core [4, 5]. Electrical insulation is achieved by winding plastic dielectric films between each successive layer of the spiral. Additional insulation between turns can be achieved by vacuum-impregnating the windings with a dielectric to remove air pockets. The foils are often tapered to prevent breakdown between overlapping edges of adjacent layers of the spiral [1]. The Martin transformer is based upon an autotransformer geometry with the primary inputs in the center of the larger secondary winding, and the Rohwein transformer usually consists of electrically isolated windings [1, 2, 6]. In summary, the transformer concepts of Martin and Rohwein provide high power capabilities with an acceptable primary to secondary coupling. The

geometries allow the removal of a ferromagnetic core, which reduces the transformer weight and the winding inductances and allows implementation with the FCG source. Therefore, the spiral-strip pulse transformer with a non-magnetic core was chosen as the transformer concept for implementation in the power conditioning system. The term non-magnetic core is used in place of the more common term air-core for accuracy because, as will be described later, a liquid dielectric was used in place of air due to the high voltage requirements.

3.3 Pulse Transformer Design Equations

The design of non-magnetic core pulse transformers has been previously analyzed [6-8]. The subsequent derivations of spiral-strip self-inductance and leakage inductance follow the derivations of Aslin and Chao [7]. Figure 19 shows the ideal shape of the conductive windings as a right circular cylinder.

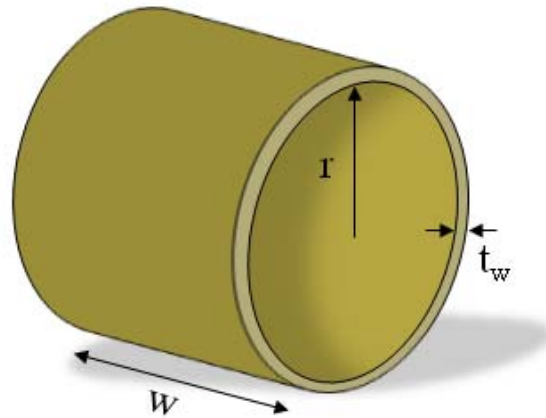


Figure 19. Right circular cylinder geometry of conductive windings

Variable r [m] is the average radius of the windings, w [m] is the width of the foils, and t_w [m] is the total thickness of the windings, including insulation. In this geometry, it is assumed that $t_w \ll r$ so that the radius of all current carrying conductors is approximately r . It is also assumed that $r \ll w$ so that the end effects of the magnetic flux density can be

neglected. With these assumptions in place, the magnetic flux density, B [Wb/m²], along the axis of the cylinder for a given winding is given by equation (17).

$$B = \frac{\mu_0 n_w i}{w} \quad (17)$$

The variable n_w represents the number of turns in the spiral winding, and the variable i [A] is the current in the winding. The total flux, Φ [Wb], from the winding of interest is then given as equation (18).

$$\Phi = BA = \frac{\mu_0 n_w i \pi r^2}{w} \quad (18)$$

The flux linkage, λ [Wb], is equal to the product of the flux times the number of turns.

$$\lambda = \frac{\mu_0 n_w^2 i \pi r^2}{w} \quad (19)$$

The inductance of the winding, L [H], can then be found as the ratio of the flux linkage to a unit current.

$$L = \frac{\lambda}{i} = \frac{\mu_0 n_w^2 \pi r^2}{w} \quad (20)$$

The derivation from Aslin and Chao goes on to correct equation (20) in the case that the assumption that $r \ll w$ is not valid by adding the term r in the denominator.

$$L = \frac{\mu_0 n_w^2 \pi r^2}{w + r} \quad (21)$$

Equation (21) is the final design equation that can be used to calculate the primary and secondary self-inductances.

The equation for the leakage inductance of the transformer can be obtained from the transformer geometry in a similar way. From Lenz's Law, the magnetic flux densities of the primary and secondary windings should cancel [7].

$$\frac{\mu_0 n_p i_p}{w} = \frac{\mu_0 n_s i_s}{w} \quad (22)$$

The subscripts s and p denote the values for the secondary and primary windings, respectively. Equation (22) does not apply within the winding thickness, t_w , and the magnetic flux densities do not completely cancel in this region [7]. By the relation $B = \mu H$, the peak magnetic field, H_{peak} [A/m], of the primary winding can be found by equation (23).

$$H_{peak} = \frac{n_p i_p}{w} \quad (23)$$

Equation (23) is applicable to the pulse transformers built for the power conditioning system. The transformers were built with electrically-isolated primary and secondary windings rather than as an autotransformer. The average value of a magnetic field decreasing radially from the current path can be related to the peak magnetic field by equation (24) [7].

$$\overline{H^2} = \frac{1}{3} H_{peak}^2 = \frac{1}{3} \frac{n_p^2 i_p^2}{w^2} \quad (24)$$

The energy stored in the magnetic field can then be calculated by equation (25). The volume, v_{tw} [m³], of the winding thickness is calculated by $v_{tw} = 2\pi r w t_w$.

$$W_H = \frac{1}{2} \mu_0 \overline{H^2} v_{tw} \quad (25)$$

Substituting for v_{tw} and $\overline{H^2}$ [A²/m²] in equation (25) results in equation (26).

$$W_H = \frac{\mu_0 \pi r t_w n_p^2 i_p^2}{3w} \quad (26)$$

The energy in the magnetic field of the windings can also be described by equation (27).

The leakage inductance is represented as L_l [H].

$$W_H = \frac{1}{2} L_l i_p^2 \quad (27)$$

Using equations (26) and (27) and solving for L_l results in equation (28).

$$L_l = \frac{2 \mu_0 n_p^2 \pi r t_w}{3 w} \quad (28)$$

Equation (28) can then be used to predict the leakage inductance based upon the geometry of the windings previously established by the design of the primary and secondary self inductances.

Another crucial design parameter for the pulse transformer is dielectric film thickness. Since the maximum turn to turn electric field will appear on the primary winding, that winding can be used to determine the minimum thickness of the dielectric sheets. The following design equation was used in this investigation to determine the number of films per turn required.

$$N = \frac{V_{peak}}{n E_{max} t_d} + 1 \quad (29)$$

The symbol N is the number of dielectric sheets, and the peak voltage across the winding is V_{peak} [V]. The number of turns for the winding is represented by n . The maximum dielectric strength of the insulating material is represented by E_{max} [V/m]. The thickness of each dielectric sheet is represented by t_d [m]. It is often good practice to add one to the calculation for N due to pinholes in the dielectric film. Pinholes can result from defects or damage of the dielectric, so it is safe practice to assume one or more sheets has pinholes but that they will not align. Equation (30) can then be used to estimate the total winding thickness, t_w .

$$t_w = (n_p + n_s)[(N + 1)t_d + t_c] \quad (30)$$

The variable t_c [m] is the thickness of the conductive foil. Equation (30) assumes that an equal number of dielectric sheets and the same conductor thickness are used for the primary and secondary windings but can be easily manipulated to account for differences between the two.

3.4 Winding Analysis

Spiral-strip pulse transformers can be constructed as either one or two-winding transformers [1]. With one winding, the primary and secondary windings are electrically connected, with the primary winding constituting a portion of the secondary winding, forming an autotransformer. As a two-winding transformer, the primary and secondary are electrically isolated, physically separate windings. In consideration of whether to build the MU transformer as an autotransformer or two-winding transformer, the overall power conditioning circuit must be considered. Figure 20 shows the typical arrangement of components in the primary circuit. In this arrangement, the opening of the fuse causes both terminals of the primary winding to go to some non-zero potential with respect to ground. This arrangement results in a floating secondary for an autotransformer. A floating secondary is disadvantageous when making voltage measurements across the secondary due to the need to take two differential measurements with respect to ground. An autotransformer could still be used if the circuit positions of the primary winding and fuse were switched. However, this arrangement would then require two voltage measurements for the fuse diagnostics. Therefore, to enable single voltage measurements on the fuse and load, the circuit arrangement of Figure 20 was used during this investigation, and a transformer with electrically-isolated windings was selected.

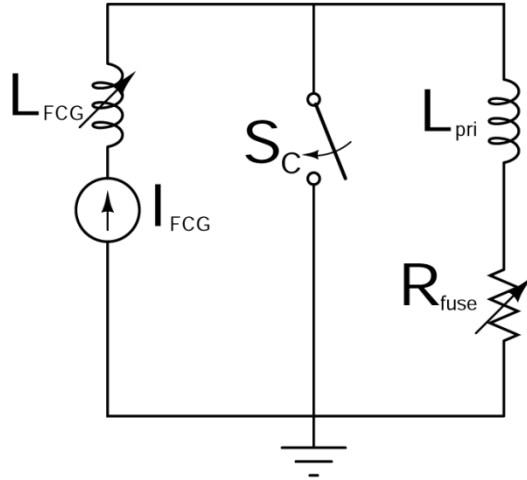


Figure 20. Typical primary circuit component arrangement

During the experimental evaluation of the first transformer prototypes, it became apparent that the transformers with electrically-isolated windings were especially prone to electrical breakdown where the primary and secondary windings were adjacent. It is, therefore, beneficial to analyze the voltages between adjacent windings of the primary and secondary. There is one restriction on the placement of the high voltage secondary terminal. To provide adequate electrical insulation of the high voltage terminal from the rest of the transformer, the high voltage terminal must be the innermost section of the winding, connecting to a conductive rod on the cylindrical axis of the transformer. This restriction means that the secondary winding is required to be the innermost winding with the primary wrapped around it. As previously mentioned, one of the secondary terminals is at ground potential to enable voltage measurements with a single high voltage probe, so the outermost section of the secondary winding will be connected to ground.

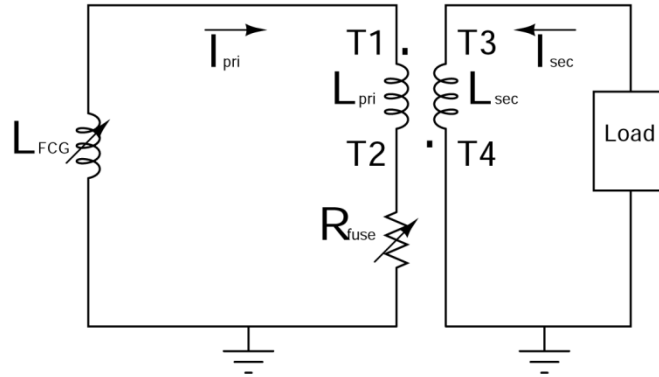


Figure 21. Simplified circuit with labeled transformer terminals

Figure 21 shows a simplified circuit with a generic load and the four transformer terminals labeled $T1$, $T2$, $T3$, and $T4$. The dot convention in Figure 21 will be used in this analysis, and it will be seen that the opposite convention could be used for a transformer with windings in the opposite direction with only the effect of the reversal of secondary voltage polarity. By estimating the potential of each terminal before and after fuse opening, one can determine which two terminals to place adjacent to each other in the winding to minimize the inter-winding voltage stress on the dielectric film insulation.

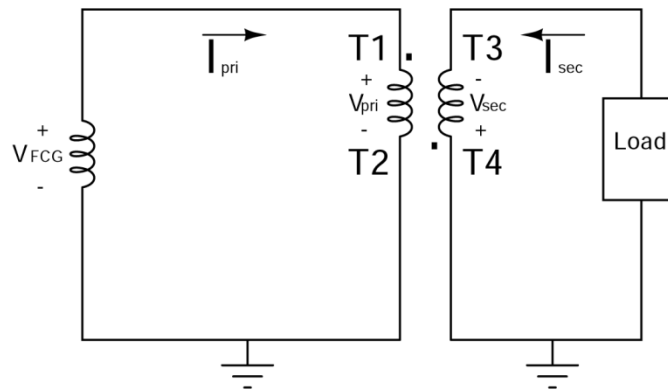


Figure 22. Equivalent circuit with voltage polarities before fuse opening

Figure 22 shows the equivalent circuit before fuse opening. The FCG is driving a current in the direction of I_{pri} , and a current is generated in the secondary circuit in the direction of I_{sec} . The fuse is approximated for this analysis as a short circuit before opening, so $T2$ is at ground potential. The FCG causes the current to build in the primary

inductance, so the voltage across the winding is polarized as in Figure 22, with $T1$ positive with respect to ground at the magnitude of the FCG output voltage. As previously mentioned, it is desirable to have one of the secondary terminals grounded to aid in voltage measurements, so $T4$ was chosen as the grounded terminal. The voltage generated across the secondary is polarized as in Figure 22, with $T3$ negative with respect to ground.

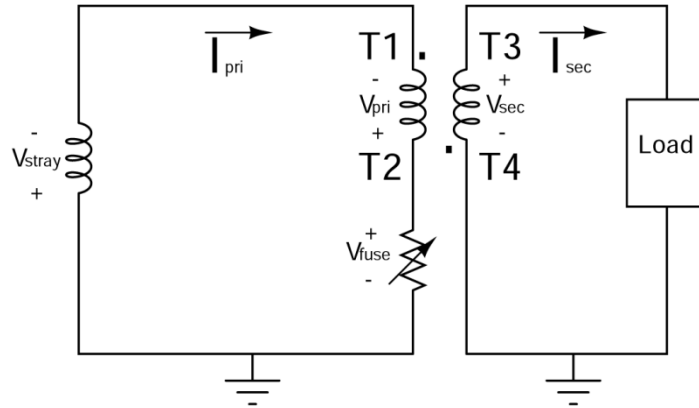


Figure 23. Equivalent circuit with voltage polarities after fuse opening

Figure 23 depicts the circuit as the fuse is opening and I_{pri} decreases towards zero. A large voltage is generated across the fuse as the resistance increases. Since I_{pri} has the same direction, the voltage across the fuse results in $T2$ rising to the voltage $+V_{fuse}$ with respect to ground. With a negative rate of current change in the primary winding, the voltage polarity across the primary and any stray inductance in the circuit now has the opposite polarity of that during the current rise. The voltage of $T1$ with respect to ground is now $V_{fuse} - V_{pri} = V_{stray}$. If the stray inductance in the circuit is negligible, then $T1$ should be at ground potential. Terminal $T4$ remains grounded during this stage of operation, but the voltage induced across the secondary winding is reversed. Therefore, $T3$ now has a positive polarity with respect to ground, +HV. A summary of the voltages relative to ground is provided in Table 5.

Table 5. Terminal Voltages with Respect to Ground

	Before Fuse Opening	During Fuse Opening
<i>T1</i>	$+ V_{FCG}$	$+ V_{fuse} - V_{pri} = V_{stray}$
<i>T2</i>	0	$+ V_{fuse}$
<i>T3</i>	$- V_{sec}$	$+ HV$
<i>T4</i>	0	0

Analysis of Table 5 determines whether to wind *T1* or *T2* adjacent to *T4*. Before fuse opening, *T2* is at the same potential as *T4*. However, since the output voltage of the FCG is only on the order of 10s of kV, this voltage could be held off with comparable dielectric thicknesses as used in the intra-winding insulation of the primary and secondary. When examining the voltages during fuse opening, the voltage of *T2* rises to the full voltage across the fuse. The voltage of *T1*, however, is the fuse voltage minus the voltage across the primary inductance. If the stray inductance is minimal, this voltage is close to ground. Since the fuse voltage can be greater than 100 kV, placing *T2* adjacent to *T4* requires additional dielectric films to prevent electrical breakdown of the insulation. It is desirable to minimize the thickness of the insulation to improve coupling between the transformers. Therefore, the winding configuration can be determined with *T1* adjacent to *T4*. Figure 24 displays the winding configuration shown in this analysis. The windings both have the same orientation, running clockwise as the radius of the winding grows.

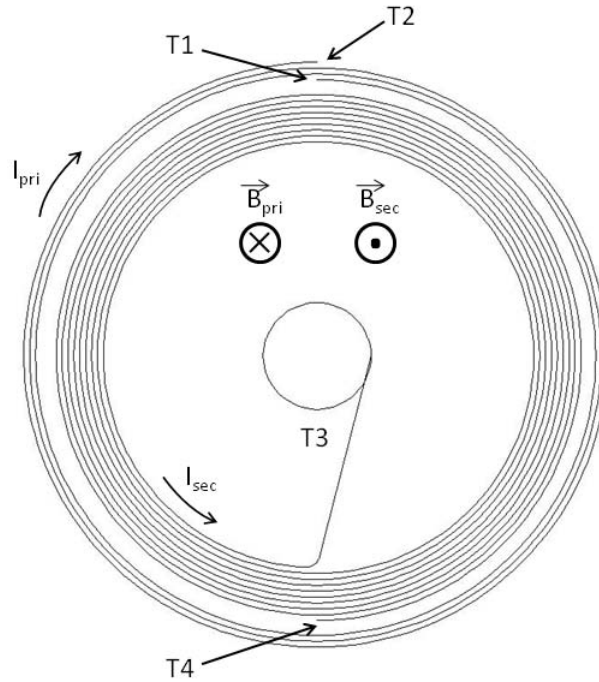


Figure 24. Transformer cross-section of winding orientation and terminal locations

The windings can also be oriented in the opposite direction, resulting in the opposite dot convention as shown in Figure 21 and the opposite polarity of the secondary voltages before and during fuse opening. Selection of the relative winding orientation could be important for some loads that require a particular voltage polarity.

3.5 Analysis of the Step-up Ratio

The step-up ratio of the transformer is designed to maximize the peak voltage reached on the secondary capacitor. With the primary self-inductance, L_p [H], set to 1 μ H for compatibility with the FCGs, the optimal step-up ratio can be used to design the secondary self-inductance, L_s [H]. The turn ratio, n , can be defined from the primary and secondary inductances by equation (31) [1].

$$n = \sqrt{\frac{L_s}{L_p}} \quad (31)$$

The analysis of the optimal step-up ratio is complicated by the dynamic behavior of the opening switch. Numerical modeling of the circuit with the dynamic behavior of the fuse resistance makes the analysis possible. For brevity, not all of the details of the numerical modeling of the optimal step-up ratio are given in this section, but the circuit and relevant details are provided for context of the results. The behavior of the fuse resistance is thoroughly described in Chapter 4, and the derivations of the required current derivatives are presented in Appendix A. The method by which the current derivatives can be used to numerically simulate the circuit with a dynamic fuse resistance is detailed in Appendix B for a similar circuit.

The equivalent circuit for the power conditioning system after generator operation is given by Figure 25. After operation of the FCG or FCG simulator, the inductance of the generator is ideally zero. For the case in which the generator inductance is not zero, the voltage across the inductance will cause the crowbar switch to close and short out the generator. Thus, the generator inductance is no longer included in the circuit of Figure 25. The capacitance is represented as C [F], and the fuse resistance is represented by R_s [Ω]. The primary and secondary currents are given as I_p [A] and I_s [A], respectively. The transformer has been replaced by its T-equivalent [1]. For a coupling coefficient k , the primary leakage inductance, L_{lp} [H], and secondary leakage inductance, L_{ls} [H], can be written as equation (32) and equation (33), respectively [1].

$$L_{lp} = \frac{L_s}{n^2}(1 - k) \quad (32)$$

$$L_{ls} = L_s(1 - k) \quad (33)$$

The magnetizing inductance referred to the primary, L_{mp} [H], can be expressed by equation (34) [1].

$$L_{mp} = \frac{kL_s}{n^2} \quad (34)$$

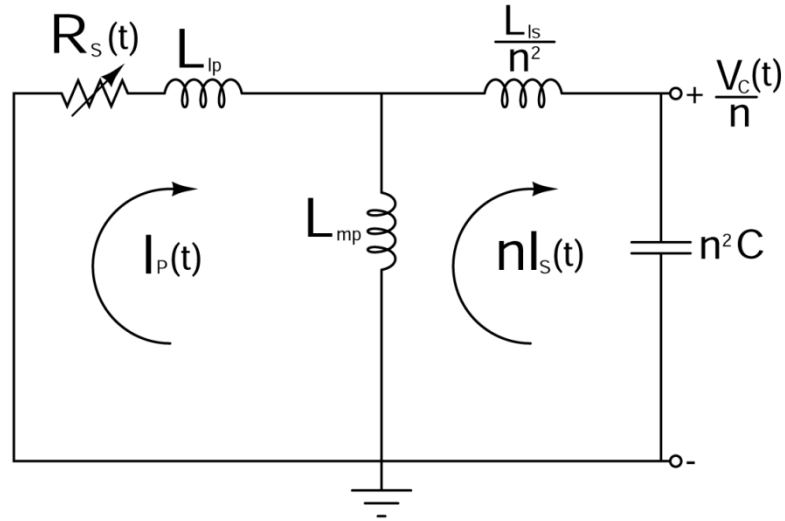


Figure 25. Power conditioning circuit after FCG operation with transformer T-equivalent

As shown in Appendix A, solutions of the current derivatives for the circuit of Figure 25 require the assumption of ideal transformer coupling. The circuit is then simplified to Figure 26.

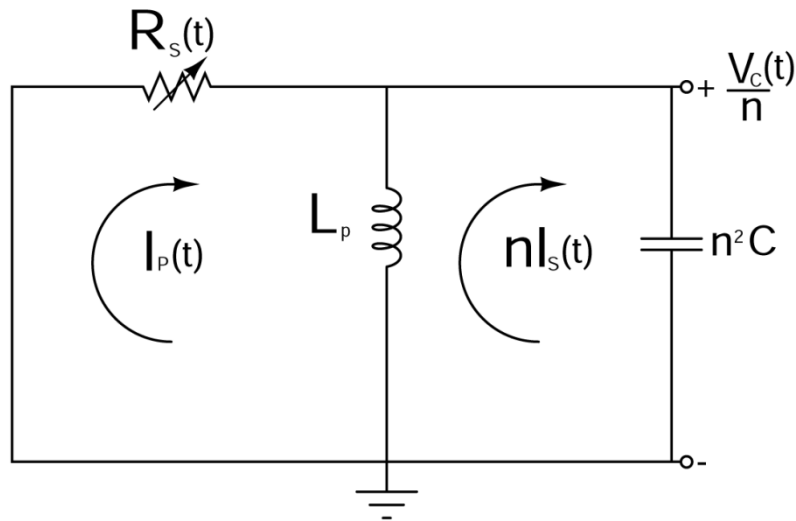


Figure 26. Power conditioning circuit after FCG operation with ideal transformer coupling

The circuit is now a source-free parallel RLC circuit with a varying resistance. The wide range of fuse resistance values between its initial low resistance and final high resistance result in the circuit behavior changing from overdamped to underdamped.

The analysis of the step-up ratio examined the peak voltage to which the capacitor was charged while changing only the turn ratio, n . The other parameters were kept equal for all cases. The analysis assumed no initial charge on the capacitor. The primary current and fuse resistance values at the end of generator operation were chosen based on typical values as 40 kA and 0.61 Ω , respectively. The results of the analysis are displayed for capacitances of 250 pF and 900 pF, which are extreme values derived in Chapter 5. Figure 27 displays the peak voltage across the secondary capacitance for values of n from 1 to 100. Although the fuse resistance values used in this analysis are representative of typically-implemented fuses, the actual peak voltage on the secondary capacitance is dependent on the parameters of the implemented fuse.

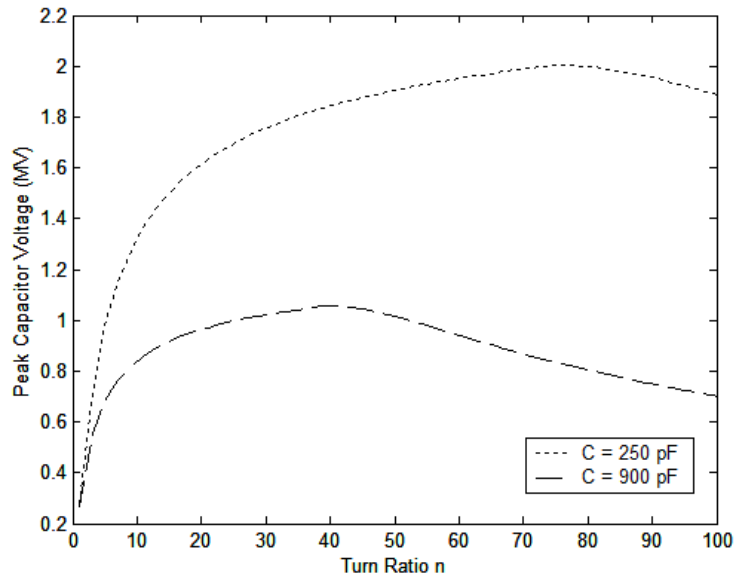


Figure 27. Peak capacitor voltage for multiple turn ratios

The optimal turn ratio for the 250 pF and 900 pF capacitors are about 80 and 40, respectively. This analysis demonstrates how without other constraints, the transformer can be implemented with a high turn ratio to maximize the peak charging voltage. However, practical limitations limit the step-up ratio in the real system. Primarily, the size constraints of the system limit the number of windings that can fit into the required diameter. The minimum primary self-inductance is 1 μ H for compatibility with the FCG. A large turn ratio of the same order of the optimal ratios from Figure 27 translates into a secondary self-inductance on the order of millihenries. From equation (21), several turns within a diameter less than 15.24 cm are required for inductances of just several microhenries. Therefore, much higher inductances are impractical to implement. Additionally, adding multiple turns will decrease the coupling factor, k , between the primary and secondary windings. A lower coupling factor could reduce the peak voltage from that predicted in Figure 27.

Although there are physical and practical limitations to increasing the turn ratio to the optimal level, the benefits of the transformer can still be achieved at much lower turn ratios. The peak voltage increases very quickly for a turn ratio up to about $n = 10$. Beyond a turn ratio of 10, the benefits of adding additional inductance to the secondary winding are increasingly reduced. For a turn ratio between 3 and 5, the peak capacitor charging voltage is already several hundred kilovolts. At this magnitude, the system is limited by the dielectric strength of the RF source components, and the step-up ratio does not need to be increased further.

3.6 Pulse Transformer Construction

The dimensions of the pulse transformer were determined by equations (21). The outer radius was designed to be the maximum of 15.24 cm to reduce the number of turns required to obtain the desired inductance. The primary self-inductance was set at 1 μH to serve as the inductive energy store for the FCG output. The secondary self-inductance was designed to be 9 μH for a turn ratio of 3. The transformers were designed to operate in oil to at least 360 kV. Table 6 gives the dimensions used in the MU pulse transformers.

Table 6. Pulse Transformer Winding Parameters

Winding	Inductance (μH)	Turns	Avg. Radius (m)	Avg. Width (m)
Primary	1	3	0.075	0.12
Secondary	9	9	0.069	0.10

The pulse transformers were constructed in a spiral-strip geometry on a cylindrical form. The secondary winding was wound directly on the cylindrical form, and the primary was wound around the secondary to form the outer winding. The outer diameter and length of the transformers are approximately 15.24 cm. Both windings had two layers of mylar insulation placed on both sides before winding. Therefore, upon winding, four layers of mylar insulation separated adjacent layers. Breakdown failures between the primary and secondary windings in the original transformer prototypes necessitated additional layers of insulation between the two windings. The high voltage output terminal was located on the axis of the cylinder to provide adequate distance for electrical isolation. Three tabs extended from the windings to make the remaining connections. Figure 28 shows an example transformer.



Figure 28. Spiral-strip pulse transformer

The conductors were made with 0.1178 mm thick copper foils. Both windings had a small taper in width to prevent breakdown due to high fields between overlapping edges. The secondary winding width had a taper between 7.62 cm and 10.16 cm. The primary winding width was tapered between 10.16 cm and 12.7 cm. The foil edges were folded and rolled flat to give a slight increase to the radius of the edge, reducing field enhancement, and eliminating the presence of burrs that result from cutting the foils to the designed width. The mylar insulation was 0.127 mm thick per film. The mylar was rated at 500 V/mil or about 197 kV/cm under DC conditions. A value of E_{max} for thermoplastic dielectric films under pulsed conditions of 2 kV/mil or 787 kV/cm was assumed. With four layers of film per turn, the dielectric strength is 40 kV per turn. The maximum pulsed voltages designed for the primary and secondary windings are thus 120 kV and 360 kV, respectively. Since the assumed dielectric strength of 787 kV/cm is somewhat conservative, the actual peak voltage holdoff of the transformer can be much higher. The film widths were cut to 15.24 cm to provide adequate overlapping insulation beyond the edges of the copper foils.

PVC piping provided the cylindrical form for the transformer. The outer diameter of the pipe was approximately 10.16 cm, and the pipe was cut to 15.24 cm in length. Slits

were cut 180° apart on both ends of the pipe to hold plastic inserts. The plastic inserts provided support for the center high voltage output. The high voltage output was made with 2.54 cm diameter copper pipe with end caps. The innermost section of the secondary winding extended through a slit in the PVC and made a connection to the copper pipe. Connections could then be made from the copper pipe to the load.



Figure 29. Transformer with center high voltage output connection

References for Chapter 3

- [1] P. W. Smith, *Transient Electronics: Pulsed Circuit Technology*. West Suxxex, England: Wiley, 2002.
- [2] J. C. Martin and I. D. Smith, "High-voltage pulse-generating transformers," U.S. Patent 3456221, July 15, 1969.
- [3] G. J. Rohwein, "A three megavolt transformer for PFL pulse charging," *IEEE Trans. on Nuclear Science*, vol. NS-26, pp. 4211-4213, 1979.
- [4] G. J. Rohwein and S. R. Babcock, "A compact high voltage pulse generator," in *Conf. Rec. of 21st International Power Modulator Symposium*, 1994.
- [5] G. J. Rohwein, R. N. Lawson, and M. C. Clark, "A compact 200 kV pulse transformer system," in *Proc. 8th IEEE International Pulse Power Conference* San Diego, CA, 1991.
- [6] J. P. O'Loughlin, J. D. Sidler, and G. J. Rohwein, "Air core pulse transformer design," in *Proc. 18th Power Modulator Symposium*, 1988, pp. 325-330.
- [7] H. Aslin and P. Chao, "Pulse transformer design study," Physics International Company, ECOM-75-1340-F, San Leandro, CA 1975.
- [8] P. Champney and C. Eichenberger, "Explosively driven 1 MV output air-core pulse transformer design," Pulse Sciences, Inc., PSI-FR-3358-01, San Leandro, CA 1988.

Chapter 4: Exploding Wire Fuse

4.1 Opening Switch Background

In inductive energy storage systems, an opening switch must be employed to divert the stored energy into the load [1]. An ideal opening switch would rise from zero impedance to infinite impedance instantaneously and dissipate no energy. All real switches will have non-zero conducting resistances, a non-zero switching time, and finite resistances while open, so energy will be dissipated in the switch. For many opening switches in high power inductive energy systems, the energy dissipation in the switch or the opening mechanism of the switch results in component destruction. Thus, many opening switches are single shot devices [2]. Schoenbach, Kristiansen, and Schaefer summarize the desirable characteristics of an opening switch as the following: long conduction times, large current conduction with low losses, fast rise of impedance during opening, high impedance after opening, high stand-off voltage, and for repetitive switches, fast recovery [2]. Several technologies have previously been developed to achieve these characteristics, including explosive opening switches, plasma erosion switches, exploding wire fuses, and several more [2].

Explosive opening switches use explosives or shaped charges to mechanically sever the conducting path to be opened [3]. Explosive opening switches can interrupt currents of more than 1 MA with opening times of just under 1 μs to 10s of μs [1, 2]. The opening time of explosive opening switches is limited by the motion of the detonation products, and they are generally too slow for application in this investigation. Plasma erosion switches use a plasma source to provide a conductive medium in an anode-cathode gap.

Plasma processes then result in a large increase in switch impedance. Plasma erosion switches have been used to interrupt currents of 100s of kA and hold off 100s of kV in opening times on the order of 10s of ns [2]. However, plasma erosion switches have relatively short conduction times on the order of 10s to 100s of ns, excluding their use with FCGs. Additionally, the large amount of equipment needed for the switch makes it impractical for compact applications. Exploding wires have been of particular interest due to their high current conduction, large impedance change upon opening, and relatively simple construction. One of the first proposals for the use of an exploding wire fuse as an opening switch in an inductive energy storage system was made by Janes and Koritz [4]. The fuse resistance increases rapidly as the conducting wires are heated through the solid, liquid, and vapor phases. The fast heating and transition between states results in explosion of the fuse wires, making the switches single use devices. Experiments have utilized exploding metallic fuses capable of interrupting currents of several MA and holding off voltages of 100s of kV [2]. Current interruption times are dependent on the circuit, but opening times of 10s of ns to 100s of ns are typical.

A priority for the inductive energy system in this investigation is for high current carrying capability of several 10s of kA and a fast rate of impedance change to deliver a fast high power pulse to the load. A comparison by Schoenbach based upon these two parameters shows explosive opening switches, plasma erosion opening switches, and fuses as similarly capable of handling very high currents with fast rates of impedance rise [1]. Due to the limitations of explosive opening and plasma erosion opening switches and the relative simplicity of fuse construction, the exploding wire fuse was chosen as the opening switch for this investigation.

4.2 Modeling the Dynamic Fuse Resistance

4.2.1 Action-Dependent Resistivity Equations

Exploding wire fuses have been the subject of coordinated research for more than 50 years. During the first conferences on exploding wire research in the late 1950s and 1960s, several models of the mechanisms of wire explosion and the increase of resistivity were proposed [5]. The types of wire explosions can be classified based upon the energy dissipated in the wire and the rate of energy dissipation [6]. Since the system energy of the FCG and inductive storage system is sufficient for full vaporization of the wires and the time scale for energy dissipation is on the order of microseconds, the type of wire explosion considered in this investigation is the fast explosion. For fast explosions, physical distortions along the wire are insignificant during fuse heating [6]. It is assumed that heating occurs during a short enough time scale that little energy dissipated in the wires is transferred to the surrounding medium. Models have previously been developed to describe the behavior of wire explosions with equations of state and magneto-hydrodynamics [7, 8]. These models can provide insight into the physical phenomena during the explosion process. However, for modeling and evaluating an exploding wire fuse and its interaction with the circuit, the primary parameter of interest is the fuse resistivity. Therefore, the model presented here is restricted to the resistivity of the wires based upon the previously-demonstrated relationship between resistivity and the specific action or specific energy [9, 10]. The current action and specific energy, which will be described later, can be predicted or calculated from knowledge of the current through and voltage across the fuse.

A comprehensive study of exploding wire data by Heeren resulted in the development of empirically-based equations for the fuse resistivity based on the integral of current action [11]. The integral of current action, given by equation (35), is a parameter often used to predict the point at which the wire reaches vaporization and the wire resistivity begins to rapidly increase [9].

$$h(t) = \int_0^{t_0} i^2(t)dt \quad (35)$$

The point at which the resistivity begins to rapidly rise, denoted h_e , is referred to as the action limit. As will be described later in this chapter, when the action limit is normalized by the cross-sectional area, the result is approximately a constant based on material properties. The curve fitting performed by Heeren is given by equations (36) and (37). Equation (36) predicts the fuse resistivity when h , the current action integral, is less than the action limit, h_e . Equation (37) applies for h greater than the action limit. The symbol ρ [$\Omega \cdot m$] is the fuse resistivity, and the symbol ρ_0 [$\Omega \cdot m$] is the initial fuse resistivity. The symbols D_1 , D_2 , and D_3 are constants found by curve fitting experimental fuse data [11]. The constants D_1 , D_2 , and D_3 for copper are given as 23.9, 2.3, and 118, respectively [11].

$$\rho(h) = \rho_0 \left[1 + D_1 \left(\frac{h}{h_e} \right)^{D_2} \right] \quad (36)$$

$$\rho(h) = \rho_0 \left[D_1 + e^{\frac{h-h_e}{h_e} D_3} \right] \quad (37)$$

Equations (38) and (39) can be used to calculate the fuse resistance as a function of h with a known initial value of fuse resistance, R_0 [Ω].

$$R(h) = R_0 \frac{\rho(h)}{\rho_0} = R_0 \left[1 + D_1 \left(\frac{h}{h_e} \right)^{D_2} \right] \quad (38)$$

$$R(h) = R_0 \frac{\rho(h)}{\rho_0} = R_0 \left[D_1 + e^{\frac{h-h_e}{h_e} D_3} \right] \quad (39)$$

Heeren observed excellent agreement in comparisons of experimental data and the predicted fuse resistivities [11]. Although Heeren notes that equation (37) begins to differ from the actual resistivity for large values of $(h-h_e)$, as yet there is no strict upper limit on the value of h for which equation (37) applies. Specifically, equation (37) does not account for fuse restrike.

Researchers who first studied high currents in exploding wires termed the period of low current the current pause or dwell time and used the term restrike to describe the renewal of high current conduction [12]. The fuse resistivity dramatically falls during a restrike event. The common explanation for restrike is that the electric field exceeds the dielectric strength of the fuse wires and an arc breakdown occurs. As the fuse vapor expands, the mass density decreases to a point where the dielectric strength of the vapor is exceeded and breakdown occurs [11]. Matter around the fuse, the quenching or tamping material, is used to slow the expansion of the fuse and thus delay the reduction in dielectric strength.

For this discussion, it is proposed to classify restrike into two types, although they are not mutually exclusive. First, for high voltage systems, the dielectric strength of the fuse could be exceeded during an early stage of fuse operation. An arc could form within or around the fuse before the wires are fully vaporized. Short fuse geometries, materials with low dielectric strength, or field enhancements could increase the probability of this type of restrike occurring. This first type of restrike will be referred to as arc breakdown due to excessive electric fields prior to full vaporization. The second type of restrike occurs when energy is dissipated in the fuse after the fuse wires have been fully

vaporized. Several researchers have suggested that energy dissipation in the fuse after the fuse has been fully vaporized can result in reduced fuse resistivity regardless of the electric field in the fuse. Tucker and other researchers have presented experimental data that shows the resistivity of the fuse dropping significantly for specific action and specific energies beyond the values at full vaporization [10, 13, 14]. Maisonnier points out that energy deposition in the fuse beyond full vaporization can result in ionization [15]. Tucker refers to theoretical work that predicts metallic vapor at densities of 1 gm/cm^3 to be conductive [14, 16]. Another theory proposed by Lindemuth states that as the metal vapor expands, a point is reached such that the cross-sectional area increases faster than the resistivity, resulting in an overall decrease in resistance [13]. Including the effects of the electric field, researchers also believe that low mass density in the wire can allow avalanche breakdown to occur [11]. Regardless of the mechanisms behind the drop in fuse resistivity, there is evidence that beyond the full vaporization of the fuse wires, there is a collapse of the fuse resistivity. This decrease in resistivity is not mutually exclusive of the first type of restrike. An electric field must still be present for energy dissipation in the fuse beyond full vaporization and, in the case of avalanche breakdown, overcome the reduced dielectric strength of the fuse vapor. However, the distinction between the two types of restrike is made because dielectric failure can occur at any point during fuse operation, but, specifically, the fuse is susceptible to restrike when energy is dissipated beyond the point of full vaporization. This second type of restrike will be referred to as arc breakdown due to excessive specific action. Although the specifics of restrike after full vaporization are undetermined, the knowledge of the specific action or

specific energy levels at which this restrike event occurs allows one to set an upper limit for fuse design.

Examination of fuse resistivity data with respect to the specific action or the specific energy allows for an approximation of the fuse resistivity after the point of peak resistivity. Although the behavior of the resistivity after the peak value is not completely understood, data presented by Tucker and Toth for several materials can be utilized to formulate an approximation [10]. Figure 30 is an example of a resistivity vs. specific action plot.

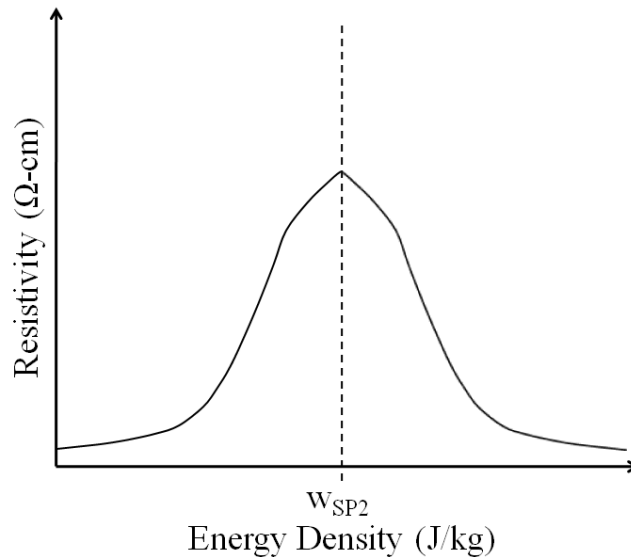


Figure 30. Illustrative plot of the resistivity rise and fall about the maximum

For many commonly-used fuse materials, including copper, silver, and gold, the drop in fuse resistivity is approximately symmetrical to the rise in fuse resistivity about the point of maximum resistivity, w_{sp2} [J/kg]. Since operation of the fuse as an opening switch will ideally not reach this resistivity collapse, an approximation of the resistivity collapse is sufficient for understanding the circuit behavior corresponding to fuse restrike. Therefore, based on the symmetry of the resistivity profile, equations (40) and (41) can be written for values of h greater than h_b , the action at full vaporization or burst. Equations (38),

(39), and (41) can then be used to predict the fuse resistance at all specific action values of interest.

$$\rho(h) = \rho_0 \left[D_1 + e^{\frac{h_b - h_e}{h_e} D_3} \right] e^{\frac{h_b - h}{h_e} D_3} \quad (40)$$

$$R(h) = R_0 \frac{\rho(h)}{\rho_0} = R_0 \left[D_1 + e^{\frac{h_b - h_e}{h_e} D_3} \right] e^{\frac{h_b - h}{h_e} D_3} \quad (41)$$

The previous equations can be numerically modeled when h_e is known or calculated. To determine h_e , the current during generator operation must be known. The generator runtime, t_r [s], is defined as the time during which the FCG produces the rising current signal in the inductive store. Heeren provides an equation for an FCG current, i_p [A], in terms of its peak current, I_{p0} [A], the generator runtime, and an exponential curve-fitting factor, ε , used to adjust the waveform to match experimental data [11].

$$i_p(t) = \frac{I_{p0}}{e^\varepsilon - 1} \left(e^{\frac{\varepsilon t}{t_r}} - 1 \right) \quad (42)$$

Calculating h_e can be accomplished by applying equation (42) for the exponential current rise from the FCG to equation (35) for the current action integral. The integral of equation (43) can be solved to provide an expression, equation (44), for the fuse action limit based on I_{p0} , t_r , and ε .

$$h_e = \int_0^{t_r} \left(\frac{I_{p0}}{e^\varepsilon - 1} \right)^2 \left(e^{\frac{\varepsilon t}{t_r}} - 1 \right)^2 dt \quad (43)$$

$$h_e = \frac{I_{p0}^2 t_r}{\varepsilon (e^\varepsilon - 1)^2} \left[\frac{1}{2} e^{2\varepsilon} - 2e^\varepsilon + \frac{5}{2} \right] \quad (44)$$

With a value for h_e and initial values for the current and resistivity, a numerical analysis can be implemented to determine current, integral of current action, resistivity, and many more system and fuse parameters in time. A MATLAB program was written and

implemented to perform this numerical analysis [17]. An example of the program with details is included in Appendix B, and the derivations of the necessary circuit equations can be found in Appendix A. The numerical analyses were utilized in the following subsections to investigate the resistance rise of the fuse, the effects of different initial fuse resistances, and the fuse energy dissipation.

4.2.2 Fuse Resistance

The equations presented in the previous sub-section can be implemented to examine the resistance rise of a fuse and its influence on circuit behavior. As detailed in Appendix A, the full solutions necessary for performing a numerical analysis of the power conditioning system with an RF source and non-ideal transformer coupling cannot be determined. Therefore, for the analyses of the fuse resistance and energy dissipation in this section, a resistive load must be considered. Since the fuse resistance and primary current are the parameters of interest in these analyses, many of the results are similar to those with the capacitive load of the RF source. Additionally, these results apply directly to the use of an HPM source. The circuit is shown in Figure 31, and Table 7 summarizes the fixed simulation parameters.

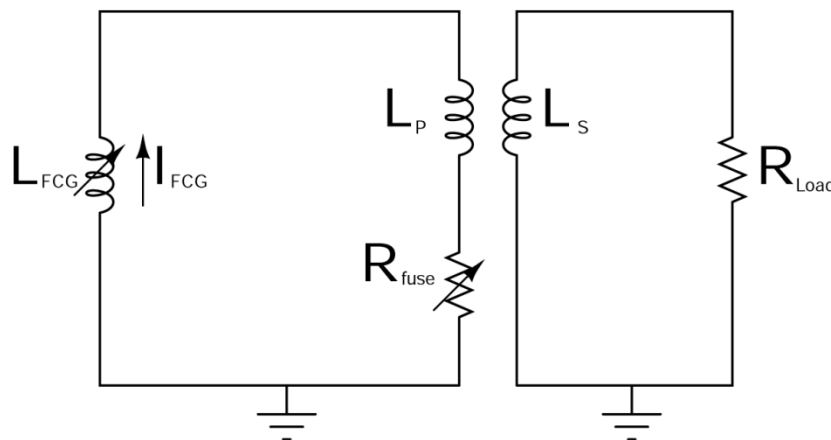


Figure 31. Power conditioning system used for numerical simulations

Table 7. Fixed Simulation Parameters

Peak Current (kA)	L_P (μH)	L_S (μH)	k	R_{Load} (Ω)
40	1	9	0.8	18
Fuse Length (cm)	Fuse Area (mm^2)		R_θ ($\text{m}\Omega$)	
7	0.1795		6.7	

The resistance rises very slowly during the 10 μs generator operation to a value of $(D_I + 1)$ times the initial value, where D_I is a material-dependent constant used in equations (36)-(41). The resistance then rises very rapidly to a peak value of 9.8 Ω . The maximum specific action and maximum specific energy do not exceed the limit past full vaporization, so no restrike occurs. More detail on these maxima is given later in this chapter.

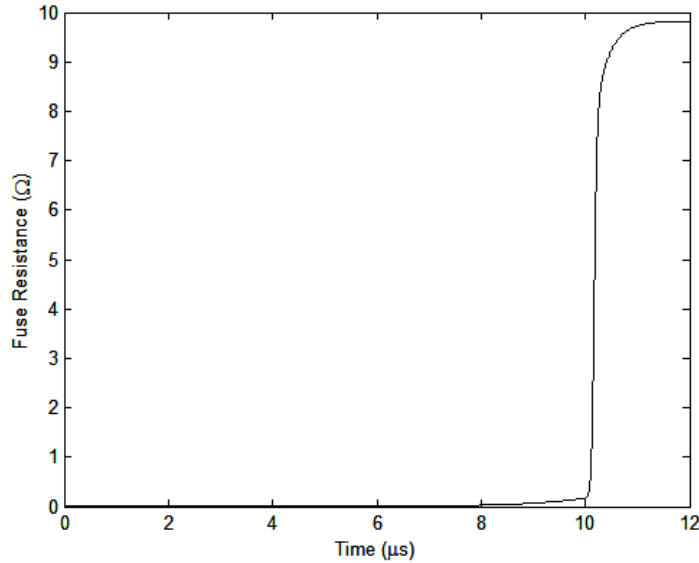


Figure 32. Fuse resistance without restrike

Figure 33 shows the fuse current corresponding to the numerical analysis of fuse resistance shown in Figure 32. The generator current rises to a peak of 40 kA with the form of equation (42). Upon the rapid rise in fuse resistance at $t = 10 \mu\text{s}$, the current falls to below 5 kA in 300 ns. Since there is no fuse restrike, the current is completely interrupted.

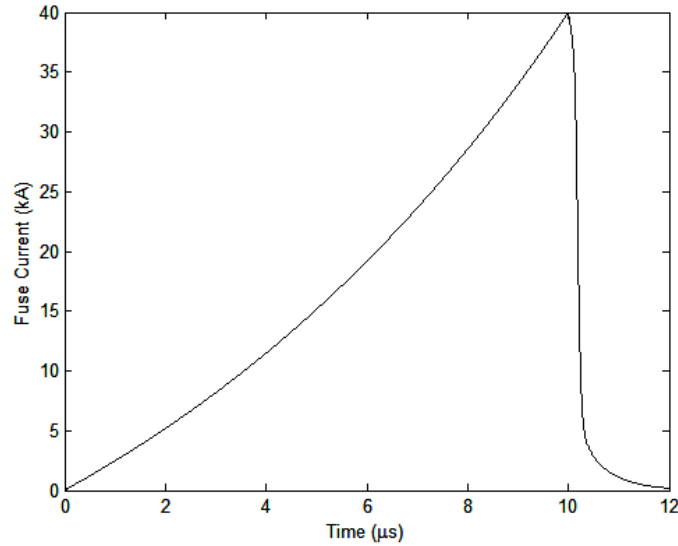


Figure 33. Fuse current without restrike

It is also beneficial to simulate the fuse and current waveforms when restrike occurs to recognize its effects on system performance. Figure 34 shows an example of the fuse resistance in the case that the specific action and specific energy limit beyond full vaporization is exceeded. The circuit of Figure 31 was simulated. The peak generator current was doubled to 80 kA, and the fuse area was increased to 0.3589 mm². However, the fuse length was kept at only 7 cm, so the specific action and specific energy exceeded the limit for restrike beyond full vaporization. After the action limit is reached at the end of generator operation, the fuse resistance begins to rapidly rise. However, the fuse restrike is clearly seen as the fuse resistance quickly falls from its peak value. The effect of the restrike can be seen on the primary current in Figure 35. After falling to below 25 kA within 300 ns of the end of generator operation, the current slightly rebounds to adjust to the low value of resistance after restrike and slowly decays.

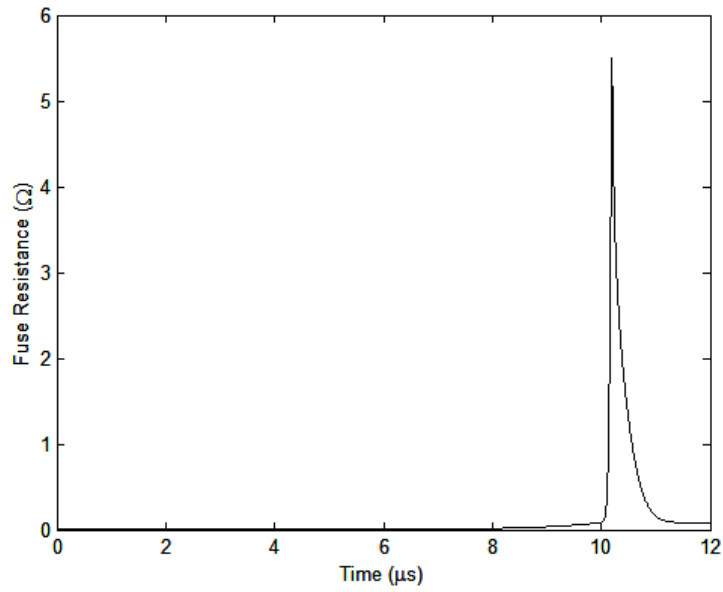


Figure 34. Fuse resistance with restrike

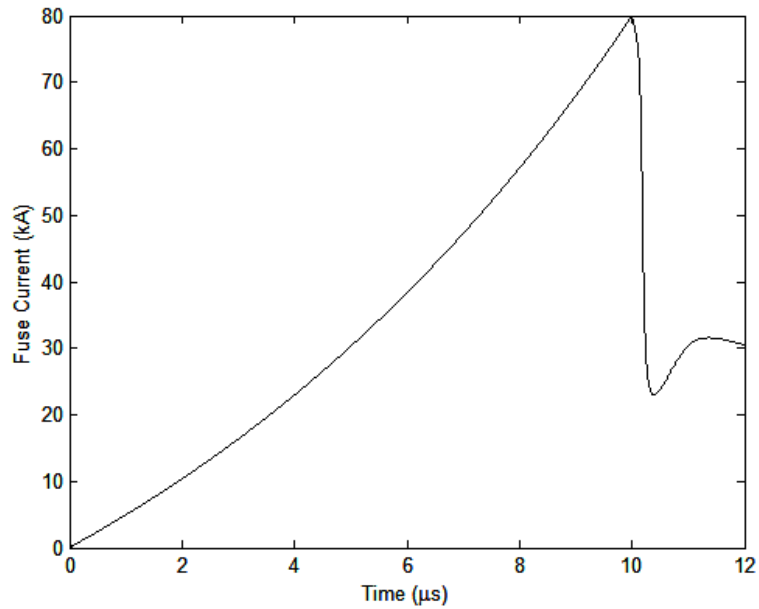


Figure 35. Fuse current with restrike

The preceding graphs show how numerical methods combined with analytically derived and curve-fit equations can be used to accurately simulate the power conditioning system with real fuse resistance response.

The effects of changes in fuse parameters can be modeled by the techniques used in this section. The resistance of a uniform resistor is given by equation (45).

$$R = \frac{\rho l_r}{A_r} \quad (45)$$

The resistance, R [Ω], is given as the product of the resistivity, ρ [$\Omega\cdot\text{m}$], and the length, l_r [m], divided by the area, A_r [m^2]. As will be discussed in the next section, the fuse area is determined based upon the action integral and cannot be significantly changed for a given current source. It is intuitive to believe from equation (45) that increasing the length of the fuse would increase the resistance. However, due to the unique resistivity dependence on specific action, described by equations (36) and (37), longer fuse lengths do not necessarily result in higher resistances.

The circuit of Figure 31 was again used to examine the differences in fuse behavior when all parameters were constant between simulations except the fuse resistance. The initial resistivity and the cross-sectional area of the fuses were the same for each simulation. Therefore, the different initial fuse resistances correspond to different fuse lengths between each simulation. The initial fuse resistance, R_0 [Ω], had values of 2.5 m Ω , 10 m Ω , 17.5 m Ω , and 25 m Ω to cover a range of possible initial values. The initial resistance of 2.5 m Ω corresponds to the shortest fuse, and the fuse lengths are increased proportionally to the initial fuse resistances. Figure 36 shows that for these values of initial fuse resistance, the higher final values of fuse resistance are obtained with the lower initial values. The exponential relationship between the fuse resistance and the action integral results in higher final resistance values for higher action integrals. The integral of current action is higher for lower initial fuse resistances. Therefore, the final resistance of shorter fuses surpasses the final resistance of longer fuses. The significance of determining which fuse parameters result in the highest final fuse resistance is that higher fuse resistances result in higher secondary voltages. The finding that shorter fuses

result in higher final resistances is contrary to what other fuse models predict and can be an important influence on fuse design. Furthermore, the results have also been confirmed in analyses of a system with a peaking switch, in which the load is isolated from the system up to the point of peak fuse voltage. The lower limit for the fuse length is determined by restrike conditions and will be discussed later in this chapter.

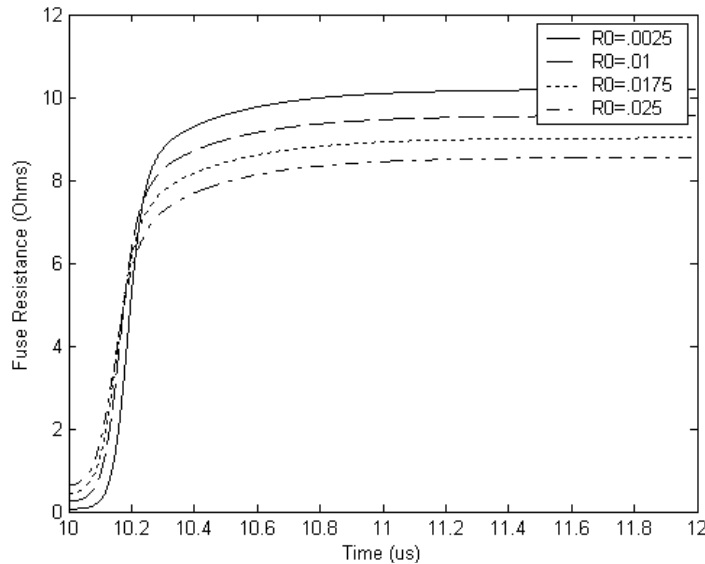


Figure 36. Fuse resistance after action limit for different initial fuse resistances

4.2.3 Fuse Energy Dissipation

Given the complicated relationships between the instantaneous primary current, i_p [A], the integral of current action, h [$A^2 \cdot s$], and the initial fuse resistance, R_0 [Ω], an analytical derivation is not possible to conveniently find the energy consumed by the fuse. Previous analyses have been made on the energy consumption of vaporizing fuses, assuming a linearly increasing fuse resistance and an isolated load up to the time of peak voltage across the fuse [11, 18]. With a numerical analysis, the energy consumed by the fuse and load can be determined with the actual fuse resistivity profile and specific system and fuse parameters. This allows greater insight into the energy dissipation in the fuse and the

overall efficiency of the system. Energy dissipation and efficiency values will vary based on the system and fuse parameters.

The circuit of Figure 31 was used for this analysis with the same parameters used for the simulation without restrike in the previous sub-section. Figure 37 shows an example energy distribution between the inductive store, fuse, and load. The energy is normalized to the total input energy of the source. Since the fuse resistance is non-zero during the FCG runtime, energy from the FCG will be dissipated in the fuse during generator operation. At the end of FCG operation, the fuse has dissipated 22.71% of the total energy input from the FCG, and the load has dissipated just 4.89%. The inductively-stored energy is 72.4% of the total energy input from the source. If a peaking switch had been in place, the energy dissipation by the fuse and the inductively-stored energy would be slightly increased, and the load energy dissipation would be zero.

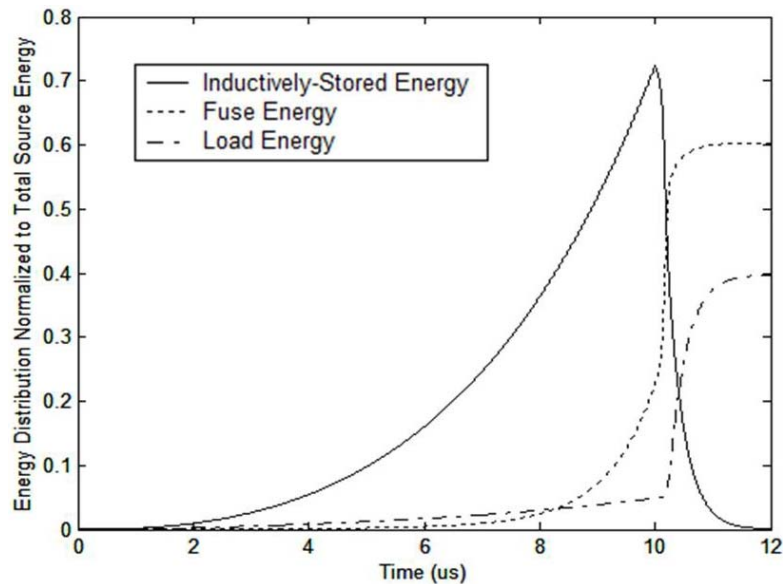


Figure 37. Energy distribution normalized to total source energy

It is shown by Reinovsky, Lindemuth, and Vorthman that for a system with a peaking switch, 63% of the energy inductively-stored at the end of generator operation will have

been dissipated in the fuse from the time the action limit is reached to the time at which the fuse voltage is at its peak [18]. It is also noted that this result is independent of the fuse or circuit parameters except that the fuse resistance rise is linear [18]. Heeren states that faster-than-linear resistance rises have a minimum energy dissipation of 63% of the inductively-stored energy at the time the action limit is reached [11]. These conclusions for the case of an open peaking switch to the point of peak voltage are correct. However, since the RF source considered in this investigation does not need to be isolated by a peaking switch, the energy dissipation without a peaking switch is desired.

Figure 38 is from the same simulation as shown in Figure 37, but the energy values are normalized to the inductively-stored energy at the end of generator operation. As Figure 38 shows, the energy dissipation by the fuse is much lower without a peaking switch. Just 51% of the energy inductively-stored at the time of the action limit is dissipated in the fuse. When considering the energy dissipated in the fuse as a percentage of the total energy supplied from the source, the values can be obtained from Figure 37. The percentage of total energy dissipated by the fuse is 60.31%, corresponding to a load energy dissipation efficiency of 39.69%. When the peaking switch is removed, the peak secondary voltage and the load energy efficiency both increase.

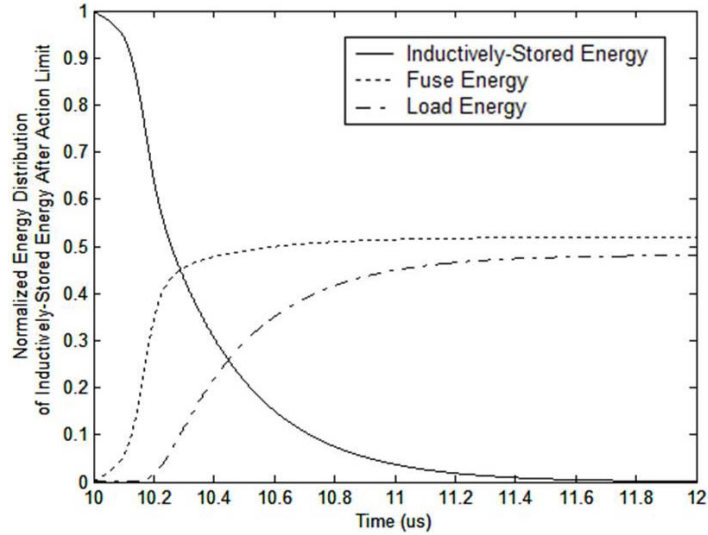


Figure 38. Energy distribution normalized to peak inductively-stored energy

The effects of the initial fuse resistance can also be seen in the energy dissipation in the fuse and load. This section has already demonstrated the benefits of higher final fuse resistance resulting from lower initial fuse resistances. Additionally, Figure 39 shows that lower values of initial fuse resistance increase the percentage of the initially inductively-stored energy dissipated in the load. Lower initial fuse resistances bring the total percentage of energy dissipated in the load closer to 50%, improving the system efficiency.

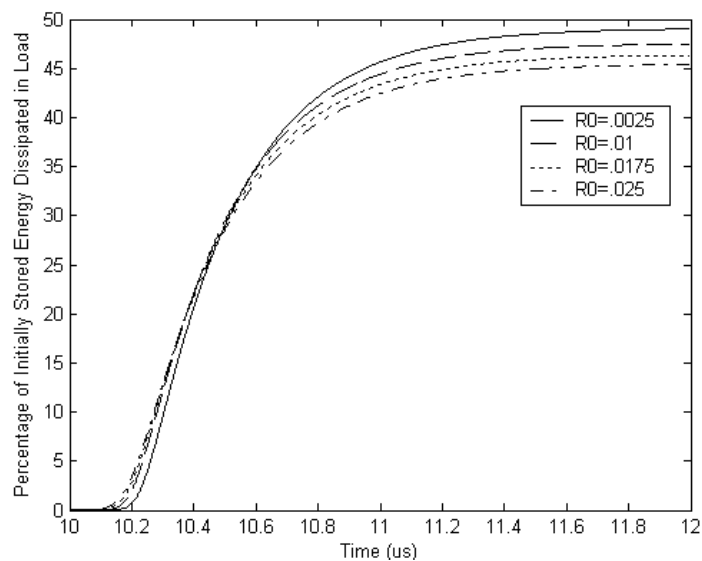


Figure 39. Percentage of initially stored energy dissipated in load

4.3 Exploding Wire Fuse Design

4.3.1 Fuse Cross-Sectional Area

Exploding wire fuses are designed to open the circuit after a predetermined integral of current action, h , as given by equation (35). The use of the integral of current action is derived by Maisonnier, Linhart, and Gourlan [15]. The method is summarized and required constants are provided by Heeren [11]. Since the use of the action integral has been well established and recorded in these works, a summary form is given here. The fuse parameter that is adjusted to vary the current action integral at which the fuse opens is the cross-sectional area. The number of fuse wires in the array can be easily varied to obtain the desired cross-sectional area and design for the opening point of the fuse. An equivalent action timescale, t_{eq} , is a method of normalizing the integral of current action to the current action at the time of fuse opening [18].

$$t_{eq} = \frac{\int_0^{t_0} I_p^2(t) dt}{I_p^2(t_0)} \quad (46)$$

Using the equivalent action timescale, the derivation for cross-sectional area results in equation (47) [11].

$$A_f = \alpha_l \sqrt{t_{eq}} I_{p0} \quad (47)$$

The cross-sectional area is represented by A_f [m^2]. A length proportionality constant, α_l [$\text{m}^2/(\text{A}\cdot\text{s}^{0.5})$], can be estimated for several wire materials. The fuse current at the time of the onset of interruption is represented by I_{p0} [A] [11]. The primary current, i_p , is equal to I_{p0} at the end of generator operation, t_0 . Ideally the fuse is designed to reach the predesigned action integral at the end of the FCG runtime, so t_0 is the same as t_r . To provide estimates based on FCG experimental data, calculated values of the integral of

current action from previous experiments were used to replace t_{eq} . Equation (46) can be rewritten as equation (48).

$$t_{eq} = \frac{h_e}{I_p^2(t_0)} \quad (48)$$

The equation for the wire cross-sectional area then simply becomes equation (49), where h_e is the integral of current action from zero to t_r .

$$A_f = \alpha_l \sqrt{h_e} \quad (49)$$

It should be noted that data associated with the design of the cross-sectional area, the resistivity of the wires, and the point of vaporization can be affected by the rate of energy dissipation in the fuse and, specifically, the current density [8, 10, 14]. Efforts were made to use data that was obtained with current densities on the same order as those used in this investigation. The constants presented by Heeren were obtained through the examination of similar systems, and the data from Tucker and Toth was obtained with current densities on the order of 10^7 A/cm² [10, 11].

4.3.2 Previous Standard for Fuse Length Design

The design of the optimal fuse length is less developed than the design guidelines for the fuse area. A basic equation governing the fundamentals of fuse length design for an inductive energy storage system with an exploding wire fuse is given by Reinovsky *et al.* [19]. The derivation is expanded and utilized further in other works [11, 18, 20]. However, each of those expansions contains errors that incorrectly design the optimal fuse length. Background on those designs is presented here to contrast them with the newly proposed design method.

The derivations of interest state that 63% of the inductively-stored energy is dissipated in the fuse between times at the beginning of wire vaporization and peak output voltage for the case in which the load is isolated until peak fuse voltage is reached [11, 18, 20]. Reinovsky *et al.* state that the fuse length can be designed such that the total energy dissipated by the fuse will bring the fuse mass to full vaporization [19]. The symbol l_f is the length [m], and the energy dissipated by the fuse is W_{fuse} [J]. The mass density is denoted by γ_m [kg/m³], and the fuse area is A_f [m²]. The fuse specific energy at vaporization is w_v [J/kg].

$$l_f = \frac{W_{fuse}}{\gamma_m A_f w_v} \quad (50)$$

Although there are more appropriate values to use for the specific energy than the vaporization specific energy, as will be discussed later, equation (50) is essentially correct. However, Reinovsky *et al.* do not state specifically how the energy dissipation, W_{fuse} , can be calculated [19]. The derivation is expanded by Reinovsky, Lindemuth, and Vorthman to state the energy dissipated in the fuse is 63% to 100% of the inductively-stored energy at the end of generator operation [18]. In equation (51), the symbol f is a percentage, between 0.63 and 1.0, of the inductively-stored energy at generator completion, W_{ISE0} [J], dissipated by the fuse. The specific energy at vaporization, w_v , was replaced by the burst energy density, w_b [J/kg].

$$l_f = \frac{f W_{ISE0}}{\gamma_m A_f w_b} \quad (51)$$

The same equation is derived by Heeren and Neuber with different, but equivalent, notation [11, 20]. Specifically, the specific energy term of equation (51), w_b , is replaced by w_{total} [J/kg] [11, 20]. The symbol w_{total} is defined as the specific energy required to

bring the fuse from the solid phase at its initial temperature to the vapor phase. These derivations are incorrect and lead to errors in the determination of the fuse length. The problem arises by defining the energy available to bring the fuse from its initial conditions to burst energy density or vaporization energy density in terms of the inductively-stored energy at the end of generator operation. Each of the references that derive equation (51) state the equivalent assumptions that either the fuse resistance is zero up to the action limit or all of the energy input from the source is inductively-stored [11, 18, 20]. The latter assumption can be represented by equation (52) in which W_{source} [J] is the total electromagnetic energy delivered by the FCG. The inductively-stored energy at the end of generator operation is represented as W_{ISE0} [J].

$$W_{source} = W_{ISE0} \quad (52)$$

As given by equation (38), the fuse resistance is non-zero during FCG operation. Energy is dissipated in the fuse during FCG operation, so the total specific energy dissipated in the fuse at the end of generator operation is non-zero. The corrected version of equation (52) is equation (53), in which $W_{fuse,t < tr}$ [J] is the energy dissipated in the fuse during generator operation.

$$W_{source} = W_{ISE0} + W_{fuse,t < tr} \quad (53)$$

If the load is not isolated from the source during source operation, then equation (53) is expanded to equation (54), which describes the situation examined in Figure 37.

$$W_{source} = W_{ISE0} + W_{fuse,t < tr} + W_{load,t < tr} \quad (54)$$

The energy dissipated in the fuse during FCG operation is a non-negligible portion of the total source energy. As in the example of the previous section shown in Figure 37, the fuse dissipated 22.71% of the source energy during source operation. The energy

dissipation of the fuse during FCG operation is non-negligible, and the assumption that all of the FCG output energy is inductively-stored is incorrect. The specific energy of the fuse at the end of generator operation corresponds to the beginning of vaporization and not the initial fuse conditions. Therefore, it is inappropriate to define the fuse length such that the fuse goes from its initial conditions to a fully vaporized state in terms of the inductively-stored energy at the end of source operation.

The observed errors in the previously-described derivations are described here because it appears to be the standard for fuse length design based on its use in other recent fuse studies, including the beginning of this investigation [21, 22]. During experiments at the beginning of this investigation, it became clear that the fuse lengths needed to be longer than the calculated values based on the previously-described designs. It was observed in another fuse study that the fuse lengths needed to be at least twice as long as those designed by the previous methods to prevent restrike [22]. It was also noted that fuse lengths were increased by Belt to prevent restrike from a design based on the previously-described methods [21].

4.3.3 Proposed Method for Fuse Length Design

It became clear that a new design method was required to correct the errors in the previous derivations and obtain an optimal fuse length. It was previously seen in numerical simulations that shorter fuse lengths resulted in higher peak voltages and improved energy efficiency. Experimental data reported by other investigators supports this observation. For long foil fuses, experimental measurements have been reported that show decreasing peak output voltage for increasing fuse lengths [23]. Another recent experimental investigation of exploding wire fuses observed that the highest peak voltage

occurred with the shortest fuse for which restriking did not occur [22]. An optimum fuse length can be estimated based upon experimental data relating the fuse resistivity to the specific energy dissipated in the fuse. As before, the derivation assumes that the electrical energy is dissipated in the fuse at short time scales such that significant thermal energy is not lost to the surrounding quenching media.

Experimental data has been produced by various researchers to produce continuous plots of fuse resistivity versus the specific action and the specific energy of many materials [10]. There are two points of particular interest in the graphs of fuse resistivity. First, the point of the action limit, as previously mentioned, corresponds to the beginning of fuse vaporization, and a dramatic increase in fuse resistivity follows this point. Second, a point occurs at which the fuse resistivity reaches a maximum and further energy dissipation in the fuse results in a decrease of the overall fuse resistance. For high energy systems, the specific energy corresponding to this maximum point can be surpassed and cause restriking. Knowledge of this point, however, can enable a designer to choose the length of the fuse such that the fuse resistance reaches the maximum without significant energy dissipation beyond this point. As the fuse modeling analysis shows, shorter fuses dissipate less energy while also reaching higher resistance values than longer fuses. Shorter fuses also result in increased energy dissipation in the load and higher load voltages. These results are all due to the increased fuse resistivity with increased specific energy. Shorter fuses have lower initial resistances than longer fuses with the same cross-sectional area and material parameters. However, these lower initial resistances result in less energy dissipation in the fuse during FCG operation, resulting in higher peak primary currents. Shorter fuses dissipate higher specific energies due to their

lower mass and the slightly higher peak primary current. These factors result in higher resistivity and overall fuse resistances that surpass those of longer fuses. The limit for decreasing the length of a fuse occurs when the specific energy dissipated in the fuse passes the point at which further increases in specific energy result in lower resistivity. This limit is the foundation for the design of the minimum fuse length.

From available experimental data, the specific energy can be found for the action limit and point of maximum fuse resistivity, denoted by w_{sp1} [J/kg] and w_{sp2} [J/kg], respectively. The heat of fusion in units of [J/kg] could alternatively be used for the difference between w_{sp2} and w_{sp1} to estimate the total energy involved in the metal vaporization. However, it is recommended here to use experimental values due to the observed differences between experimental values for the two points obtained in exploding wire experiments and the standard values for the heat of fusion [14]. By determining the length based upon the difference between the points of w_{sp1} and w_{sp2} , only the energy dissipated in the fuse after the action limit should be considered. In considering energy dissipation after the action limit is reached, the inductively-stored energy at the time of the action limit can now be appropriately used as the energy available to be dissipated in the fuse and load. To reiterate, the time of the action limit, if correctly designed, corresponds with the end of FCG operation, and the primary current is at its maximum. The peak inductively-stored energy, W_{ISE0} [J], can be calculated as the sum of inductively-stored energy in the leakage and magnetizing inductances, as shown in equation (57). The primary and secondary currents at the end of generator operation are represented as I_{p0} [A] and I_{s0} [A], respectively. If the primary current follows the form of equation (42), the secondary current at the end of generator operation can be calculated

by equation (55). The primary self-inductance is represented by L_p [H], and the coupling factor is given by k . The turn ratio is represented as n . The magnetizing current at the end of generator operation, I_{m0} [A], can be determined with equation (56). Equation (58) is a simplified form of equation (57) and can be used with predicted or measured values of the peak primary and secondary currents and the system parameters.

$$I_{s0} = \frac{I_{p0}k}{(e^1 - 1)n} \left[\frac{1}{\left(\frac{\varepsilon}{t_r} + \frac{R_L}{L_s}\right)} \left(\frac{\varepsilon}{t_r} e^\varepsilon + \frac{R_L}{L_s} e^{\frac{-R_L t_r}{L_s}} \right) - e^{\frac{-R_L t_r}{L_s}} \right] \quad (55)$$

$$I_{m0} = I_{p0} - nI_{s0} \quad (56)$$

$$W_{ISE0} = \frac{1}{2} L_p (1 - k) I_{p0}^2 + \frac{1}{2} L_p k I_{m0}^2 + \frac{1}{2} L_p n^2 (1 - k) I_{s0}^2 \quad (57)$$

$$W_{ISE0} = \frac{1}{2} L_p (I_{p0}^2 + n^2 I_{s0}^2 - 2kn I_{p0} I_{s0}) \quad (58)$$

When equation (58) is considered for a system with a peaking switch in place, there is no secondary current, and all of the energy is stored in the inductance of the primary winding.

$$W_{ISE0} = \frac{1}{2} L_p I_{p0}^2 \quad (59)$$

Based on simulation and experimental results, a fraction, f , of the inductively-stored energy will be dissipated in the fuse after the action limit. As was correctly derived for the situation in which a peaking switch is in place until the peak fuse voltage is reached, the minimum for this fraction is 0.63. As shown previously in this chapter for a case with no peaking switch, the fraction of inductively-stored energy dissipated in the fuse can be lower. The simulations with lower initial fuse resistances resulted in values of f that approached 0.5. Numerical simulations specific to the system parameters may be required to initially estimate f for a given system. By comparing the time of peak voltage in Figure

35 to the fraction of energy dissipated in the fuse in Figure 38, it is clear that the peak voltage occurs before the maximum fraction of stored energy has been deposited in the fuse. Therefore, it may be advantageous to slightly underestimate the fraction of energy dissipated in the fuse to allow the peak fuse resistance to be reached before the end of operation. Having the fuse resistance peak before the very end of system operation will allow the peak resistance to increase the peak of the load voltage pulse. Although the fuse resistance will decrease near the end of operation, the decrease will occur after the peak of the load voltage pulse, thus having little or no negative effect.

Since the fuse resistivity is in terms of the energy dissipated per unit mass, the mass of the fuse material, m_{fuse} [kg], is determined by the initial cross-sectional area, A_f [m²], as determined by the action limit, the fuse length, l_f [m], and the solid state mass density, γ_m [kg/m³].

$$m_{fuse} = \gamma_m A_f l_f \quad (60)$$

The specific energy change from the point of the action limit to the point of maximum fuse resistivity can be equated to the fraction of inductively-stored energy at the time of the action limit divided by the fuse mass.

$$w_{sp2} - w_{sp1} = \frac{f W_{ISE0}}{m_{fuse}} \quad (61)$$

Replacing the fuse mass by equation (60) allows the minimum length to be solved.

$$w_{sp2} - w_{sp1} = \frac{f W_{ISE0}}{\gamma_m A_f l_{min}} \quad (62)$$

$$l_{min} = \frac{f W_{ISE0}}{\gamma_m A_f (w_{sp2} - w_{sp1})} \quad (63)$$

Equation (63) is the basic equation that can be used for fuse length design. Given the equations relating the inductively-stored energy to the measured or calculated circuit currents, equation (63) can be expanded to equation (64) for the case with no peaking switch and equation (65) for the case of a peaking switch at least up to the action limit.

$$l_{min} = \frac{fL_p(I_{p0}^2 + n^2I_{s0}^2 - 2knI_{p0}I_{s0})}{2\gamma_m A_f (w_{sp2} - w_{sp1})} \quad (64)$$

$$l_{min} = \frac{fL_p I_{p0}^2}{2\gamma_m A_f (w_{sp2} - w_{sp1})} \quad (65)$$

With the fuse length and cross-sectional area determined, the fuse resistance can be predicted as a continuous function of specific action or specific energy. Alternatively, the fuse resistance can be calculated at the critical points of the beginning of system operation, the action limit, and end of system operation.

The previous derivation provides the optimum fuse length based on the principle of reaching the maximum fuse resistance. However, many high voltage systems may require the fuse length to be greater than this optimal minimum to prevent arc breakdown prior to full vaporization. Although one form of restrike is accounted for by ensuring that the specific energy dissipated in the fuse does not result in specific energy dissipation beyond full vaporization, the possibility of arc breakdown within or around the fuse before full vaporization is an issue that must be determined based upon the electric fields obtained with each system independently. The system parameters and the input energy to the system will determine the peak voltages that appear across the fuse. If the peak electric field across the field will result in breakdown in or around the fuse, the fuse length must be increased to lower the field to an acceptable level. The dielectric strength of fuses in one experimental study was estimated to be 6 kV/cm [23]. Another study reported

variations of the dielectric strength, depending upon the pressure of the tamping medium, up to about 20 kV/cm [24]. Although lengthening the fuse will result in a lower specific energy dissipated in the fuse and thus a lower fuse resistance, it can be imperative to prevent the more significant performance degradation associated with fuse restrike.

Table 8 gives the fuse parameters used for a simulation of the ideal minimum fuse length. The circuit used for the simulation is from Figure 31, and the other circuit parameters are the same as in Table 7. The fuse cross-sectional area was calculated given the predicted action limit, as given by equations (44) and (49). The length was then calculated using equation (64) with a value of f of 0.53. The value of f was based upon the percentage of energy dissipated observed in Figure 38. The peak secondary current was calculated with equation (55). The calculated fuse length was approximately 5.32 cm. This fuse length will result in the maximum fuse resistivity near the end of system operation, thus resulting in higher fuse resistance, load voltage, and energy dissipated in the load.

Table 8. Parameters for Simulation of Ideal Minimum Fuse Length

f	γ_m (kg/m ³) [25]	A_f (m ²)	w_{sp1} (J/kg) [10]	w_{sp2} (J/kg) [10]	l_{min} (m)
0.53	8960	1.79E-07	1409000	5909000	0.053162

The following graphs with the optimized fuse length can be compared to the graphs in Section 4.1, which were produced in simulations with identical parameters except for a fuse length of 10.45 cm. Figure 40 shows the specific energy dissipated in the fuse in time. The maximum specific energy is just over 5900 kJ/kg, corresponding to the point of maximum resistivity for copper according to Tucker and Toth [10].

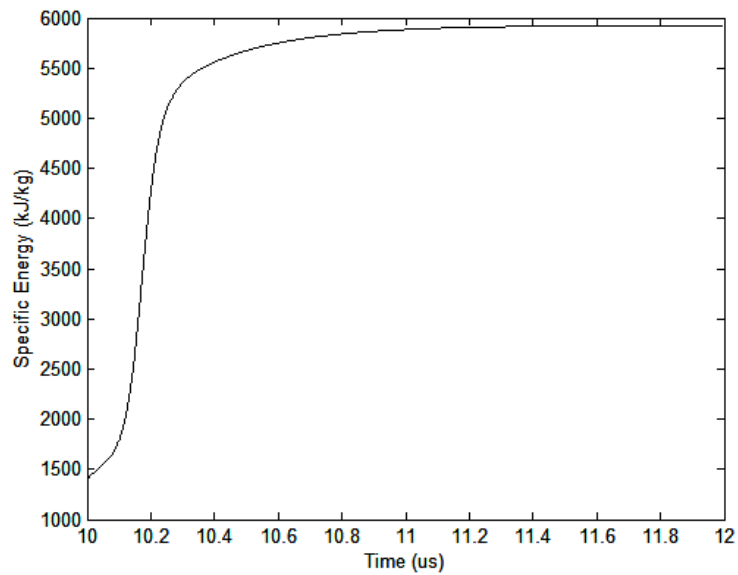


Figure 40. Specific energy dissipated in the fuse after the action limit

Figure 41 shows the fuse resistance after the action limit. Although the fuse is almost half the length as that simulated in Section 4.1, the fuse resistance is greater by approximately 0.5Ω , 5% greater than the peak value. This simulation verifies the new fuse length design as a method to maximize the fuse resistance. From the previously-established trends, maximizing the fuse resistance will also increase the load voltage and energy efficiency of the system. By shortening the fuse length, it is possible to increase the specific energy dissipated in the fuse such that the fuse resistance reaches a maximum near the end of system operation. However, many high voltage implementations of the power conditioning system considered in this thesis will require longer fuse lengths than the optimized minimum to prevent restrike. Longer fuses or advanced designs resistant to fuse breakdown due to high electric fields are often necessary.

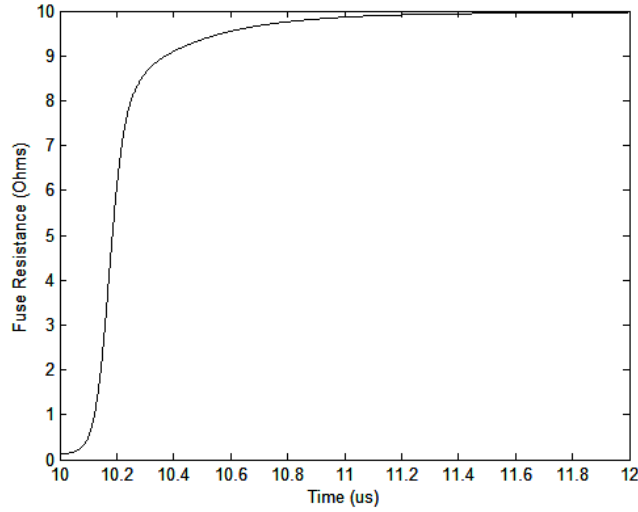


Figure 41. Fuse resistance after action limit for minimal length fuse

4.3.4 Fuse Inductance

Although the fuse resistance is the primary parameter of interest in fuse design, it is beneficial to be able to predict the inductance of the fuse as well. The geometry of the fuse, a circular array of parallel wires, closely resembles the geometry of wire arrays used for Z-pinch experiments. A coaxial structure is assumed for a wire array in a circular arrangement with radius r_0 [m] and a current return conductor of radius R_r [m]. The diameter of the individual wires is given as a_w [m]. The length of the wires is l_w [m], and N_w is the number of wires in the array. The inductance of the wire array can then be predicted from Kuai *et al.* as equation (66) [26].

$$L_{fuse} = \frac{\mu_0 l_w}{2\pi} \left(\frac{1}{N_w} \ln \left(\frac{R_r}{N_w a_w} \right) + \frac{N_w - 1}{N_w} \ln \left(\frac{R_r}{r_0} \right) \right) \quad (66)$$

Clearly, the inductance of the array is reduced as the number of wires is increased. The inductance can further be reduced by reducing the radius of the current return conductor, increasing the size of the wires, and bringing the radius of the wire array as close as possible to the radius of the current return. Table 9 provides an example calculation of the

fuse inductance for typical fuse dimensions, as detailed in the following section. The radius of the return current conductor is given as the maximum radius, given the system size constraints. The slow variance of the natural log term results in relatively small increases in the fuse inductance for larger radii of the current return path. Therefore, the inductance of the fuse in the experimental arrangement is on the same order as the calculated values. For the parameters given in Table 9, the inductance is calculated to be 167 nH. With the same fuse dimensions, varying the number of fuse wires from 10 to 40 changes the inductance over a range from 217 nH to 146 nH.

Table 9. Fuse Parameters for Inductance Calculation

R_r (m)	l_w (m)	N_w	a_w (m)	r_θ (m)	L_{fuse} (H)
0.0762	0.3	20	3.94E-05	3.81E-02	1.67E-07

4.4 Exploding Wire Fuse Construction

The exploding wire fuses consist of three main parts: the form on which the wires are wound, the housing in which the form and wires are packed in sand, and the fuse wires. The form has three equally spaced ratchet gears on which the wires are wound. The ratchet gears have an outer diameter of 7.62 cm with 100 teeth each. The teeth were ground down to flatten the sharp points of the teeth while still retaining the grooves to hold the wires in place. To further reduce corona around the teeth of the ratchet gears, field shapers were constructed in the plane of the ratchet gear. The field shapers consisted of 1.27 cm diameter copper pipe fittings soldered together into a semi-circular ring. Small copper pieces provided the physical and electrical connection of each ratchet gear to its corresponding field shaper. The ratchet gears and field shapers were equally spaced along a 30.48 cm long all thread rod with 2.54 cm of rod protruding on each end.

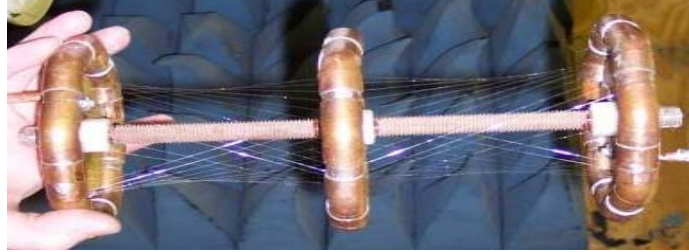


Figure 42. Central form of the fuse supporting angled fuse wires

The body of the fuse housing was an acrylic tube with a 15.2 cm diameter. The ends of the tubes were sealed by acrylic plates 15.24 cm square. Four all thread rods clamped the housing together through both plates. The quenching medium was very fine glass beads with a rated mesh size of 170-325. Holes were cut in the end plates to allow copper braid connections to be made with the circuit.

Forty gauge silver-plated copper wires with a 6.1% plating thickness were chosen based on previous fuse wire studies reported by Neuber [20]. Between 20 and 36 wires were used, depending on the desired action integral before opening. The wires were anchored to the all thread rod at each end of the fuse using an adhesive or double-sided tape to provide tension in each wire independent of the others.



Figure 43. Fuse housing being packed with fine glass beads

4.5 Crowbar Switch

4.5.1 Theory for Use of Crowbar Switch

The inductance of an FCG is a minimum at the end of its operation, at the peak current output. As previously discussed, the FCG simulator was also designed to have a minimal inductance at the time of peak current. However, experiments proved that the inductance of the FCG simulator at the time of fuse opening was non-negligible. As a result, there was a very significant additional voltage across the fuse as the current was interrupted. The increased electric field can cause fuse restrike, decreasing the rate of the primary current interruption. It is also possible for a restrike event to occur due to excessive energy dissipation beyond full vaporization as a result of stray inductance. The stray inductance in series with the fuse can result in a larger fraction of the inductively-stored energy being dissipated in the fuse. Since a restrike event reduces the load voltage, it was determined that a crowbar switch should be implemented to divert the energy stored in the stray inductance to help prevent restrike. With the crowbar switch in place, the voltage across the fuse at the time of the fuse opening should approximately equal the voltage across the transformer primary winding, and the fraction of energy dissipated in the fuse should be approximately that expected with no stray inductance. After the development and implementation of a crowbar switch in this investigation, research in the literature uncovered an early incidence of a type of crowbar switch that had been used with exploding wires to reduce the energy deposition in wires used for compound synthesis [27].

The exploding wire fuse resistance rises to a finite value upon the vaporization of the wire array. Examining the primary circuit during this resistive increase, as shown by

Figure 44, it is seen that the voltage across the fuse resistance, V_{fuse} [V], is equal to the voltage across both the transformer primary inductance, V_{pri} [V], and the voltage across the stray inductance of the circuit, V_{LS} [V].

$$V_{fuse} = V_{pri} + V_{LS} \quad (67)$$

For the case in which stray inductance is non-negligible, the voltage across the stray inductance during current interruption can be very high, and the system performance can be seriously degraded. The power and energy delivered to the load can be decreased as a result of stray inductance, particularly if the stray inductance results in restriking.

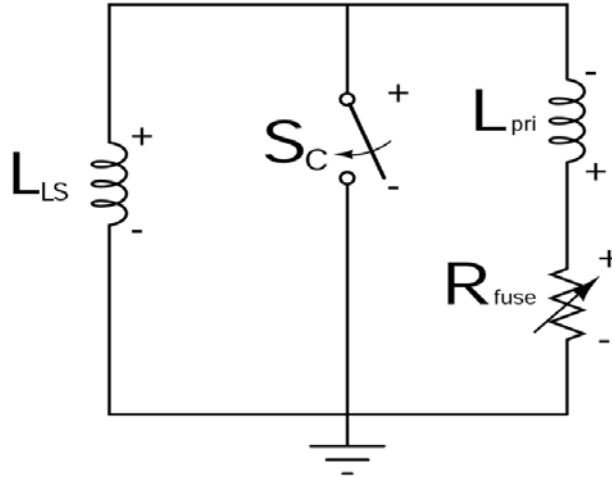


Figure 44. Primary circuit with non-negligible stray inductance and crowbar switch

Analyses of restriking due to excessive electric fields and excessive energy dissipation in the fuse due to stray inductance are provided in this section. The circuit of Figure 31 is used for the analyses. Many of the conclusions from the analysis and the effects of degraded system performance can be extended to a system with an RF source on the secondary. The stray inductance in the primary circuit is in series with the primary leakage inductance. The circuit analysis can thus be performed when the primary leakage inductance is replaced by the primary leakage inductance plus the stray inductance as in the relation given by equation (68).

$$L_{lp} \rightarrow L_{lp}(1 + x) \quad (68)$$

The value of x can be increased to increase the value of stray inductance in consideration. The stray inductance is calculated in terms of a primary leakage inductance, $L_p(1-k)$, of 200 nH, corresponding to a 1 μ H primary inductance with a coupling factor of 0.8. The stray inductance values range from relatively low inductances that may be present in many large circuits to inductances of a few microhenries, which could be present if the fuse action limit is reached before the end of FCG operation.

There are two methods used to examine the effects of multiple stray inductance values on fuse and system performance. The first is to vary the primary stray inductance while the peak inductively-stored energy and the fuse parameters are the same. This analysis allows the effects of stray inductance on fuse performance to be examined without varying the amount of energy available to dissipate in the fuse. This situation could occur in real systems. If the total output energy of a generator is approximately constant for a range of inductive loads, the generator will provide the peak currents listed in Table 10. For a higher primary stray inductance, the peak current values must be decreased to ensure equal energy storage between the cases. The fuse parameters from Table 7 were used. For comparison with the case of zero stray inductance, as analyzed in Section 4.3, the assumed initial energy for each case is equal to the energy used in that section, 725.8 J. Table 10 provides a summary of circuit values for each case.

Table 10. Parameters Used for Stray Inductance Analysis with Equal Energy Storage

Stray Inductance (μH)	I_{p0} (A)	I_{s0} (A)	I_{m0} (A)	Energy Stored (J)
0.0	40000	803.54	37589	725.8
0.2	36208	727.37	34026	725.8
1.0	27588	554.20	25925	725.8
2.0	22345	448.88	20998	725.8
4.0	17199	345.50	16162	725.8

Figure 45 displays the current fall for multiple values of stray inductance. The initial currents are different, corresponding to the magnitude that gives each system an equal amount of inductively-stored energy. The cases with higher stray inductance show less current interruption by the fuse. This is a sign of restriking occurring in the fuse, with more dramatic effects as the stray inductance increases. The fuse restrike seen here is a result of excessive energy dissipation in the fuse beyond full vaporization. The fuse restrike can be seen directly in the plot of fuse resistance in Figure 46. For high values of stray inductance, the fuse resistance is reduced significantly, reducing the effectiveness of the fuse in interruption of the primary current.

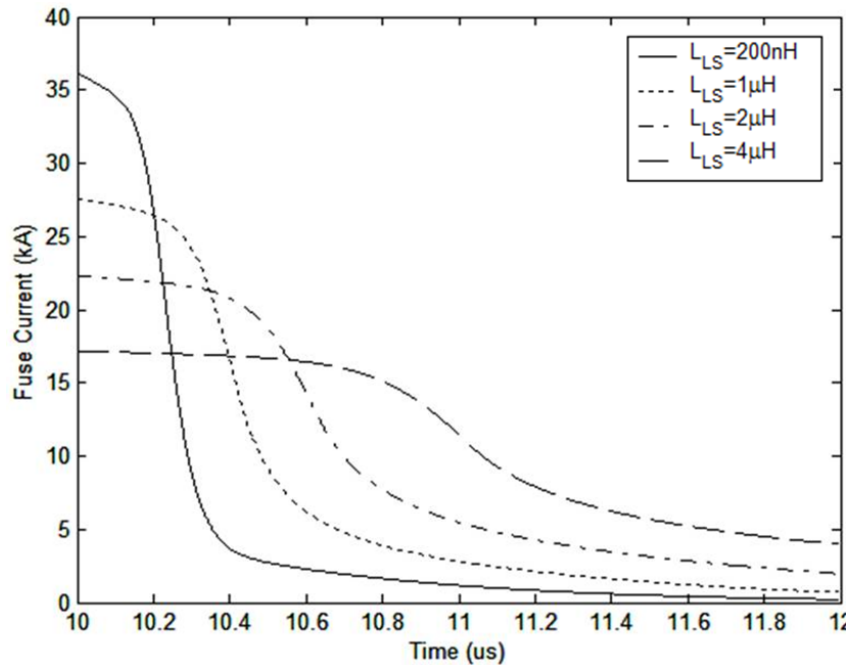


Figure 45. Primary current for multiple primary stray inductance values

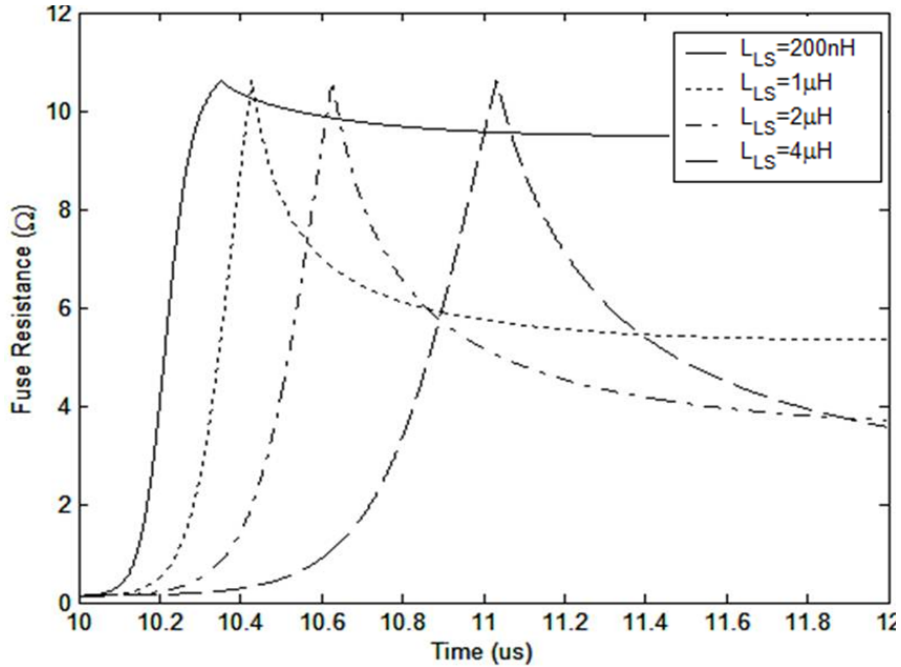


Figure 46. Fuse resistance for multiple primary stray inductance values

The cause of the resistance collapse in this case can be seen in Figure 47. Although the same fuse and the same amount of total energy were used in the analysis, the specific energy dissipated in the fuse is much higher for cases with higher stray inductance. For a stray inductance of 200 nH, the specific energy dissipated in the fuse is only slightly greater than the 5.909 kJ/g point for maximum resistivity. However, the other cases all resulted in much higher specific energies and corresponding drops in fuse resistance. This increase in specific energy dissipated in the fuse also results in lower energies delivered to the load for higher stray inductances. Even if the effects of fuse restrike are minimal, the system performance is degraded by lower efficiency as the fuse consumes a larger percentage of the inductively-stored energy. Table 11 lists the percentage of the total energy dissipated in the fuse.

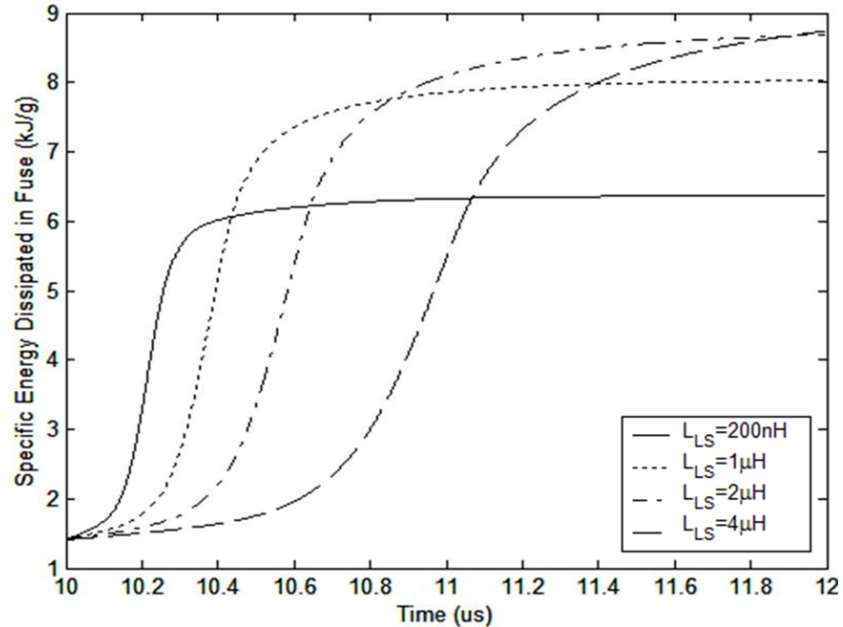


Figure 47. Specific energy dissipated in the fuse after current source operation

Table 11. Percentage of Inductively-Stored Energy Dissipated in Fuse After Action Limit

Stray Inductance (μH)	Percentage
0	51.66
0.2	60.58
1.0	80.85
2.0	88.94
4.0	89.57

The increased percentage of energy dissipation in the fuse for higher stray inductance can be visualized with the aid of Figure 48. The circuit shows the system after FCG operation. The circuits represent the T-equivalent of the transformer with ideal coupling for simplicity. Circuit (a) has a non-negligible stray inductance, and circuit (b) has zero stray inductance. When the fuse resistance increases, the current in the stray inductance of circuit (a) must go through the fuse resistance regardless of the resistance rise of the fuse. Based upon the relative impedances of the current path with the fuse resistance and stray inductance and the path with the load resistance, the current in the magnetizing inductance of circuit (a) will be shared between the two. In circuit (b), however, there is

no inductance in series with the fuse. Since there is ideally no inductance in series with the fuse in this case, there is no minimum current that must flow through the fuse. Only a fraction of the current in the magnetizing inductance will pass through the fuse resistance based upon its relative impedance with the load resistance. Thus, for cases with higher stray inductances, higher amounts of energy are stored in the stray inductance rather than the magnetizing inductance, and the fuse will dissipate higher amounts of energy.

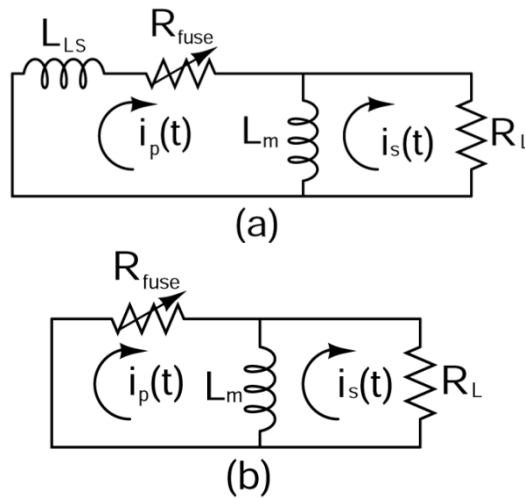


Figure 48. Simplified schematics with and without stray inductance

The second method of analyzing the effects of stray inductance is to consider a situation in which the peak currents and fuse parameters are the same for several values of stray inductance. This situation could also occur in a real system. An FCG or FCG simulator is often tested into a known inductive load, such as a transformer or inductor, to test its output characteristics. The known inductive load and the measured currents would be used to design the fuse for implementation in future experiments. However, if there is stray inductance that is unaccounted for, there will be excess system energy and an increased possibility of fuse restrike. This situation could occur when there is unknown circuit inductance in an FCG simulator or a non-negligible inductance of the FCG at the time the action limit of the fuse is reached. The peak current value of 40 kA is the same

as the case of no stray inductance in the previous analysis. Table 12 lists the stray inductance, current, and energy parameters for this analysis. The fuse parameters were chosen such that the fuse area corresponds to an action limit of $4107.5 \text{ A}^2\text{s}$. This again is the same value as for the case of no stray inductance in the previous analysis. The fuse length, however, is increased significantly over the minimum value. The fuse length is approximately the length of the fuses used in the experimental parts of this investigation. Use of this length makes the fuse more robust against restrike and provides a reference for comparison of theoretical effects of stray inductance to the experimentally observed effects. The fuse parameters are listed in Table 13.

Table 12. Parameters for Analysis with Equal Peak Currents and Identical Fuse

Stray Inductance (μH)	I_{p0} (A)	I_{s0} (A)	I_{m0} (A)	Energy Stored (J)
0.0	40000	803.54	37589	725.8
0.2	40000	803.54	37589	885.8
1.0	40000	803.54	37589	1525.8
2.0	40000	803.54	37589	2325.8

Table 13. Fuse Parameters for Analysis with Equal Peak Currents and Identical Fuses

Fuse Length (m)	Fuse Area (m^2)	Fuse Mass (g)	R_0 (Ω)
0.280	1.79E-07	0.437	0.0269

Since the fuse length was increased above the minimum value, the fuse mass was increased to the point where restrike from excessive specific energy dissipated in the fuse is not an issue. In this analysis, restrike due to excessive electric fields is investigated. To determine the peak fuse voltage and electric field achievable given the system parameters, the numerical model does not assume a value for the dielectric strength of the fuse. The effects of stray inductance on the peak electric field can thus be determined.

Table 14 demonstrates again how having a larger percentage of the total energy stored in the stray inductance results in a higher percentage of energy dissipated in the fuse. This

extra energy dissipation in the fuse is an effect of having more system energy for larger stray inductances and a larger stored energy in series with the fuse, as previously described.

Table 14. Percentage of Inductively-Stored Energy Dissipated in Fuse After Action Limit

Stray Inductance (μH)	Percentage
0	54.74
0.2	60.67
1.0	75.31
2.0	83.41

The fuse voltage, shown in Figure 49, reveals the ultimate result of the extra stray inductance. The fuse voltage dramatically increases from less than 100 kV for the case of no stray inductance to several hundred kilovolts for up to 2 μH of stray inductance.

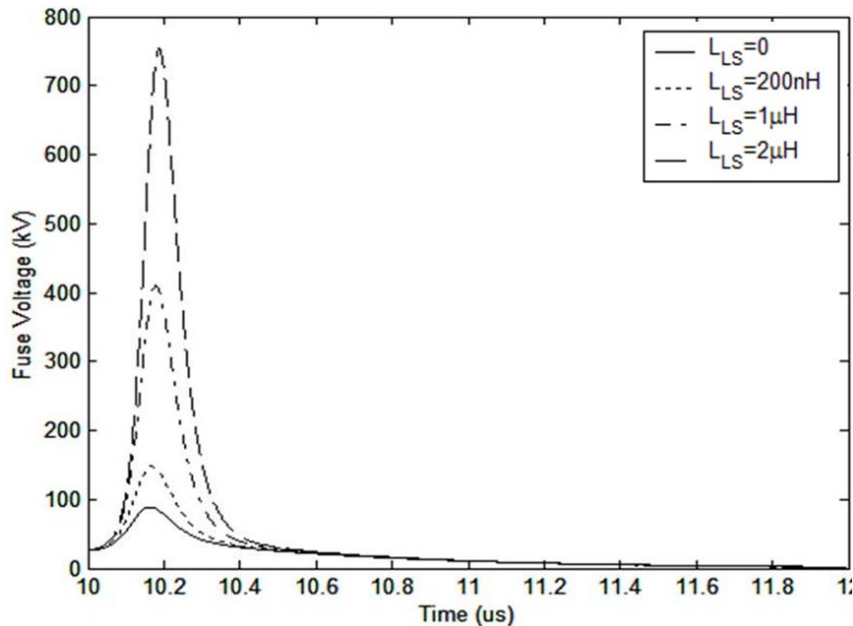


Figure 49. Fuse voltage after action limit for multiple primary stray inductance values

Dividing the fuse voltage by the fuse length gives the fuse electric field, as shown in Figure 50. The estimated breakdown strength of vaporized wire was estimated by one study as 6 kV/cm [23]. This would result in stable operation without fuse restrike for the case with no stray inductance and with 200 nH of stray inductance. Stray inductances

slightly above 200 nH would produce field levels above 6 kV/cm in this simulation, and the field levels corresponding to 1 μH and 2 μH would very likely result in an arc breakdown restriking event. This analysis verifies that for a fuse designed for a specific inductance and peak current, extra stray inductance can cause a catastrophic restriking event.

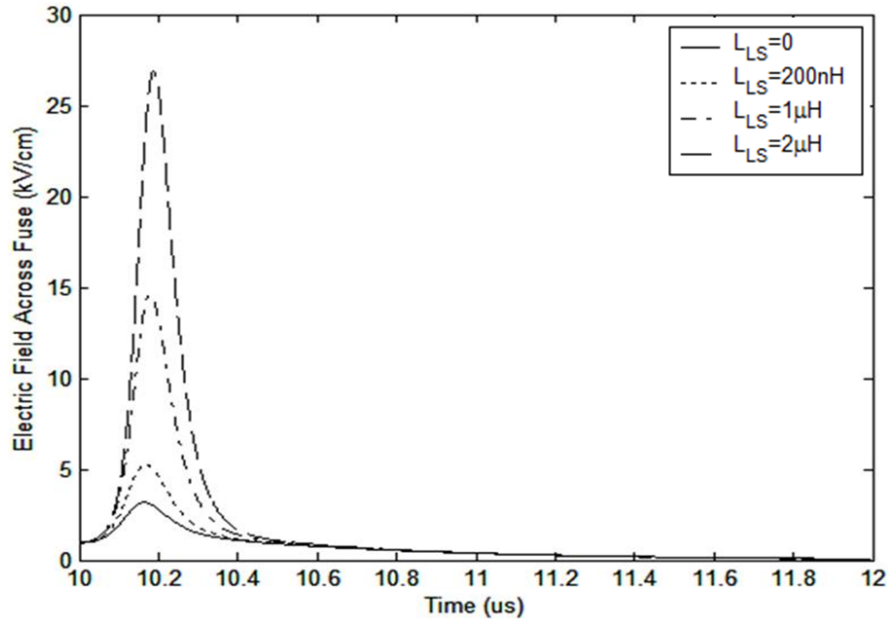


Figure 50. Electric field across fuse after action limit

As a part of circuit optimization, the stray inductance should be made a minimum. However, unavoidable sources of stray inductance and the possibility of significant stray inductance due to variations in FCG operation make the use of a crowbar switch very beneficial. The implementation of a crowbar switch can significantly help in avoiding the negative effects of stray inductance by preventing restriking of the fuse. In the case in which a fuse is designed to operate near its optimal minimum length, excess stray inductance can cause restriking from an excessive amount of energy dissipation in the fuse. This situation corresponds to the first analysis. In this situation, the crowbar switch diverts the excess energy stored in the stray inductance, greatly reducing the excess

energy dissipated in the fuse and preventing restrike. In the case in which the fuse length is much longer than the optimal minimum value, excess energy dissipation is less of a concern. However, excess stray inductance can still result in electric field levels in the fuse that will cause restrike due to breakdown. Implementation of a crowbar switch in this circumstance allows the excess energy in the stray inductance to be diverted and the field levels across the fuse to be significantly lowered by shorting the stray inductance. With the crowbar switch in place, only the voltage across the inductive store appears across the fuse. The crowbar switch is a simple yet critical element in the power conditioning system to limit the effects of stray inductance.

4.5.2 Crowbar Switch Implementation

One crowbar switch was constructed as a proof of principle of its ability to decrease restrike events. The crowbar switch was implemented as a simple atmospheric pressure air spark gap. Connections across the switch were made to two aluminum plates. The plates and electrodes were held together with dielectric all thread rods. The spacing of the switch was adjusted between 1 cm and 2 cm to ensure that the spark gap could hold off at least 30 kV and not close before the fuse action limit. The spacing could easily be adjusted by moving the aluminum plates along the all thread rods. The electrodes were stainless steel acorn nuts bolted to the aluminum plates. The acorn nuts are approximately hemispherical and provide a switching surface without significant field enhancements. Due to the amount of energy being diverted through the crowbar switch, significant erosion of the electrodes occurred, requiring replacement of the electrodes every few shots.

References for Chapter 4

- [1] K. H. Schoenbach, "Opening switches," in *Pulsed Power Lecture Series*. vol. No. 34: Texas Tech University.
- [2] K. H. Schoenbach, M. Kristiansen, and G. Schaefer, "A review of opening switch technology for inductive energy storage," *Proc. of the IEEE*, vol. 72, pp. 1019-1040, 1984.
- [3] E. Aivailotis and M. Peterhans, "Explosive opening switch work at Westinghouse," *IEEE Trans. on Magnetics*, vol. 35, pp. 40-45, 1989.
- [4] G. S. Janes and H. E. Koritz, "High power pulse steepening by means of exploding wires," in *Exploding Wires*. vol. I, W. G. Chace and H. K. Moore, Eds. New York, NY: Plenum Press, 1959.
- [5] W. G. Chace and H. K. Moore, "Exploding Wires." vol. I, II, III, IV New York, NY: Plenum Press.
- [6] W. G. Chace and M. A. Levine, "Classification of Wire Explosions," *Journal of Applied Physics*, vol. 31, p. 1298, 1960.
- [7] S. I. Tkachenko, V. S. Vorob'ev, and S. P. Malyshenko, "Parameters of wires during electric explosion," *Applied Physics Letters*, vol. 82, pp. 4047-4049, June 9, 2003 2003.
- [8] V. S. Sedoi, G. A. Mesyats, V. I. Oreshkin, V. V. Valevich, and L. I. Chemezova, "The current density and the specific energy input in fast electrical explosion," *IEEE Trans. Plasma Science*, vol. 27, pp. 845-850, 1999.
- [9] G. W. Anderson and F. W. Neilson, "Use of the "action integral" in exploding wire studies," in *Exploding Wires*. vol. I, W. G. Chace and H. K. Moore, Eds. New York, NY: Plenum Press, 1959.
- [10] T. J. Tucker and R. P. Toth, "A computer code for the prediction of the behavior of electrical circuits containing exploding wire elements," Sandia National Laboratories, Albuquerque, NM SAND-75-0041, 1975.
- [11] T. Heeren, "Power conditioning for high voltage pulse applications," Ph.D. Dissertation, Elec. and Comp. Engr., Texas Tech University, Lubbock, TX, 2003.
- [12] E. C. Snare and F. W. Neilson, "Large exploding wires - correlation to small wires and pause time versus length dependency," in *Exploding Wires*. vol. I, W. G. Chace and H. K. Moore, Eds. New York, NY: Plenum Press, 1959.
- [13] I. R. Lindemuth, J. H. Brownell, A. E. Greene, G. H. Nickel, T. A. Oliphant, and D. L. Weiss, "A computational model of exploding metallic fuses for multimegajoule switching," *Journal of Applied Physics*, vol. 57, p. 13, 1985.
- [14] T. J. Tucker, "Behavior of exploding gold wires," *Journal of Applied Physics*, vol. 32, pp. 1894-1900, 1961.
- [15] C. Maisonnier, J. G. Linhart, and C. Gourlan, "Rapid transfer of magnetic energy by means of exploding foils," *The Review of Scientific Instruments*, vol. 37, pp. 1380-1384, 1966.
- [16] E. David, *Z. Physik*, vol. 150, 1958.
- [17] "MATLAB," 6.5.0.1924 Release 13 ed Natick, MA: The MathWorks, 2002.
- [18] R. E. Reinovsky, I. R. Lindemuth, and J. E. Vorthman, "High voltage power condition systems powered by flux compression generators," in *Proc. 7th Pulsed Power Conference*, R. White and B. Bernstein, Eds. Monterey, CA, 1989.

- [19] R. E. Reinovsky, D. L. Smith, W. L. Baker, J. H. Degnan, R. P. Henderson, R. J. Kohn, and N. F. Roderick, "Inductive store pulse compression system for driving high speed plasma implosions," *IEEE Trans. Plasma Science*, vol. PS-10, pp. 73-81, 1982.
- [20] A. A. Neuber, "Explosively Driven Pulsed Power," Berlin: Springer-Verlag, 2005.
- [21] D. Belt, "Non-explosive test bed for flux compression generator fuses," M.S. Thesis, Elec. and Comp. Engr., Texas Tech University, Lubbock, TX, 2006.
- [22] D. R. McCauley, "Electro-explosive fuse optimization for FCG current sources," M.S. Thesis, Elec. and Comp. Engr., Texas Tech University, Lubbock, TX, 2007.
- [23] J. N. DiMarco and L. C. Burkhardt, "Characteristics of a magnetic energy storage system using exploding foils," *Journal of Applied Physics*, vol. 41, pp. 3894-2899, 1970.
- [24] I. M. Vitkovitsky and V. E. Scherrer, "Recovery characteristic of exploding wire fuses in air and vacuum," *Journal of Applied Physics*, vol. 52, pp. 3012-3015, 1981.
- [25] D. R. Lide, "CRC Handbook of Chemistry and Physics," 88th (Internet Version 2008) ed Boca Raton, FL: CRC Press/Taylor and Francis, 2008.
- [26] B. Kuai, A. Qiu, L. Wang, Z. Zeng, W. Wang, P. Cong, T. Gai, F. Wei, N. Guo, and Z. Zhang, "Primarily Experimental Results for a W Wire Array Z Pinch," *Plasma Science and Technology*, vol. 8, pp. 168-171, 2006.
- [27] M. J. Joncich, S. K. Lott, C. W. Spangler, and H. B. Giddings, "Apparatus with electronic crowbar for chemical investigations of exploding wire phenomena," in *Exploding Wires*. vol. IV, W. G. Chace and H. K. Moore, Eds. New York, NY: Plenum Press, 1968.

Chapter 5: High Voltage RF Source

The high voltage RF source performs two primary functions in the system operation. First, the capacitor stores the energy transferred from the primary circuit at high voltage. Second, the capacitor discharges through a low inductance shunt to form a high frequency oscillating circuit. Since the capacitor is both the high voltage energy storage component and part of the resonant circuit, it is the most crucial component in the RF load. Additionally, the spark gap switch and inductive shunt determine the frequencies of oscillation across the load, and the design of these inductive components must be considered to ensure resonance in the desired frequency range.

The energy dissipating element in the system is placed in parallel with the resonant LC circuit. The load could be an antenna for simulating RF signals. Alternatively, the load can be a resistive approximation of the antenna impedance. For design purposes, the load impedance was assumed to be the impedance of free space, approximately 377Ω . The following three sections describe the three high voltage capacitors used in this investigation, the aqueous-electrolyte resistor used a dummy load in place of an antenna, and the low inductance switch.

5.1 High Voltage Capacitor

As previously mentioned, the high voltage capacitor served as both the high voltage energy storage element and the capacitive element of the high frequency oscillator. Therefore, the design of the capacitor must be optimized with considerations for both energy storage and the resonant frequency. The energy stored, W_C [J], in a capacitive

element is directly proportional to the capacitance, C_S [F], as shown in equation (69) [1]. The symbol V_C [V] is the capacitor voltage.

$$W_C = \frac{1}{2} C_S V_C^2 \quad (69)$$

The system energy is sufficient to charge capacitors on the order of 100s of picofarads to around 1 MV. Since the compact capacitors in this study were designed for peak voltages on the order of a few hundred kilovolts, the capacitance could be increased to the order of nanofarads. For maximum energy storage and maximum RF energy delivered to the antenna or dummy load, the capacitance should be made as high as possible. However, the capacitance is limited to form a resonant circuit that oscillates in the range of several 10s of MHz. For the parallel RLC network of the RF source, the resonant frequency, ω [rad/s], can be determined by equation (70) [2]. The shunt inductance is given as L_{shunt} [H], and the impedance of the antenna is represented as Z_L [Ω]. The load impedance is considered to be completely real in equation (70).

$$\omega = \sqrt{\frac{1}{L_{shunt} C_S} - \frac{1}{4Z_L^2 C_S^2}} \quad (70)$$

With the capacitive term in the denominator of both fractions in equation (70), it is clear that increased capacitance results in a lower resonant frequency. The capacitance cannot be maximized for energy storage without reducing the resonant frequency. Figure 51 shows the dependence of the resonant frequency and the energy storage on the capacitance. For calculations of the resonant frequency dependence, the shunt inductance was assumed to be 30 nH, which is a representative value for a real shunt. The load impedance was assumed to be 377 Ω to represent the impedance of free space. For calculations of the energy storage dependence, the charging voltage was assumed to be

200 kV. The energy stored increases linearly with capacitance, but the resonant frequency decreases approximately as $C_S^{-1/2}$.

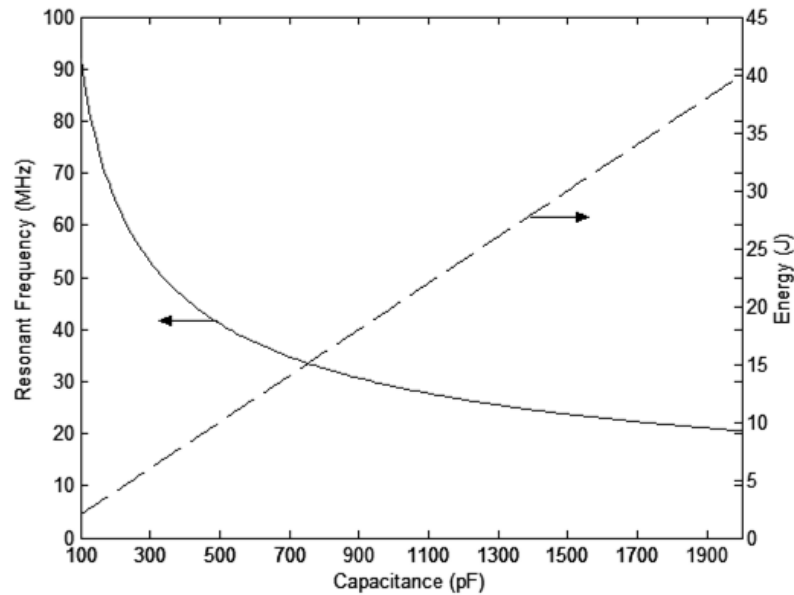


Figure 51. Dependence of resonant frequency and energy storage on capacitance

With the tradeoff between energy storage and resonant frequency established, the design constraints for the high voltage capacitor are determined. The minimum desired resonant frequency can be used to set the upper limit on the capacitance. For an assumed value of 30 nH shunt inductance, the maximum capacitance is limited to approximately 900 pF for a resonant frequency above 30 MHz. The minimum capacitance can be determined by the lower limit of energy stored in the capacitor and delivered to the load. If the minimum desired energy storage of the capacitor is 5 J, the minimum capacitance corresponding to a 200 kV charging voltage is 250 pF. As previously mentioned, the power conditioning system is capable of charging a capacitance on the order of 100s of picofarads to voltages up to around 1 MV. Therefore, the peak charging voltage is primarily limited by the size constraints on the system components and the dielectric strength of the insulating materials. For the highest power output and the maximum

energy delivery to the load, the maximum charging voltage attainable in consideration of these limitations is desired. Table 15 summarizes the energy storage and resonant frequency ranges obtained for the minimum and maximum capacitance values. The values are obtained assuming a 200 kV charge voltage, 377 Ω load impedance, and 30 nH shunt inductance. It should be noted that although the resonant frequency of an RLC circuit can be determined using equation (70), other factors, including multiple modes and transmission line effects, can alter the observed frequency spectrum.

Table 15. Energy Stored and Resonant Frequency at Min. and Max. Capacitance

	Energy Stored (J)	Resonant Frequency (MHz)
Minimum Capacitance (pF) 250	5	58.1
Maximum Capacitance (pF) 900	18	30.63

The high voltage capacitor imposes design constraints of high peak voltage, low capacitance and inductance for high frequency operation, and a compact cylindrical geometry. There are many commercially-produced capacitors for the pulsed power, RF, and electric power industries that fit some of the requirements for this system [3-9]. However, the combined requirements of the capacitor required in the power conditioning system disqualify nearly all commercially-produced capacitors. Capacitors for many RF and pulsed power systems have capacitance values in the desired range but operate at much lower voltages [3, 8]. Many capacitors designed for very high voltages are implemented for energy storage, so the capacitance is too high for operation in the frequency range of interest [5-7, 9]. Most of these commercial products also exceed the acceptable dimensions for the power conditioning system. Capacitors designed for high voltage transmission systems have both very high voltage capabilities, capacitances in the

range of interest, and a cylindrical design [3]. However, the dimensions also exceed the system limitations. Additionally, the capacitors for transmission systems are designed to operate at very low mains frequencies, and the RF characteristics of these capacitors are unknown. The design constraints of the high voltage capacitor limit the application of a commercially-available product, so the development of a suitable device was required as a part of this investigation.

One of the critical elements in capacitor development is the dielectric material. The many types of previously-developed capacitors are often characterized by the dielectric materials utilized [10]. The diversity of dielectrics implemented in capacitors include gases, vacuum, plastics, papers, oils, glasses, mica, porcelain, oxides, and ceramics, among more [1, 10, 11]. To increase energy storage in a compact package, it is beneficial to have a dielectric constant greater than that of air or vacuum, so air and vacuum were not preferred. Some materials, such as ceramics, glasses, mica, and porcelain, exhibit higher dielectric constants [10]. However, the poor mechanical properties, including the brittle nature of these materials and difficulty in conforming them to certain geometries, limit their application for this system as well. Oxide layers find application in compact high capacitance electrolytic capacitors [11]. However, the very thin nature of the oxide layer inhibits its use in very high voltage applications. Although the dielectric constants of many plastics and oils only range between 2 and 3, the capacitance can be noticeably increased over that in air or vacuum [10]. Additionally, the increased dielectric strength of the plastics and oils allows the capacitor size to be minimized, which aids in both conforming to the size restraints of the system and decreases inter-electrode distance for a higher capacitance. The easy capability to machine or form plastics to the desired

geometry along with the fluid nature of oil allows the dielectrics to be adapted to most capacitor geometries. Finally, the similarity of the plastics and oils with the pulse transformer dielectrics provides compatibility between the system components. Therefore, a combination of thermoplastics and transformer oil was chosen as the best candidates for the dielectric media of the high voltage capacitors. Three capacitors of different geometries were built and tested as prototypes for this system. The first, a tri-plate capacitor, was built as a proof of concept for testing of the full power conditioning system with RF production. The second and third capacitors were then designed in conformance with the system size and geometry restraints.

5.1.1 Tri-Plate Capacitor

The high voltage capacitor is a critical system component for storing energy at high voltage and for forming a high frequency resonant circuit. Since the first high voltage capacitor was a prototype for proof of principle testing with the pulse transformer and fuse, a low inductance tri-plate geometry was chosen. The tri-plate geometry results in twice the capacitance of a single parallel plate. Additionally, placing ground plates on both sides of the center high voltage plate provides shielding of the high voltage center plate from surrounding components, such as the shunt inductor. The equation used for the capacitance of a tri-plate capacitor is given as equation (71).

$$C_{tri-plate} = \frac{2\varepsilon_0\varepsilon_r w_p l_p}{d_p} \quad (71)$$

The permittivity of free space is given as ε_0 [F/m], and the relative permittivity is represented as ε_r . The width and length of the center high voltage conductor are w_p [m] and l_p [m], respectively. The distance between high voltage and ground plates is

represented as d_p [m]. The equation assumes that the tri-plate is in a symmetrical geometry such that the effective area and the distances between the high voltage plate and each ground plate are the same for both of the capacitors that form the tri-plate.

The inductance of the tri-plate was kept minimal to increase the resonant frequency of the RF source. Factors influencing the inductance of the capacitor can be estimated from the equations derived for a parallel plate transmission line [12]. Since the tri-plate capacitor forms two parallel plates, the inductance is divided by two.

$$L_{tri-plate} = \frac{\mu_0 \mu_r d_p l_p}{2w_p} \quad (72)$$

To increase the capacitance while minimizing the inductance, the width must be increased while the distance between conductors must be decreased. The length and width of the capacitor were limited by the oil bath in which it was submerged. The maximum length and width that the oil bath could fit were approximately 50 cm and 35.5 cm, respectively. The widths of the conductors were further limited to provide sufficient overlap of the dielectric insulators to prevent flashover. The dielectric clamping rods required approximately 2.54 cm on each side of the capacitor. The distance between the high voltage and ground plates, d_p , was also limited by the high voltage requirements. The capacitor was meant to be used for many shots, so the capacitor was designed to operate well under the limits of the dielectric strength. Both dielectric breakdown and flashover along the dielectric edges were considered. The distance was minimized to increase the capacitance up to a point where the chances of punch through were kept minimal. For a dielectric strength of 787 kV/cm and a thickness of 1.9 cm, the dielectric sheets can hold off approximately 1.5 MV. Table 16 shows the design parameters for the high voltage capacitor.

Table 16. High Voltage Capacitor Parameters

w_p (m)	l_p (m)	d_p (m)	ϵ_r
0.292	0.445	0.019	2.25
Area (m ²)	$C_{tri-plate}$ (pF)	$L_{tri-plate}$ (nH)	Characteristic Impedance (Ω)
0.13	272.5	18.2	8.2

The tri-plate capacitor was constructed with polyethylene sheets, double-sided PC board, insulating all thread rods and nuts, and copper shim stock. The polyethylene sheets were 1.905 cm thick and served as the dielectric between the high voltage and ground conductors. Sheets were also placed on the top and bottom of the capacitor to clamp the ground conductors as flat as possible against the inner dielectrics. The center PC board extended beyond the polyethylene and was connected to the high voltage center terminal of the pulse transformer. The two outer PC boards extended beyond the polyethylene on the opposite side of the stack and were connected to the ground plane running along the bottom of the oil tank. The entire stack was clamped together with seven dielectric all thread rods and nuts on each side. Figure 52 shows the assembled tri-plate capacitor.



Figure 52. Tri-plate capacitor

To minimize the probability of flashover at the ends of the tri-plate capacitor, the high voltage and ground connections were made on opposite ends. This arrangement, however, increased the shunt inductance by requiring a conducting strip to run the length

of the capacitor. The inductance of the parallel plate structure formed by the shunt and the top ground plane of the capacitor can be estimated as two times that predicted by equation (72). Table 17 summarizes the parameters for the tri-plate shunt inductance. Figure 53 shows the tri-plate capacitor with the shunt conductor in oil.

Table 17. Tri-Plate Shunt Inductance

Width (cm)	Length (cm)	Shunt-GND Distance (cm)	Shunt Inductance (nH)
15.24	45	1.9	70.50

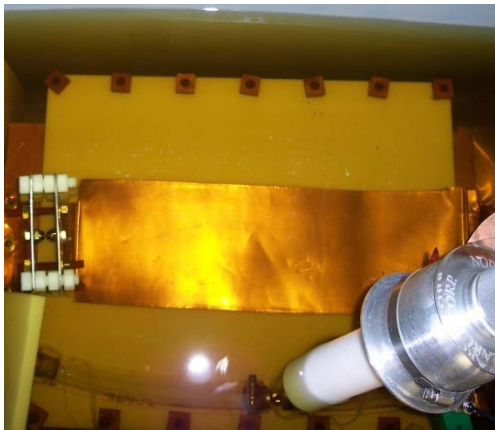


Figure 53. Tri-plate RF source in oil

5.1.2 Spiral-Strip Capacitor

The tri-plate high voltage capacitor used for initial system testing was capable of holding off voltages of several hundred kilovolts. However, the tri-plate geometry has a relatively large volume and does not conform to the system design constraints. Therefore, the capacitor had to be redesigned to the cylindrical geometry and maximum 15.24 cm diameter to which the pulse transformer and exploding wire fuse were built.

Given the results of the spiral-strip pulse transformers, several aspects of the design and construction of the spiral-strip capacitor were adapted from those proven by the pulse transformer. Stacks of thin thermoplastic films were used as dielectric insulation, which allowed the capacitor to be wound around a cylindrical core. The high voltage connection

was made along the center axis of the cylinder to adequately distance the high voltage input terminal from the ground foil. This geometry also provided a direct coaxial connection with the high voltage output of the pulse transformer.

The capacitor was constructed as a long parallel-plate capacitor wound around a cylindrical mandrel. Beginning with the mandrel, layers were formed first with the HV foil, the first dielectric layer, the ground foil, and an additional dielectric layer. This initial arrangement forms a parallel-plate capacitor with an extra dielectric layer on top. When the length of the foils is larger than the circumference of the first winding, the additional turns will form two capacitive layers per turn, increasing the electrostatic energy storage in a given volume. Figure 54 shows a conceptual view of the winding cross-section.

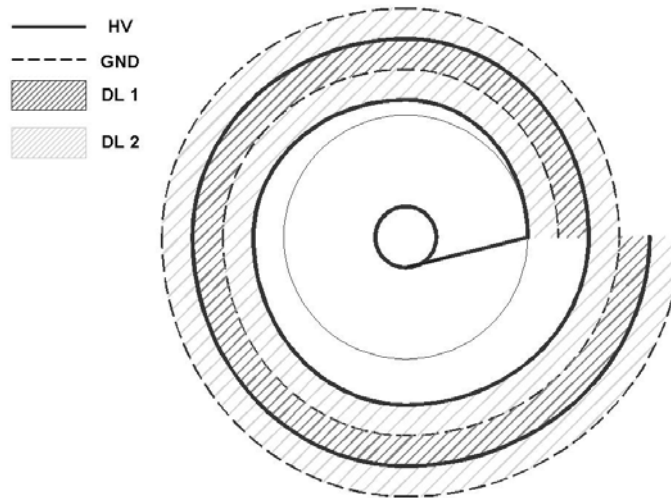


Figure 54. Simplified cross-section of winding pattern

Neglecting the effects of the radius of curvature, the capacitance of the cylindrical geometry can then be estimated by equation (73). The symbol l_p [m] is the length of the foils, and w_p [m] represents the width of the HV foil. The symbol r_{ss} [m] is the average radius of the first turn, and the distance between adjacent foils is d_p [m].

$$C_{ss} \cong \frac{2\varepsilon_0\varepsilon_r(l_p - \pi r_{ss})w_p}{d_p} \text{ for } l_p \geq 2\pi r_{ss} \quad (73)$$

The capacitor was wound on a 30.5 cm long cylindrical mandrel with approximately a 7.75 cm diameter. The width of the high voltage foil was approximately 22.75 cm, and the length was 61 cm. Ten 508 μm thick Teflon films were wound between the capacitor foils for a total dielectric thickness per layer of 5.08 mm. The windings were impregnated with oil, and the capacitor was operated in an oil bath. The outer diameter of the wound capacitor was within the 15.24 cm limit. The predicted capacitance from equation (73), using 2.1 for ε_r , is 850 pF. The measured capacitance with the capacitor submerged in oil was approximately 730 pF. The difference between the predicted and measured values is largely a result of the gaps between foils where the layers were not wound directly on top of each other. The capacitance increase from the tri-plate prototype to the present cylindrical version was 265%. Figure 55 shows the spiral-strip capacitor, and Figure 56 displays the arrangement of the capacitor with the pulse transformer and other load components.



Figure 55. Cylindrical capacitor with axial high voltage connection



Figure 56. Full system load with pulse transformer at upper left

5.1.3 Coaxial Cylindrical Capacitor

The third high voltage capacitor was designed in a coaxial cylinder geometry. The geometry has advantages of a cylindrical form, a high voltage connection on the center axis, a small diameter, and the use of oil as the bulk dielectric medium. Additionally, the construction of the capacitor is much more easily performed than the winding of films in a spiral-strip capacitor. The coaxial cylinder capacitor is formed by aligning conducting cylinders along the same cylindrical center axis. Each successive cylinder has a larger radius and opposite polarity to the previous cylinder. A cross-sectional representation is shown in Figure 57 to illustrate the geometry.

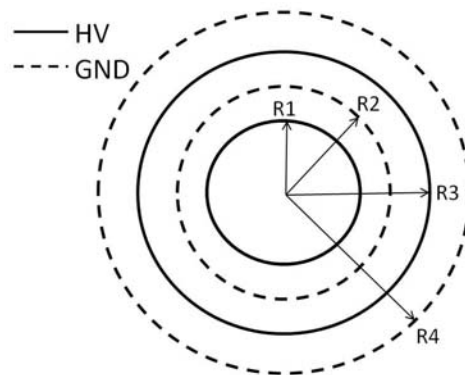


Figure 57. Simplified cross-section representing the coaxial cylinder geometry

The cylinder with the smallest radius was directly connected with the axial high voltage output of the pulse transformer. The cylinder with the largest radius is at ground

potential, which is ideal for encasing the system or for placing the capacitor adjacent to the ground plane in the experimental setup.

The capacitance of coaxial cylinders has been thoroughly studied for their common use as transmission lines. The capacitance of a coaxial line is given by equation (74) [13]. The symbol a [m] is the radius of the inner cylinder. The symbol r_{out} [m] and r_{in} [m] represent the inner radius of the outer cylinder and the outer radius of the inner conductor, respectively. The symbol l_c [m] represents the length of the cylinders.

$$C_{CC} = \frac{2\pi\epsilon_0\epsilon_r l_c}{\ln\left(\frac{r_{out}}{r_{in}}\right)} \quad (74)$$

With the multiple capacitive layers of the coaxial cylinder geometry of Figure 57, equation (74) can be expanded to give the total capacitance. The thickness of the conductors is considered negligible. The cylinder radii $R1$, $R2$, $R3$, and $R4$ are arranged as shown in Figure 57.

$$C_{CC} = 2\pi\epsilon_0\epsilon_r l_c \left[\frac{1}{\ln\left(\frac{R2}{R1}\right)} + \frac{1}{\ln\left(\frac{R3}{R2}\right)} + \frac{1}{\ln\left(\frac{R4}{R3}\right)} \right] \quad (75)$$

As previously stated, one of the advantages of the coaxial cylinder geometry is the relative ease of construction compared with a spiral-strip capacitor. Each of the conducting cylinders was formed by affixing a single layer of copper foil to a PVC pipe of known diameter. For cylinders with radii $R2$, $R3$, and $R4$, a copper tab protruded from the cylinder for electrical connection. For high voltage insulation, the tab from the cylinder with radius $R3$ was placed on the opposite side as the tabs from cylinders with radii $R2$ and $R4$. The cylinders were held in place by two end insulators and insulating

threaded rods. To reduce the inductance of the oscillating circuit, the oil spark gap switch was connected directly to the tabs of the capacitor.

The outer diameter of the largest cylinder is 8.23 cm, making the coaxial cylinder the most compact geometry investigated. The predicted capacitance, as calculated with equation (75), was 337 pF. However, the measured capacitance in oil was much higher at 459 pF. Upon disassembling the capacitor after testing, it was determined that the oil greatly inhibited the adhesive used to affix the foils to the PVC piping, resulting in the foil at radius R_2 detaching from the outer diameter of the 0.0206 m pipe and unwinding to the inner radius of the 0.0302 m pipe. The effective increase of the radius R_2 greatly reduced the distance between adjacent foils and could explain the unexpectedly high capacitance value. As this foil movement also puts the capacitor at much greater risk for dielectric breakdown at high voltage, adhesives with improved compatibility with oil are required. Two views of the coaxial cylinder capacitor are shown in Figure 58. Table 18 summarizes the parameters of the coaxial cylinder capacitor.

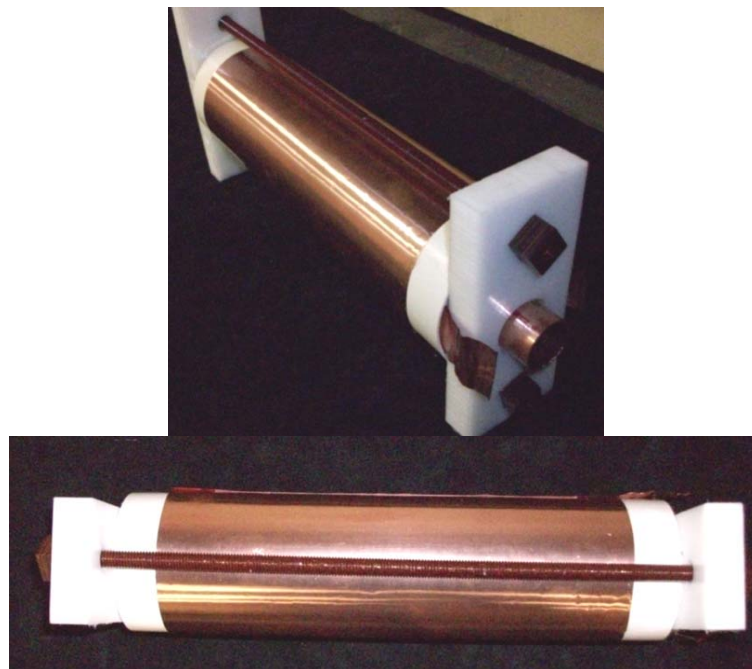


Figure 58. Assembled coaxial cylinder capacitor

Table 18. Coaxial Cylinder Capacitor Parameters

$R1$ (m)	$R2$ (m)	$R3$ (m)	$R4$ (m)
0.0159	0.0206	0.0302	0.0413
l_c (m)	ϵ_0 [F/m]	ϵ_r	
0.27305	8.85E-12	2.3	
Predicted Capacitance in Oil (F)	Measured Capacitance in Air (F)	Measured Capacitance in Oil (F)	
3.37E-10	2.02E-10	4.59E-10	

5.2 Aqueous-Electrolyte Load Resistor

The load of the power conditioning system can be a radiating antenna or a dummy load. The dummy load approximates the impedance of a specific antenna or the impedance of free space radiation. For the most of the characterization tests of the power conditioning system, an aqueous resistor was implemented as a dummy load. The choice of an aqueous resistor had the advantages of ease of control of the resistivity, length, and resistance. Aqueous resistors can be used in pulsed high fields of less than 15 kV/cm with less than 10% variation in the resistance [14]. The resistivity can be a function of temperature [14]. However, due to the single shot nature of this investigation, the effects of temperature are negligible. The resistivity, ρ [$\Omega\cdot\text{cm}$], of an aqueous-electrolyte solution can be described by equation (76) where constants K_1 and K_2 are dependent on the solute [14]. The variable c [g/L] is the concentration of solute in water.

$$\rho = K_1 c^{K_2} \quad (76)$$

The curve-fit constants and electrode material compatibility for the solutes used during the course of this investigation, copper sulfate and sodium thiosulfate, are provided in Table 19.

Table 19. Parameters for Aqueous-Electrolyte Solutes [14]

	K_1	K_2	Electrode Compatibility
Copper Sulfate	1553	-0.7465	Copper
Sodium Thiosulfate	1173	-0.901	Aluminum

To ensure that the resistivity remains constant at high frequency, the skin effect must be considered. Assuming a cylindrical resistor, the radius r_{aq} [cm] must be less than 10%-20% of the skin depth, δ [cm] [14]. The skin depth is dependent on the frequency. When the resistivity-frequency product is much greater than 14.3 MHz- Ω ·cm, the skin depth can be approximated by equation (77) [14]. The relative permittivity of the solution, ϵ_r [F/m], can be estimated as the permittivity of water, 81.

$$\delta \cong 0.53\rho\sqrt{\epsilon_r} \quad (77)$$

For a resistivity on the order of 65 Ω ·cm and a peak operating frequency of 300 MHz, equation (77) can be used. The skin depth for a water-based resistor is calculated to be 310 cm, and the maximum radius of the resistor is 31 cm.

The self-inductance, L_{aq} [H] of an aqueous-electrolyte resistor can be estimated from equation (78) [15]. The length of the resistor is represented as l_{aq} [cm].

$$L_{aq} \approx \left(2l_{aq} \left[\ln \left(\frac{2l_{aq}}{r_{aq}} \right) - 0.75 \right] \right) \times 10^{-9} \quad (78)$$

For a resistor radius of 1.27 cm and a maximum length of 35.5 cm, the maximum self-inductance of the load is approximately 233 nH. For a load resistance approximating the free-space impedance, 377 Ω , the L/R time constant is 618 ps.

Two resistors in series formed the load resistor and provided a voltage divider for high voltage measurements, as discussed in Chapter 6. The total resistance was made to approximate the free space impedance of 377 Ω . The lengths of the resistors were approximately 25.4 cm and 10.2 cm. The load resistor was contained in Tygon tubing

with a 2.54 cm inner diameter. Both copper sulfate and sodium thiosulfate were used throughout the investigation.

5.3 Secondary Low Inductance Switch

The shunt inductance forms the magnetic energy storage element of the underdamped LC circuit. The inductance of the spark gap switch and leads form the total shunt inductance. As seen in equation (70), increase of the shunt inductance lowers the damped resonant frequency of the circuit. Minimizing the shunt inductance allows the capacitance to be increased for maximal energy storage for a given peak charging voltage and resonant frequency. Thus, the shunt inductance should be as low as possible. The leads from the capacitor to spark gap were made as wide strips. The width of the strips was limited to prevent breakdown between the leads at the capacitor terminals.

The inductance of an arc discharge in a spark gap with a coaxial current return path can be described as a coaxial transmission line. For an inter-electrode distance l_g [m], a return current radius R_r [m], and an arc radius r_a [m], the arc inductance, L_g [H], can be described by equation (79).

$$L_g = \frac{l_g \mu_0}{2\pi} \ln \left(\frac{R_r}{r_a} \right) \quad (79)$$

The inductance of the arc discharge is directly proportional to the length of the discharge. Implementing a dielectric medium with a high dielectric strength allows the length of the inter-electrode gap to be minimized, decreasing the inductance. To lower the switch inductance, transformer oil was used as the dielectric material in the switch. Table 20 shows typical values for the secondary switch. The inductance of the switch, assuming an arc radius of 0.5 mm, is approximately 1 nH. The inductance can further be reduced by

decreasing the current return radius. The switch inductance is small compared to the inductance of the shunt, and the resonant frequency of the shunt path is dominated by the effects of the shunt inductor.

Table 20. Typical Secondary Switch Parameters

L_g [m]	R_r [m]	r_a [m]	L_g [H]
0.001	0.0762	0.0005	1.005E-09

The variation of the switch inductance is of particular interest. While the inductance of the leads is constant during system operation, the inductance of the spark gap arc is variable. As detailed by Persephonis *et al.*, the inductance of a switch can vary greatly over the conduction time of the arc [16]. The inductance varies based upon the geometrical relationship of the conductors, as seen in equation (79). Specifically, the change in the radius of the arc discharge alters the inductance of the switch [16]. The logarithmic nature of the dependence of the arc radius in equation (79) suggests small inductance variations for changes in the discharge radius. However, an analysis of the arc discharge inductance by Persephonis *et al.* for a high frequency underdamped discharge exhibited dramatic variation of the arc inductance. After an initial peak in the inductance at the beginning of the discharge, the inductance followed a slowly decreasing trend due to plasma diffusion and channel expansion as the conduction time increases [16]. Additionally, much larger fluctuations of the inductance were observed to follow the changes in the current magnitude [16]. The authors attribute this effect due to constriction and expansion of the discharge diameter from current self-focusing [16]. These fluctuations in the spark gap inductance could produce noticeable effects in the output of the RF source. For a minimized shunt inductance in which the spark gap inductance is significant, variations in the spark gap inductance can change the resonant frequency of

the circuit. Small changes in the resonant frequency of the circuit will be seen as a spreading effect of the frequency content around the expected natural frequency.

References for Chapter 5

- [1] F. B. Frungel, *Capacitor Discharge Engineering* vol. III. London: Academic Press, Inc., 1967.
- [2] C. K. Alexander and M. N. O. Sadiku, *Fundamentals of Electric Circuits*: McGraw-Hill Higher Education, 2000.
- [3] Maxwell Technologies (Access Confirmed Nov. 2008). High voltage capacitors CDOR CDCT CDHT. [Online]. Available: http://www.maxwell.com/pdf/hv/high_voltage_capacitors_catalogue.pdf.
- [4] Morgan ElectroCeramics (Access Confirmed Nov. 2008). Capacitors - doorknob RF transmitting capacitors. [Online]. Available: <http://www.morganelectroceramics.com/capacitors/capdoor.html>.
- [5] General Atomics (Access Confirmed Nov. 2008). Series C high voltage energy storage capacitors. [Online]. Available: <http://www.gaep.com/series-c-capacitors.html>.
- [6] Aerovox Corp. Custom and pulse power capacitors. [Online]. Available: http://www.aerovox.com/pdf/Power_Electronics-1.pdf.
- [7] General Atomics (Access Confirmed Nov. 2008). High voltage fast pulse capacitors. [Online]. Available: <http://www.gaep.com/series-pds-pdss-capacitors.html>.
- [8] High Energy Corp. EPSR series: high voltage pulse power. [Online]. Available: <http://www.highenergycorp.com/download/epsrsheetb.pdf>.
- [9] High Energy Corp (Access Confirmed Nov. 2008). Energy storage capacitors. [Online]. Available: <http://www.highenergycorp.com/download/oilcat3.pdf>.
- [10] C. J. Kaiser, *The Capacitor Handbook*. Olathe, KS: CJ Publishing, 1993.
- [11] G. W. A. Dummer and H. M. Nordenberg, *Fixed and Variable Capacitors*. New York, NY: McGraw-Hill and Co., 1960.
- [12] G. F. Miner, *Lines and Electromagnetic Fields for Engineers*. New York, NY: Oxford University Press, 1996.
- [13] F. T. Ulaby, *Fundamentals of Applied Electromagnetics*. Upper Saddle River, NJ: Prentice Hall, 2001.
- [14] R.E. Beverly III and Associates (Access Confirmed Nov. 2008). Application Notes for Aqueous Electrolyte Resistors. [Online]. Available: http://www.reb3.com/pdf/r_appl.pdf.
- [15] F. W. Grover, *Inductance Calculations, Working Formulas and Tables*. New York: D. Van Nostrand, 1946.
- [16] P. Persephonis, K. Vlachos, C. Georgiades, and J. Parthenios, "The inductance of the discharge in a spark gap," *Journal of Applied Physics*, vol. 71, pp. 4755-4762, 1992.

Chapter 6: Experimental Results

6.1 Diagnostics

Diagnostics were implemented with the power conditioning system to optimize and characterize the system performance. The measurements of greatest interest were the primary circuit current and the secondary capacitor voltage. The primary circuit current measurement provides the output current of the FCG or FCG simulator as well as the current through the transformer primary winding and exploding wire fuse. The primary circuit current can be used to determine the total inductively-stored energy. Additionally, the current through the fuse allows for the determination of the appropriate action integral and characterization of the current interruption. The secondary capacitor voltage is the most critical measurement to determine the peak charging voltage, oscillation magnitudes, and frequency of secondary oscillations. Additionally, the voltage of the FCG simulator capacitor bank was monitored during charging, and the fuse voltage and secondary winding current were measured in some experiments.

The oscilloscope used for data acquisition in this study, which will be described later in this section, was rated for peak input voltage levels of 150 V peak for a 1 M Ω input impedance and 10 V peak for a 50 Ω input impedance [2]. Therefore, for high voltage and current measurements, the voltage and current diagnostics incorporated resistive voltage dividers and signal attenuators, respectively. The voltage measurements were performed with resistive voltage dividers. If a voltage is present across two known resistances in series, as shown in Figure 59 as R_1 and R_2 , the voltage can be determined as a multiple of the measured voltage, v_m . The ratio of the measured voltage to the total

voltage is given by equation (80). Equation (80) applies when the effects of reactive elements can be neglected.

$$\frac{v_m}{v_0} = \frac{R_2}{R_1 + R_2} \quad (80)$$

The value of R_1 is often greater than R_2 , so the measured voltage is a small fraction of the actual voltage. High voltage measurements often require the incorporation of dielectric insulation and larger device components than low voltage probes to prevent electrical breakdown of the divider or voltage probe. Additionally, high frequency measurements require shielding of the divider and capacitive compensation to reduce the probe rise time.

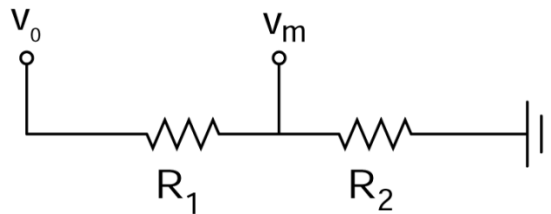


Figure 59. Simple voltage divider for high voltage measurements

For measurements of voltages greater than the peak rated voltage of the high voltage probes, as when measuring the secondary capacitor and fuse voltages, additional resistive voltage dividers made from aqueous resistors were implemented. The expected voltages across the fuse and secondary capacitor both exceeded the ratings of the high voltage probes, which will be described later in this section. Therefore, both measurements required additional voltage dividers in the circuit. The desired voltage measurement can be obtained by applying equation (80) for both the circuit resistive divider and the resistive divider within the voltage probe. Aqueous-electrolyte voltage dividers were made based upon the guidelines discussed in Chapter 5 [3].

Voltage measurements on the secondary capacitor required both high voltage and high frequency diagnostics. The North Star High Voltage PVM6 high voltage probe was implemented for this measurement [4]. The probe is rated to measure voltages up to 100 kV. The PVM6 is calibrated for a 1000:1 ratio of actual voltage to measured voltage. The probe is calibrated for use with 9.144 m of 50 Ω RG-223 cable and is terminated at a 1 M Ω input resistance at the oscilloscope. At frequencies up to 80 MHz, the error is less than 4%. The Tektronix P6015A passive high voltage probe was utilized for fuse voltage measurements. The ratio of the actual voltage to the measured voltage of the P6015A is 1000:1. The P6015A is rated for a peak voltage of 40 kV with a pulse duration of less than 100 ms and can measure frequencies up to 75 MHz [5]. The probe has a 3.05 m cable and a calibration box, which is terminated at a 1 M Ω oscilloscope input resistance. Charging of the FCG simulator capacitor bank was monitored using a Fluke 80K-40 voltage probe. The probe is designed for performing high voltage DC measurements to be monitored on a Fluke multimeter. The Fluke 80K-40 was used to verify the peak charging voltage before degassing the pressurized spark gap switch, thus triggering the FCG operation. The ratio of actual voltage to measured voltage is 1000:1.

Current measurements were made using a current transformer. If the current-carrying element passes through an enclosed multiple-turn winding around a magnetic core, magnetic coupling between the current-carrying element and the winding will cause a voltage across the multiple-turn winding. The geometry of the conductor and windings forms a transformer with a single turn primary and multiple turn secondary. The voltage induced on the secondary winding is integrated, and the current in the single turn is then directly proportional to the measured voltage. The peak current and pulse duration of a

current transformer is limited by the saturation of the magnetic core, which is determined by the saturation equations presented in Chapter 2.

The measurement of high currents on the order of tens of kiloamps required the implementation of additional signal attenuators to reduce the input signal to the oscilloscope to acceptable levels. The attenuators are rated in decibels. The ratio of the attenuator output voltage to the input voltage can be expressed by equation (81), where the rated attenuation, a [dB], is a negative number.

$$\frac{v_{out}}{v_{in}} = 10^{\frac{a}{20}} \quad (81)$$

The selection of a current monitor was made under the assumption that the FCG would supply a primary current peak up to 40 kA with a maximum risetime of 14 μ s. The Pearson Electronics 101 current monitor was implemented based upon its maximum current rating of 50 kA and maximum volt-second product of 2.5 V·s [6]. The upper frequency limit is rated at approximately 4 MHz, and the inner diameter of the current monitor, through which the current-carrying element must pass, is approximately 5.33 cm [6]. The ratio of voltage output to current measured by the P101 is 1:100 [6]. The current monitor is connected with a 50 Ω RG-58 cable into a 50 Ω oscilloscope input resistance. When terminated into 50 Ω , the measured voltage is reduced by a factor of two. Additionally, two 50 Ω attenuators with a total signal attenuation of -40 dB were also implemented to reduce the input signal to the oscilloscope to less than 10 V. The current monitor was positioned at the grounded terminal of the exploding wire fuse to prevent arc discharges to the grounded case of the current monitor.

A Tektronix TDS 5054B Digital Phosphor Oscilloscope was utilized for data collection. The 5054B model is a 4-channel oscilloscope with a 500 MHz bandwidth [2].

The maximum sampling rate is 1.25 GS/s per channel when 3 or 4 channels are used and 5 GS/s or 2.5 GS/s per channel when 1 or 2 channels are used, respectively [2]. The oscilloscope was triggered by the negative edge of the primary current signal, corresponding to current interruption. Figure 60 illustrates the positioning of the diagnostics as previously described.

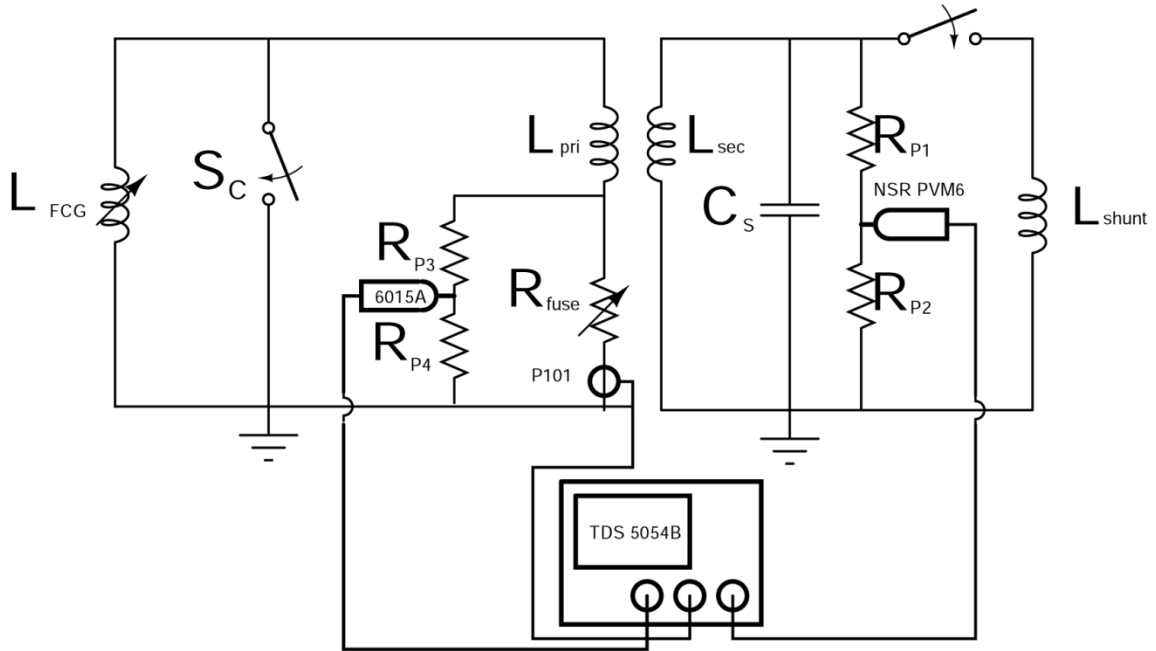


Figure 60. Experimental arrangement with diagnostics

6.2 Experimental Results of the Power Conditioning System and FCG Simulator

Many experiments were conducted with the FCG simulator to test the power conditioning components. Final experiments were aimed at full system operation with a current input similar to that expected from a TTU FCG. Full experiments were conducted with the tri-plate, spiral-strip, and coaxial cylinder RF sources. A dummy resistive load was used in place of an antenna in all of these experiments. The diagnostic setup was identical to that described in section 6.1 and shown in Figure 60.

A typical experimental setup is shown in Figure 61. The components at the upper left form part of the inductive network of the FCG simulator. The gray container contains the oil bath with the pulse transformer and RF source components. The North Star High Voltage PVM 6 is seen protruding from the oil bath. The fuse, packed in fine glass beads, is arranged vertically outside the gray container. The entire assembly is supported by the steel cage containing the primary energy storage capacitors.

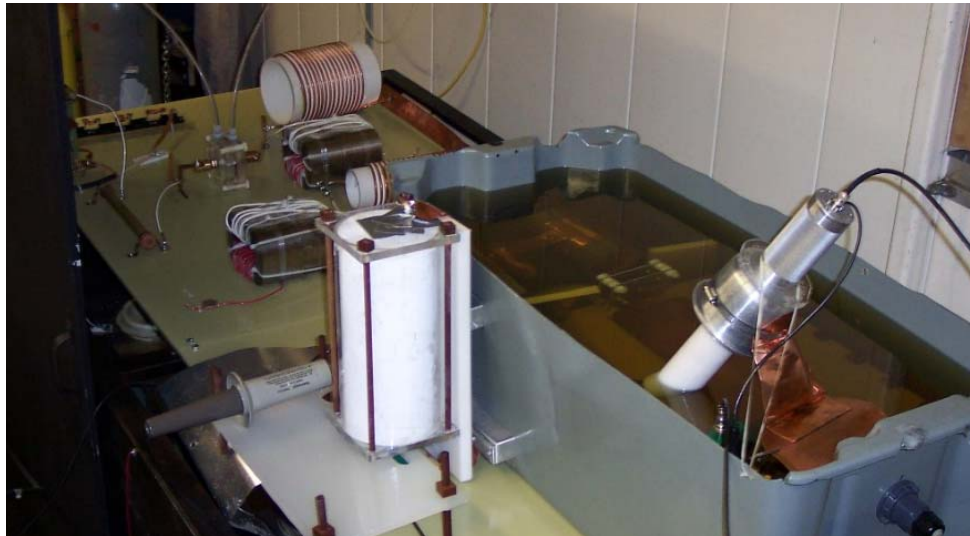


Figure 61. Power conditioning system at lower right with FCG simulator at upper left

6.2.1 Experimental Results of the Tri-Plate Capacitor and FCG Simulator

The tri-plate capacitor was used in the initial full system experiments due to its high voltage capabilities. A resistive load of 369 ohms was placed in parallel with the 275 pF capacitance to act as a dummy load and a voltage divider for high voltage measurements. The pulse transformer had a 1 μH primary and an 8.25 μH secondary self-inductance. The coupling factor was approximately 0.8. A fuse consisting of 28 wires was implemented to obtain an action limit on the order of 1000s A^2s . The fuse length of approximately 30.5 cm ensured holdoff of a voltage up to 183 kV, assuming a dielectric strength of 6 kV/cm. An oil gap spacing of approximately 1.1 mm was implemented for a

self-break voltage of approximately 200 kV. A crowbar switch was placed in parallel with the transformer primary and fuse. The atmospheric pressure air gap was set to 1 cm for a breakdown voltage of approximately 30 kV.

The capacitor bank of the FCG simulator was charged to 25 kV. As seen in the primary current waveform of Figure 62, the FCG simulator current reached a peak of greater than 32 kA. The increasing rate of current rise due to saturation of the magnetic switches is seen early in the current rise. The operating time of the FCG simulator, from the beginning of operation until the current begins to rapidly be interrupted, is 12 μ s.

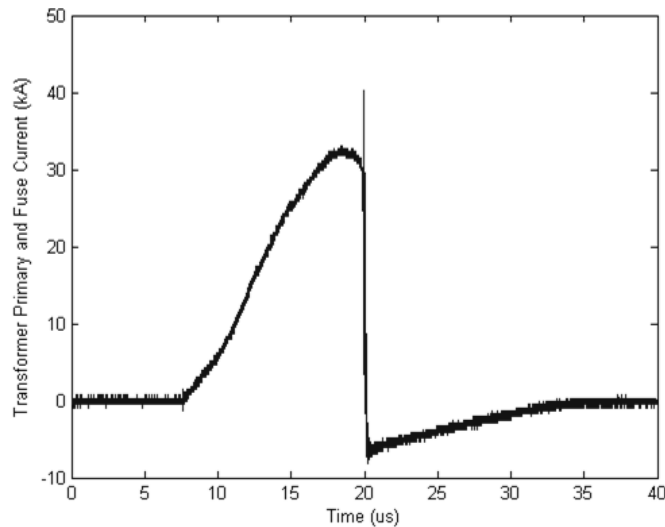


Figure 62. Full view of primary current rise and interruption

As the fuse opened, the current dropped to around 20 kA in about 150 ns before the oil switch on the secondary closed. The closure of the oil switch at this stage in system operation is evidenced by the large fluctuations in the fuse current, as seen in Figure 63. The large current oscillations are likely the result of the RF signal of the secondary being coupled to the primary circuit and diagnostics. The current in the transformer primary crosses zero within 200 ns of the beginning of current interruption.

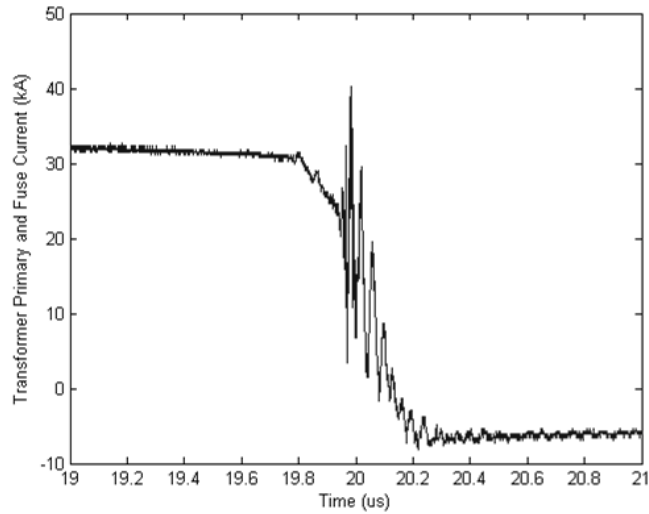


Figure 63. Detailed view of current interruption by fuse

The voltage across the load capacitor is shown in Figure 64. As the fuse decreases the primary current from 32 kA to about 20 kA, the capacitor is charged to over 200 kV. The oil gap then closed, resulting in the several oscillations that follow.

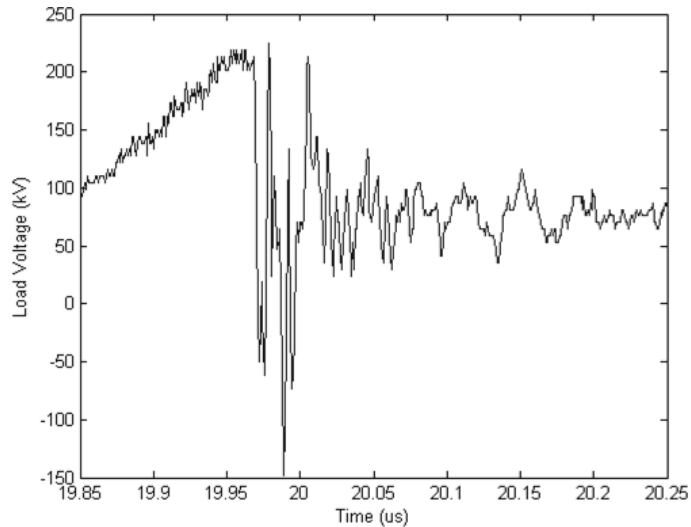


Figure 64. Load voltage at time of fuse opening

The peak RF power was greater than 130 MW. A total of seven voltage peaks correspond to peak powers greater than 50 MW. Figure 65 displays an overlaid plot of the load power and total power dissipated in the load. The load was in parallel with the high voltage capacitor, so energy was dissipated in the load before the oil gap closed.

During charging of the secondary capacitor, approximately 89 J were dissipated in the parallel load resistance. At $t = 20.25 \mu\text{s}$, the total energy dissipated in the load was greater than 94 J, meaning more than 5 J were dissipated in the very high frequency oscillations.

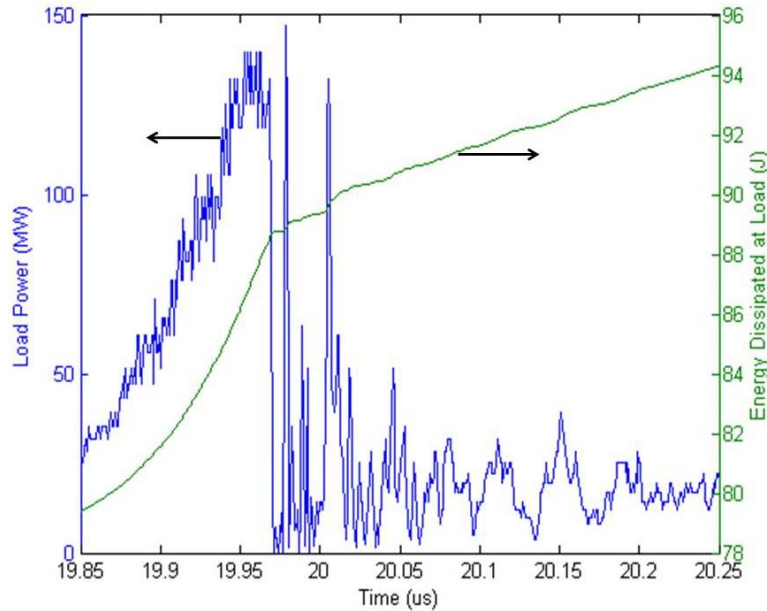


Figure 65. Load power and energy dissipated at load

There was a wide band of frequencies present in the secondary RF oscillations. As shown in Figure 66, there was significant frequency content up to about 250 MHz. The frequency content up to 250 MHz was consistently measured in several experiments.

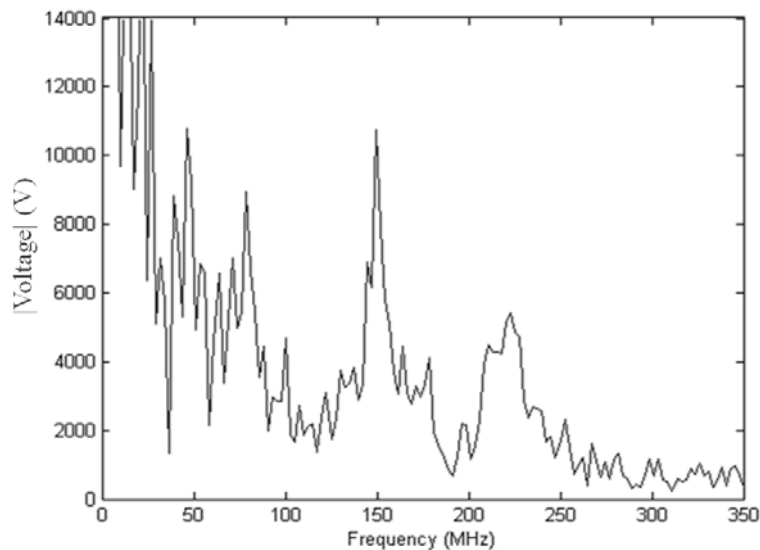


Figure 66. Frequency content of load voltage oscillations

Additional experiments with the tri-plate RF source, FCG simulator, and dummy load indicate that even higher voltages and powers have been achieved. It is believed that power levels above 250 MW have been reached. Problems obtaining full system diagnostic measurements and reliable switching of the oil spark gap have prevented the acquisition of adequate data to present full results at that magnitude. However, there is evidence of the higher voltage and higher power capabilities of this system. First, the spark gap on the secondary closed in several tests after the fuse had decreased the primary circuit current to only 20 kA. This suggests that about 200 J of inductively-stored energy was still available at the time the capacitor was fully charged. Increasing the spark gap electrode spacing could allow more energy to be transferred to the secondary circuit and the capacitance to be charged to much higher voltages. Secondly, the theoretical peak charging voltage of the secondary capacitance is several 100s of kV. As shown in section 6.3, the secondary can be charged to over 700 kV.

6.2.2 Experimental Results of the Spiral-Strip Capacitor and FCG Simulator

In addition to testing the compact spiral-strip capacitor geometry, the experiments in this section were performed with an attempt to better utilize the inductively-stored energy in the power conditioning system. As mentioned at the end of the previous section, experiments with the tri-plate capacitor indicated that the load capacitor would charge to high voltage and the secondary oil spark gap would close before the primary current reached zero amps. The majority of the inductively-stored energy at the time when the oil gap closed would be wasted as it would not contribute to the very high frequency load oscillations. This observation results in two opportunities. First, as previously mentioned, the oil gap can be set wider to charge the load capacitor to higher voltages. Second,

similar charging voltages can be achieved on the load capacitor with much lower energy sources. The latter opportunity was investigated in these experiments.

In the previously detailed experiment with the tri-plate capacitor, the peak primary current was 32 kA, corresponding to an inductively-stored energy of 512 J. However, at the time when the oil gap closed with a capacitor voltage of 200 kV, the primary current was 20 kA. The corresponding 200 J of inductively-stored energy remaining was therefore extraneous. To reduce wasted energy, a lower energy source of 312 J might have been used to achieve the same results with oil gap closure at peak voltage just as the primary current reached zero current. An inductively-stored energy of 312 J corresponds to a primary current of about 25 kA. Therefore, the FCG simulator charging voltage and fuse cross-sectional area were adjusted for peak currents around 25 kA in experiments with the spiral-strip capacitor.

The experiments were conducted with the FCG simulator at MU. An aqueous-electrolyte resistor of 384 Ω was implemented as a dummy load and as a voltage divider for capacitor voltage measurements. A second transformer was designed and built with the same parameters as the transformer used for the tests with the tri-plate capacitor. The same fuse form as that used in tests with the tri-plate capacitor was utilized. However, since the power conditioning system was driven with a current reduced by 22% from the previously-discussed experiment, the number of fuse wires was reduced to 17 40-gauge silver-plated copper wires. A crowbar switch was included to limit the effects of the inductance of the FCG simulator during the fuse resistance rise.

Figure 67 shows the current in the transformer primary and fuse opening switch as the current is interrupted. During a generator operating time of approximately 10 μ s, the

primary current reached a peak of approximately 25 kA. As the fuse resistance rapidly increased, the primary current fell from 22.5 kA to zero in 200 ns. Oscillations of the secondary were coupled to the primary circuit and diagnostics, resulting in large oscillations of the primary current.

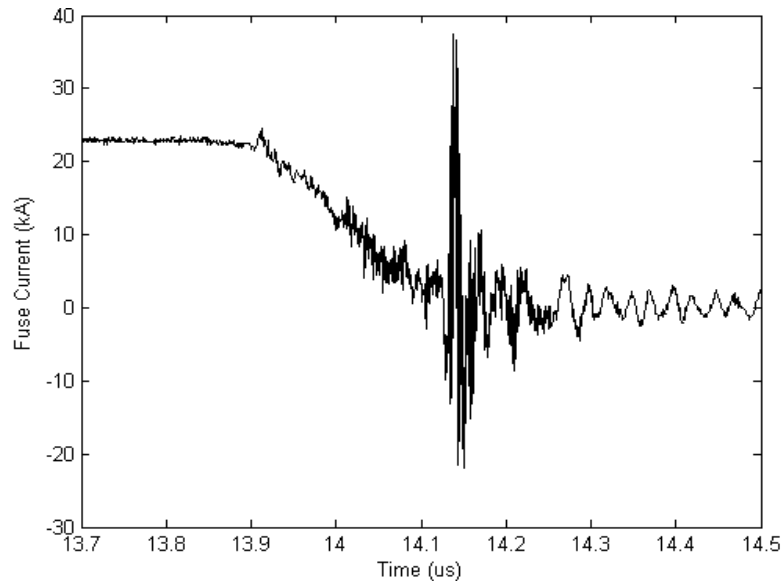


Figure 67. Detailed view of primary current waveform

Figure 68 gives a detailed view of the high voltage stages of load operation. The capacitor was charged to -190 kV before the oil spark gap closed to form an underdamped RLC circuit with the shunt inductance. Several very high frequency oscillations were present before a series of lower frequency oscillations. With the resistive load of 384Ω parallel to the capacitor, the peak load power was greater than 90 MW.

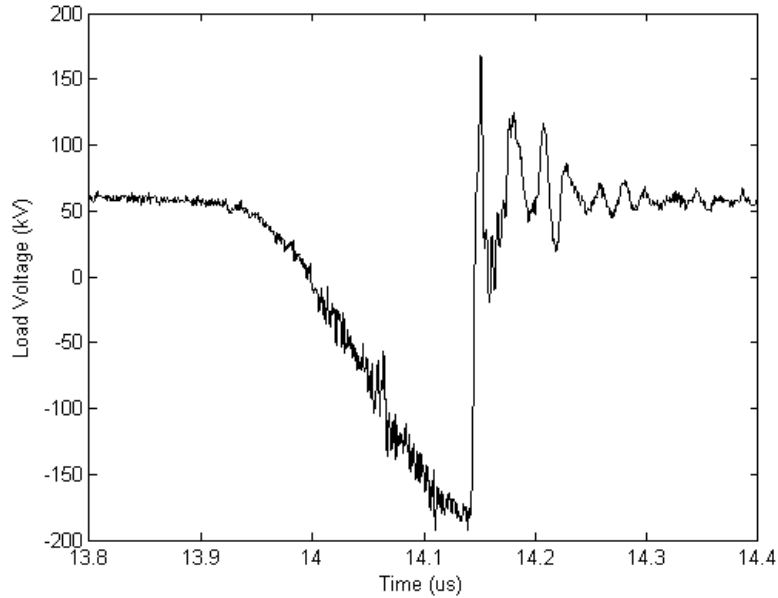


Figure 68. Detailed view of load voltage RF oscillations

Figure 69 shows the results of a fast Fourier transform of the secondary voltage oscillations shown in Figure 68. The peak values from the FFT are seen at 2.5 MHz, corresponding to the capacitor charging. The most significant frequency component of the secondary oscillations occurred at 40 MHz. There was significant frequency content up to about 75 MHz. Additional frequency components around 200 MHz formed the upper frequency limit. After the load capacitor had been fully charged, the load oscillation frequency content was mostly in the range from 30 MHz to 75 MHz. Therefore, this iteration of the load is considered a mesoband oscillator. Including the frequency content down to 2.5 MHz, the load is considered a hyperband oscillator [7].

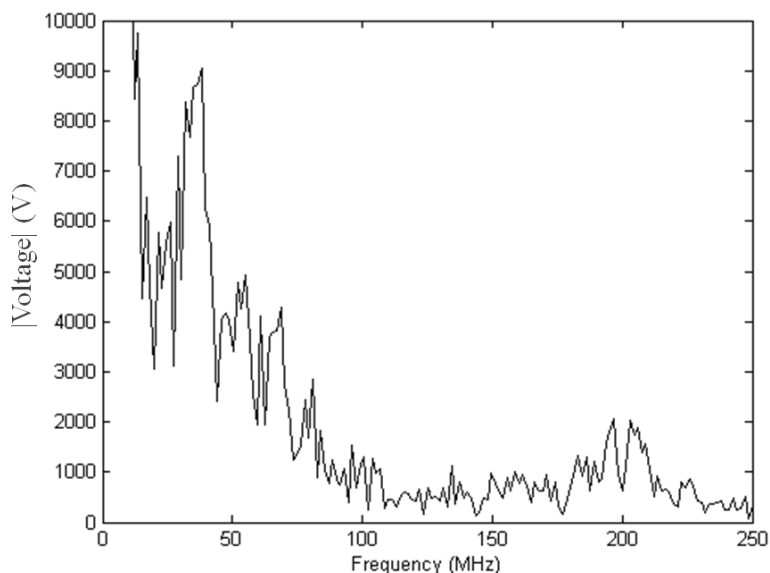


Figure 69. FFT of load voltage RF oscillations

Despite the increase in capacitance from the tri-plate geometry to the spiral-strip geometry, the peak charging voltage was only slightly lower than the peak levels obtained with the tri-plate capacitor and FCG simulator. The inductively-stored energy for this experiment with a peak current of 25 kA was 312.5 J. Compared to the previous experiment with a peak current of 32 kA and corresponding inductively-stored energy of 512 J, the inductively-stored energy was reduced by 39%. The ability to achieve similar peak charging voltages on a larger capacitance despite significantly reduced input energy demonstrates the compatibility of the power conditioning system and RF source with lower energy sources.

A possible component failure is dielectric breakdown in the compact high voltage capacitor. Nevertheless, this component failure can also result in successful system operation. In this case, the capacitor is shorted by dielectric failure before the oil spark gap closes. However, as seen in the detailed view of Figure 70, this situation also results in high frequency voltage oscillations. In an experiment with a primary current of 28.5 kA, dielectric breakdown occurred in the spiral-strip capacitor at about -190 kV, which is

believed to be due to air remaining between the dielectric layers. The subsequent peak reached 225 kV, corresponding to 130 MW. An FFT of the oscillations showed the peak frequency component to be 2.5 MHz, corresponding to capacitor charging, with frequency content up to 75 MHz. This situation demonstrates that for single-shot systems, the dielectric breakdown of the capacitor can produce the desired high frequency oscillations.

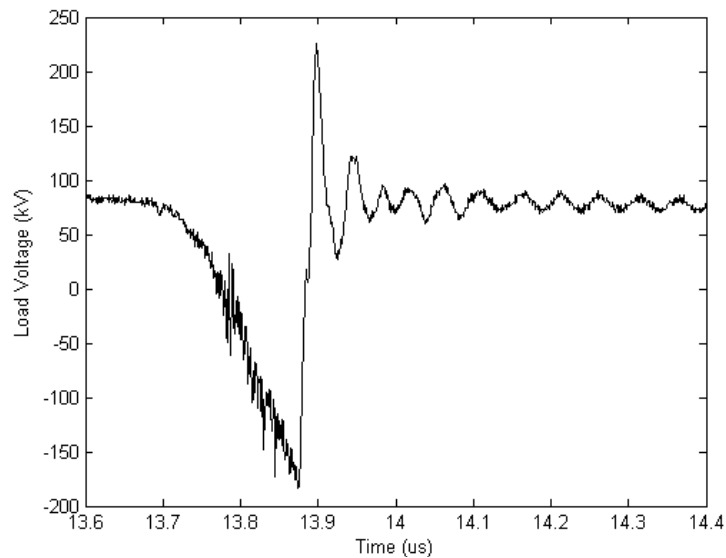


Figure 70. Detailed view of load voltage after dielectric breakdown

Another fault mode of operation occurs if the oil spark gap does not close. The relatively high value of the fuse resistance at this point in system operation allows the approximation of the inductance in parallel with the capacitor to be the secondary self-inductance. This inductance is much higher than the shunt inductance. Nevertheless, the secondary circuit will oscillate at lower frequencies. A wideband antenna that radiates in the lower band shown in Figure 69 can still radiate high power RF despite the incomplete system operation. It is seen as an advantage of the system that two of the most common load failures still result in high power RF generation.

6.2.3 Experimental Results of a Coaxial-Cylinder Capacitor and FCG Simulator

The final RF system tested was the coaxial-cylinder geometry. The tests with this capacitor were driven by the MU FCG simulator. In parallel with the coaxial-cylinder capacitor was a resistive load of $540\ \Omega$, which provided a divider for high voltage measurements and a load to substitute for a radiating antenna. The pulse transformer and fuse form were identical to those used in the tests of the spiral-strip capacitor. The fuse consisted of 18 40-gauge silver-plated copper wires in parallel. The capacitance in oil of the coaxial-cylinder capacitor was 459 pF.

Figure 71 and Figure 72 show the full and detailed primary current waveforms. The current rose to a peak of approximately 27 kA in about a 10 μs risetime. The current was then rapidly reduced from 25 kA to about 5 kA in approximately 150 ns. The inductively-stored energy when the RF oscillations began was approximately 12.5 J, so relatively little inductively-stored energy was wasted.

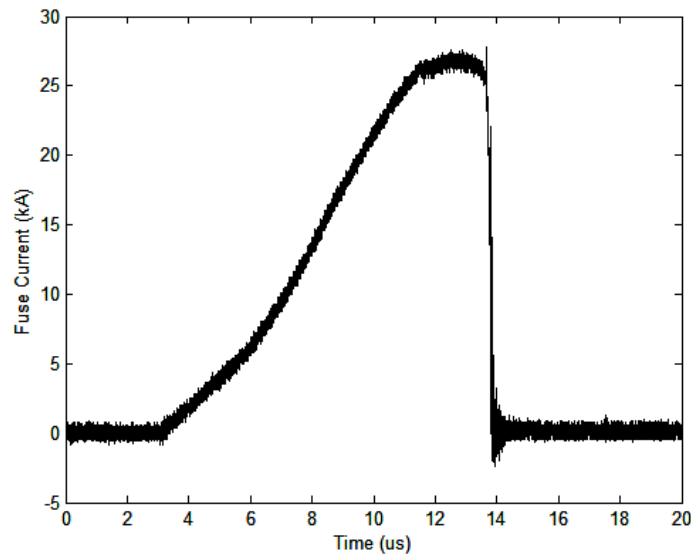


Figure 71. Full view of primary current for the test of coaxial-cylinder RF load

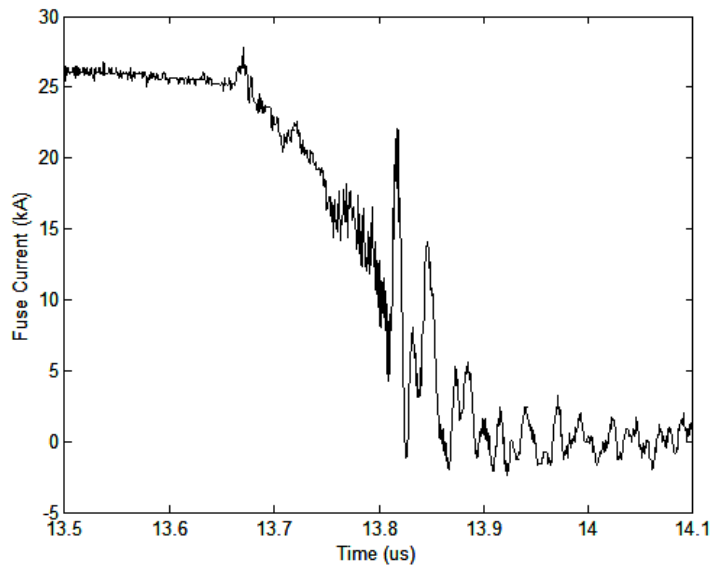


Figure 72. Detailed view of primary current in test of coaxial-cylinder RF load

Figure 73 and Figure 74 show the full and detailed load voltage waveforms. As the fuse resistance increased and energy was transferred to the secondary circuit, the load capacitor was charged to approximately -180 kV. At this point, a breakdown occurred that resulted in high power load oscillations. The peak RF power reached approximately 70 MW. The output power is somewhat lower due to the high dummy load resistance used in this experiment. The breakdown that resulted in RF oscillations was within the capacitor, so the system operation for this experiment was similar to the failure mode presented in the previous discussion. It is believed that the breakdown within the capacitor occurred due to the ineffective adhesives in oil. As previously described, one of the inner foils came off of the pipe it had been affixed to, which greatly reduced the gap between the free foil and the adjacent foil. Therefore, future coaxial-cylinder capacitors must use adhesives or other mechanisms that are more resistant to oil.

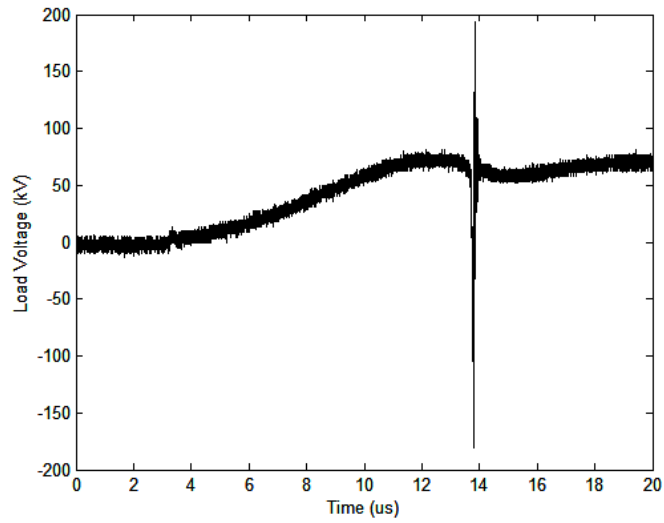


Figure 73. Full view of load voltage for coaxial-cylinder RF load

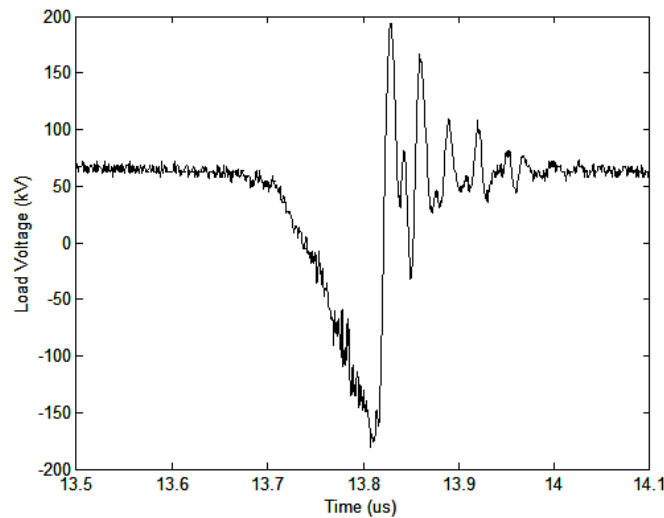


Figure 74. Full view of load voltage for coaxial-cylinder RF load

Figure 75 shows the FFT of the load voltage waveform in Figure 74. There was a very high peak less than 40 MHz as well as a wide peak from 50 MHz to 70 MHz. These wide frequency bands could be radiated by a wideband antenna. The peak frequencies may be limited by the inductance of the conducting path through the capacitor insulation. When the oscillating circuit is completed through closure of the oil switch, the shunt inductance

should be significantly lower. Preventing dielectric breakdown in the capacitor and lowering circuit inductances may increase the peak frequencies.

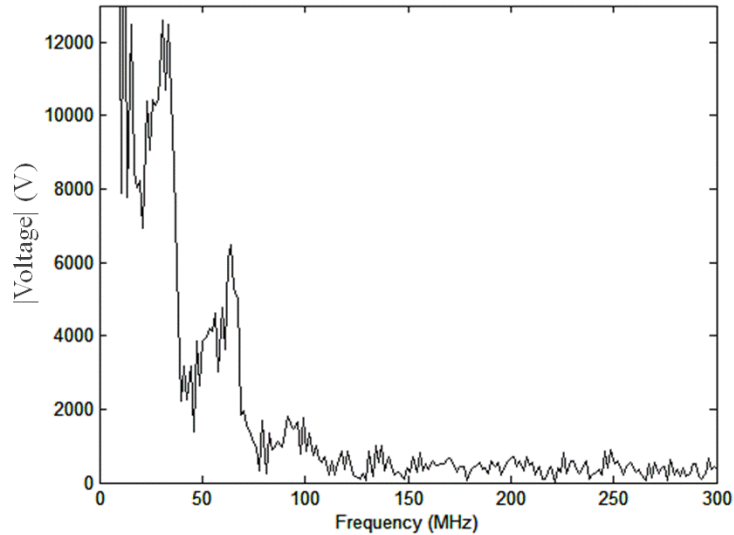


Figure 75. Frequency content of coaxial cylinder load voltage oscillations

6.3 Experiments Results of the Power Conditioning System with FCGs

In April 2007, teams from the University of Missouri-Columbia and Texas Tech University integrated their systems for coordinated tests in Lubbock, TX. A total of five experiments were conducted. All power conditioning components, including the pulse transformer, fuse, high voltage capacitor, low inductance oil switch, and oscillating circuit performed as expected with the exception of restrike in the fuse after the RF burst. The crowbar switch was not used in the coordinated experiments with TTU. However, since the restrike occurred after the low inductance switch closed and the RF load began oscillating, the restrike had little negative effect on the system operation in most tests. Several difficulties with diagnostics were encountered for both groups. Many of the difficulties with diagnostics were a result of operation of the system interfering with and disabling oscilloscopes and video cameras. Some data was lost as a result of the RF interference.

Figure 76 and Figure 77 show the layout of the experiments. The red tank in the center of Figure 76 housed the FCG and contained the explosion. The electrical output of the FCG was fed through a side port on the explosives tank and drove the power conditioning components located in the gray container. The receiving antennas are seen in the right foreground.



Figure 76. The power conditioning system, explosives chamber, and receiving antennas

Figure 77 shows the power conditioning components adjacent to the port on the explosives chamber. The exploding wire fuse is shown packed in fine glass beads and placed adjacent to the oil bath. One end of the radiating dipole antenna can be seen extending from the center of the oil bath.



Figure 77. A fuse, packed in sand, is positioned next to the oil bath

6.3.1 Experimental Results with an FCG and Non-Radiating Load

The first three experiments conducted with TTU FCGs used a resistive load of 369Ω in parallel with the secondary capacitance to replace an antenna and provide a resistive voltage divider. A fuse of 27 40 gauge silver-plated copper wires was implemented as the opening switch. The fuse wires were approximately 30 cm long. A transformer with a $1 \mu\text{H}$ primary self-inductance, $8.25 \mu\text{H}$ secondary inductance, and coupling factor of 0.8 was implemented in the tests. The tri-plate capacitor of 275 pF was used as the RF system capacitor. The oil spark gap was set to approximately 1.25 mm.

Figure 78 displays the voltage measured from the resistive voltage divider across the low inductance capacitor during the time of fuse operation. Prior to the fuse opening, the capacitor is charged to -50 kV as current builds in the transformer primary. As the fuse opens, the capacitor is charged to a peak of about $+145 \text{ kV}$. As will be seen in the current graphs below, there is evidence of a decrease in current interruption due to very high voltages across the fuse. As a result, the voltage on the capacitor decreased to about 50 kV before the oil gap closed and the capacitor began to oscillate. Since the energy stored in the capacitor was reduced as the voltage fell from 145 kV to 50 kV , it is believed that most of the energy stored in the capacitor was dissipated in the first voltage spike, which peaked at less than -200 kV . The remaining oscillations of lesser magnitude may then be the result of energy being coupled from the primary circuit to the secondary circuit due to continued current flow through the primary winding of the transformer.

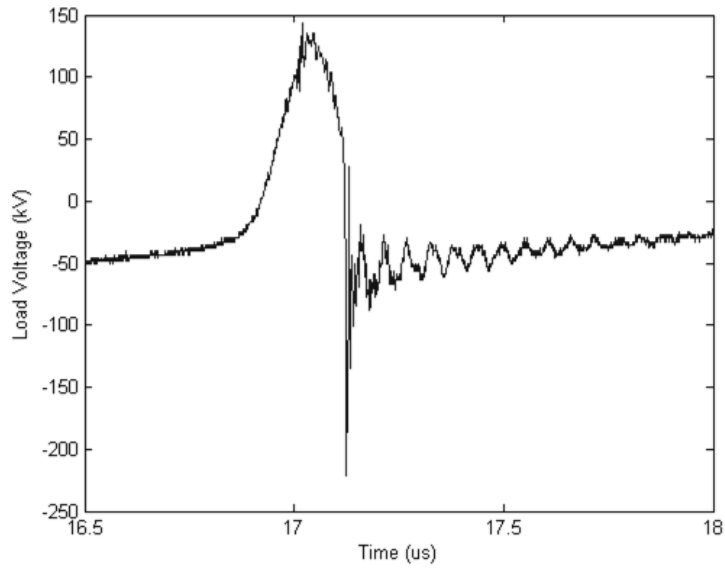


Figure 78. Load voltage during fuse operation

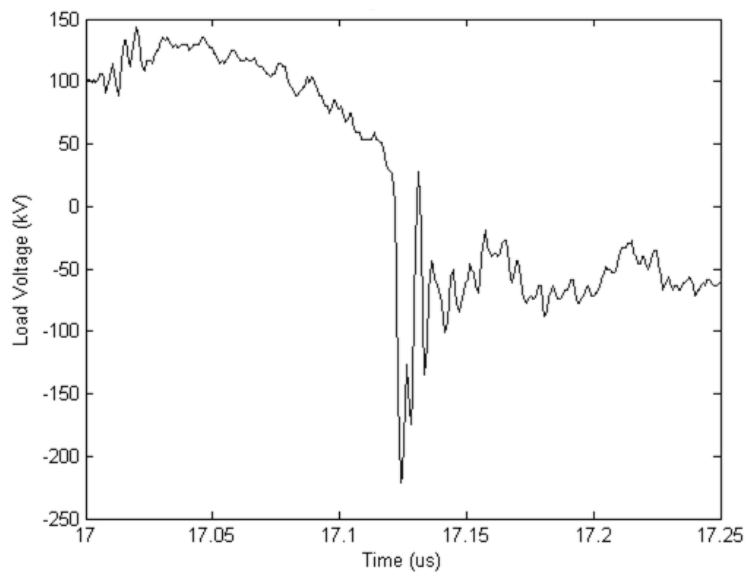


Figure 79. Detailed view of capacitor voltage at time of oil gap closure

The peak power of the main spike reached 120 MW. The frequency of the load voltage after FCG operation had a wide band of significant content beyond 200 MHz, as shown in Figure 80.

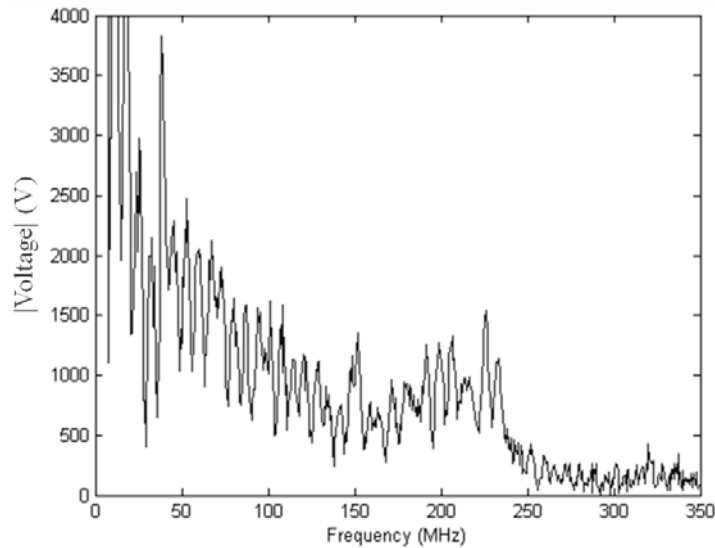


Figure 80. Frequency content of capacitor voltage

Figure 81 shows the current through the transformer primary and fuse. The fuse resistance initially increased very rapidly, reducing the current from 42kA to 20kA. However, as Figure 82 demonstrates, the voltage across the fuse rose to voltages much higher than anticipated for the design. The fuse voltage peak was greater than 500 kV. The excessively high voltage caused the fuse resistance to drop just before the oil switch closed. The oscillations of the primary current and fuse voltage that followed correspond to the extra energy coupled to the secondary due to the decaying primary current.

There is evidence that the fuse opened before the current rise of the FCG was complete. The resulting stray inductance in the primary circuit explains why the voltage across the fuse reached such high levels, resulting in restrike. If there is still a substantial inductance in the FCG due to the action limit being reached before the FCG inductance has been fully removed from the circuit, the fuse will have to hold off the extra voltage that appears across the additional inductance during current interruption. Given the evidence of the very high voltages generated across the fuse in this case, it is advantageous to implement a crowbar switch, as described previously, not only with the

FCG simulator but also with an FCG. The crowbar could short the FCG inductance and minimize the voltage across the fuse.

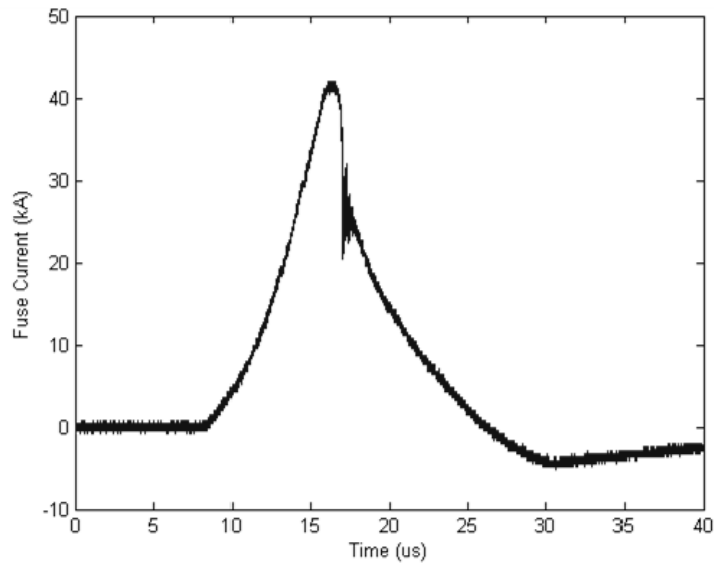


Figure 81. Transformer primary current

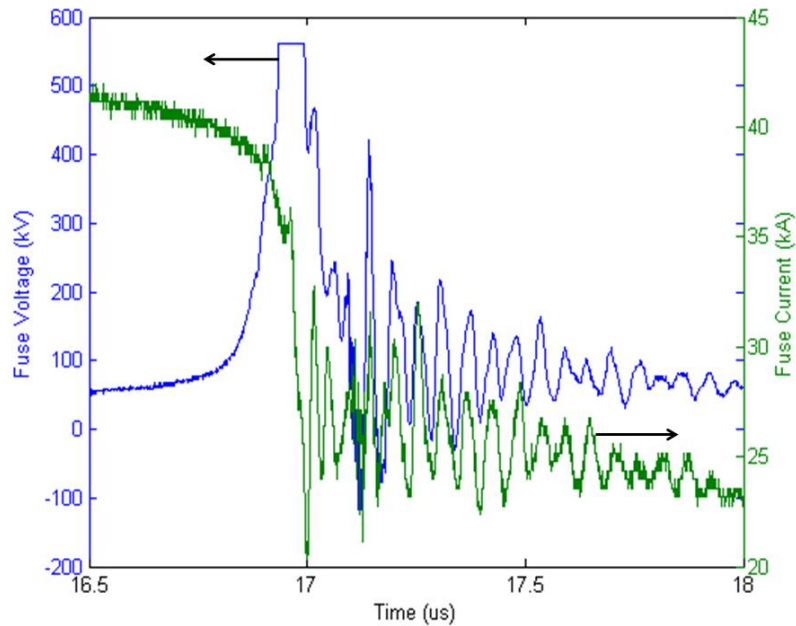


Figure 82. Detailed view of fuse current and voltage

6.3.2 Experimental Results with an FCG and Dipole Antenna

For experiments with a radiating antenna, a dipole was added to the system in parallel with the secondary capacitance. The dipole antenna was constructed from copper pipe

and tuned to radiate at 60 MHz. A previous experiment had disabled the oscilloscope used for data collection of the power conditioning diagnostics, resulting in a loss of data. To prevent the RF interference, the oscilloscope was moved to a screen room for the antenna experiments. However, the distance to the screen room was greater than the length of the cables to which the North Star High Voltage PVM 6 and Tektronix P6015A high voltage probes were calibrated. Therefore, the load voltage diagnostics were replaced by a capacitive probe provided by TTU. To reduce noise in the long coaxial cables used with the capacitive probe and current monitor, the cables were wrapped around ferrites both near the probes and at the entrance to the screen room. With the dipole antenna and capacitive voltage probe in place, the resistive dummy load, which had also served as a voltage divider, was removed from the system.

From the observed fuse restrike in experiments with a dummy load, it was evident that the FCG could provide a higher current and greater energy than previously expected. Due to the higher currents than expected, the action limit of the fuse was reached before FCG operation had completed. Therefore, for experiments with a dipole antenna, the number of fuse wires was increased to 36. By increasing the number of fuse wires and, thus, the value of the action limit, the FCG operated for a longer time before the action limit was reached. The longer operating time for the FCG results in a lower FCG inductance and a higher primary current before the fuse resistance begins its rapid increase. With the higher peak primary current, the energy available for transfer to the secondary was increased. Therefore, the oil gap spacing was increased to 2.5 mm, twice the gap spacing in the resistive load experiment previously discussed. The increased gap spacing would

allow the secondary capacitance to be charged to a much higher voltage before the switch closed.

Figure 83 displays the current waveform through the fuse and transformer primary. Although it shows a peak current of about 72 kA, the peak current is greater than the rated limits of the P101, and the actual peak is likely lower than that measured [6]. Again there is evidence of current conduction through the transformer primary and fuse after operation of the oscillating circuit, indicating a restrike event. The restrike is due to the extremely high fuse voltages resulting from the remaining inductance of the FCG as the current is interrupted.

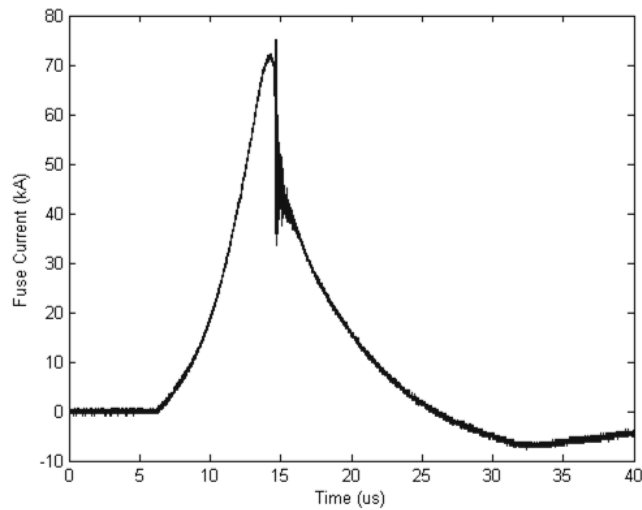


Figure 83. Transformer primary and fuse current

Figure 84 shows the load voltage obtained by the capacitive probe at the time of fuse opening. Much of the noise was removed by the addition of the ferrites around the coaxial cables. As all previous tests at MU and TTU had a much smaller oil gap spacing, the peak capacitor voltage levels obtained in this test were much higher than those previously recorded. Also, the load resistor that was previously in parallel with the capacitor was removed for the dipole antenna tests. The several tens of joules normally

dissipated by a resistive dummy load while the capacitor is charged, as shown in Figure 65, were no longer wasted. The capacitor was charged until about $t = 14.6 \mu\text{s}$. Although the peak voltage values were cutoff by the oscilloscope, Figure 84 shows that the peak capacitor voltage reached greater than 700kV.

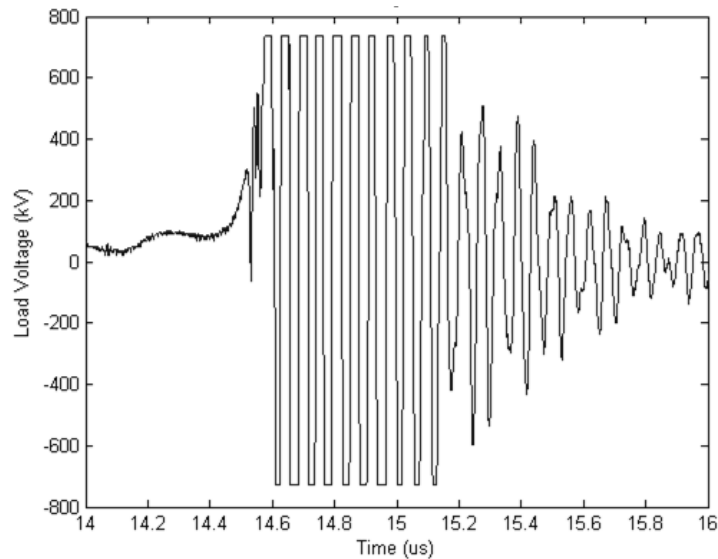


Figure 84. Load voltage from capacitive probe

Although the peak secondary voltages were higher than anticipated, they are under the theoretical peak charging voltages. Figure 86 displays PSpice waveforms of simulations of the secondary voltage which demonstrate that currents of the magnitude observed in this experiment can theoretically charge the secondary to greater than 700 kV. The simulated peak primary currents were 65 kA and 70 kA after a 10 μs generator operating time. The secondary capacitance in the simulation was 275 pF. The transformer primary self-inductance, secondary self-inductance, and coupling ratio were 1 μH , 9 μH , and 0.8, respectively. The waveform modeling the fuse resistance behavior is shown in Figure 85.

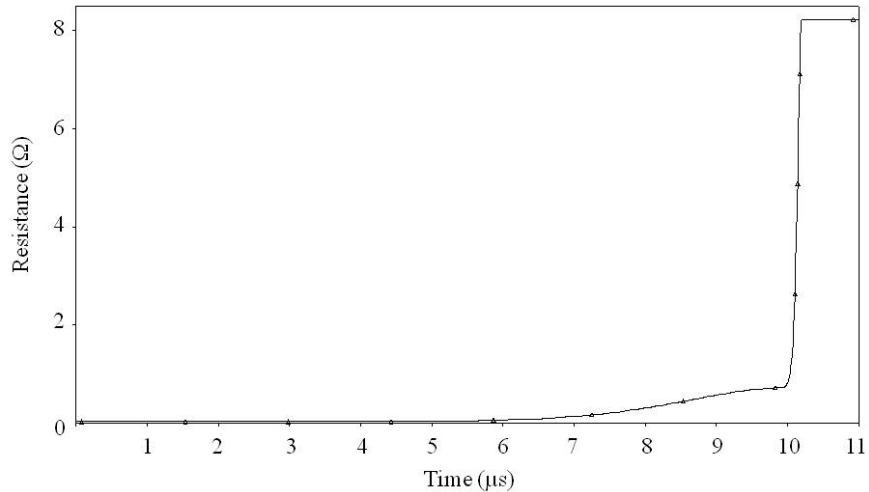


Figure 85. Modeled fuse resistance for analysis of peak charging voltage

Since these simulations are designed to predict the peak possible charging voltages, the low inductance switch was omitted. Figure 86 confirms that for primary currents of 65 kA and 70 kA, the peak charging voltage is greater than 700 kV. Additionally, if the stray inductance is non-negligible, as evidence of restriking suggests, the inductively-stored energy is even greater, and the peak charging voltage could be increased further.

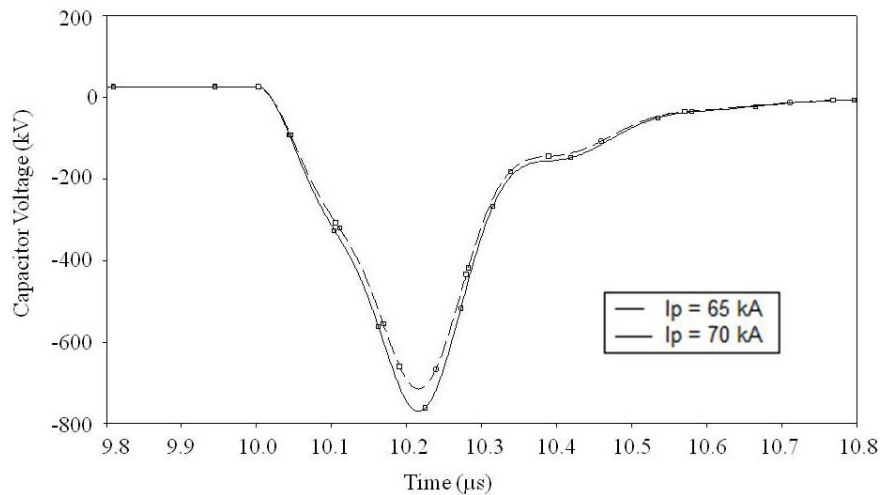


Figure 86. Simulated peak charging voltage

Figure 87 shows plots of the load voltage and primary current after the action limit of the fuse has been reached. The close correspondence between the oscillations of both signals suggests that the oscillations of the primary current are due to coupling from the secondary circuit.

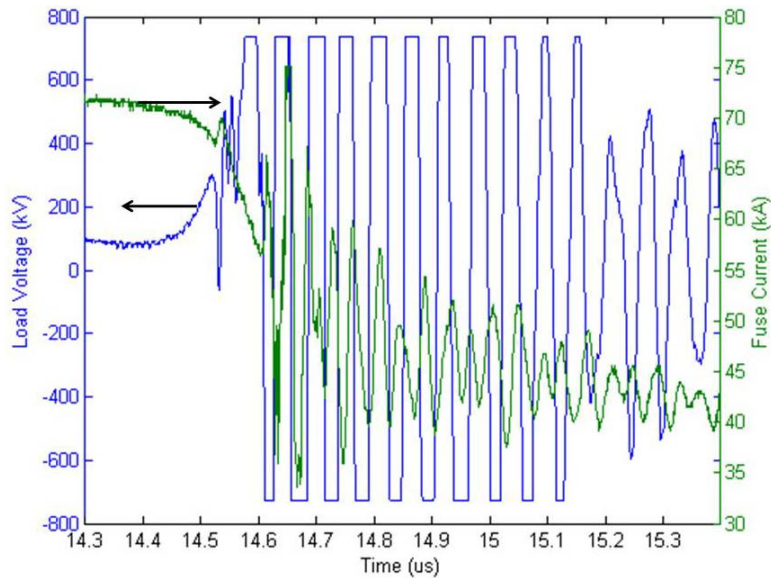


Figure 87. Load voltage and fuse current

Receiving antennas at a distance of about 5.5 m from the power conditioning equipment showed field levels in excess of 6 kV/m peak-to-peak. The fast Fourier transform of these electric field readings confirms that high fields were radiated at 60 MHz and 120 MHz. Much of the additional frequency content observed with the tri-plate RF source was also present up to 250 MHz [8].

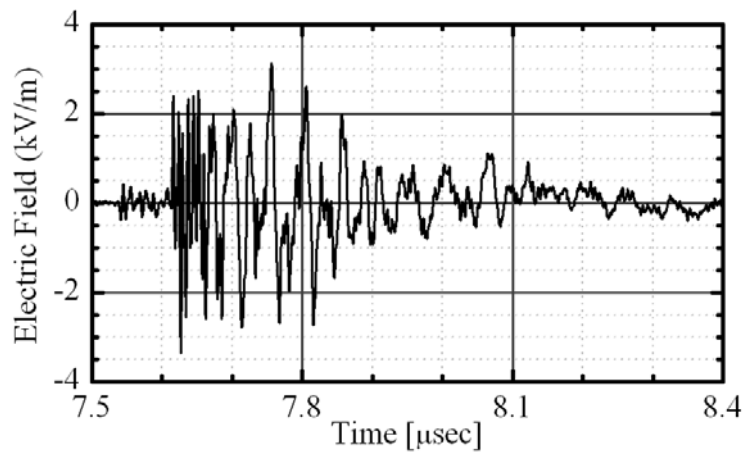


Figure 88. Electric field measured by receiving antenna 5.5 m from dipole antenna [8]

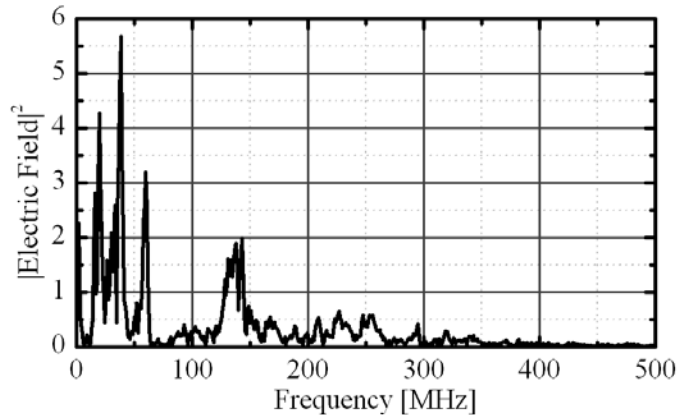


Figure 89. Frequency content of the received signal [8]

The coordinated tests demonstrated a successful full-system integration. Although RF interference with the diagnostics resulted in several measurements being lost, the goal of radiating high fields that could be measured at a distance was achieved. The addition of the crowbar switch to the power conditioning system when operating with FCGs should reduce the probability of restrike and increase the energy transfer to the secondary in future systems.

References for Chapter 6

- [1] "OrCAD PSpice," 9.10.157 CIS ed Beaverton, OR: OrCAD, Inc., 1999.
- [2] Tektronix (Access Confirmed Nov. 2008). Digital Phosphor Oscilloscopes: TDS 5000B Series. [Online]. Available: <http://www.tektronix.com/tds5000b>.
- [3] R.E. Beverly III and Associates (Access Confirmed Nov. 2008). Application Notes for Aqueous Electrolyte Resistors. [Online]. Available: http://www.reb3.com/pdf/r_appl.pdf.
- [4] North Star High Voltage (Access Confirmed Nov. 2008). PVM series portable high voltage probes to 60 kV DC. [Online]. Available: <http://www.highvoltageprobes.com/PDF/Vmonad.pdf>.
- [5] Tektronix (Access Confirmed Nov. 2008). Passive High Voltage Probes. [Online]. Available: http://www2.tek.com/cmsreplive/psrep/13471/56W_10262_2_2008.05.21.08.16.14_13471_EN.pdf.
- [6] Pearson Electronics Inc. (Access Confirmed Nov. 2008). Pearson Current Monitor Model 101. [Online]. Available: <http://www.pearsonelectronics.com/datasheets/standard-ct/101.pdf>.

- [7] D. V. Giri and F. M. Tesche, "Classification of intentional electromagnetic environments (IEME)," *IEEE Trans. on Electromagnetic Compatibility*, vol. 46, pp. 322-328, 2004.
- [8] T. Holt, A. Young, M. Elsayed, A. Neuber, M. Kristianssen, K. O'Connor, and R. Curry, "Investigation of an FCG and pulse transformer based power conditioning system," in *The 16th IEEE International Pulsed Power Conference*, Albuquerque, NM, 2007.

Chapter 7: Summary and Conclusions

Power conditioning and RF systems have been developed to provide a compact and portable source of high power RF signals. A pulse transformer, exploding wire fuse, and crowbar switch were developed as power conditioning components that can drive high power RF sources. Three geometries of a high power RF source were investigated as an alternative to other HPM sources. A high power test stand that can drive the power conditioning system with a signal approximating that of a flux compression generator was built and repeatedly tested to provide a non-destructive and inexpensive experimental alternative to explosive sources. This chapter provides a brief summary of system operation, the power conditioning components, and the project's main accomplishments.

The system operates in three stages. First, the FCG or FCG simulator drives an increasing current through the transformer primary winding and fuse. The majority of the energy from the generator is inductively-stored in the transformer. Also, some energy is dissipated in the fuse to heat it to the beginning of vaporization. At the end of FCG or FCG simulator operation, the inductance of the generator is a minimum, ideally zero. The primary current has reached its peak value at this time, and the fuse has reached the action limit. In the second stage of operation, the resistance of the fuse rapidly rises, and energy is transferred from the transformer to the secondary circuit, charging the secondary capacitance to high voltage. The end of the second stage of operation coincides with the closure of the secondary switch, which shorts the capacitor through a shunt inductance. Ideally, the secondary switch closes when the primary current has reached zero amps. The secondary voltage reaches its peak value, and the maximum amount of

energy is stored in the capacitance. The third stage of operation generates an RF signal as energy oscillates between the secondary capacitance and shunt inductance. A load in parallel with the secondary capacitance, which could be a radiating antenna, dissipates or radiates the high power RF signal.

The FCG simulator is capable of delivering a high current to the power conditioning and RF systems for experiments that closely match those with explosive generators. The FCG simulator produces a current pulse with an increasing rate of current rise in time, similar to that of an FCG. The risetime of the current pulse is typically 6-12 μs , and the peak currents reach approximately 60 kA for a 1 μH load and from 20 kA to over 40 kA with a full power conditioning system as the load. The generator allows inexpensive, repeatable, and non-destructive testing of power conditioning components and RF sources with no components from the FCG simulator requiring replacement between experiments.

The pulse transformer stores the energy from the FCG or FCG simulator and provides a voltage step-up to the RF source. The transformer was constructed in a spiral-strip geometry, which provides a compact package for energy storage and transfer. A non-magnetic core allows compatibility with the relatively long applied voltage pulse from the FCG. The flux coupling, enabled by the overlapping geometry of the transformer strips, results in reduced leakage inductance and fast energy transfer to the secondary circuit. The transformers had a 1 μH primary self-inductance, a secondary self-inductance between 8 μH and 9 μH , and a coupling factor of 0.8. The transformers were built to a diameter of 15.24 cm and a length of 17.78 cm. The windings are impregnated with oil, and the transformer is operated while submerged in an oil bath. The transformers have

repeatedly been tested with primary currents of 20-40 kA and secondary voltages greater than 100 kV. A peak secondary voltage of greater than 700 kV across the transformer secondary has been recorded without failure. Modeling the circuit with variable transformer parameters enabled the determination of the optimal turn ratio of the transformer.

The exploding wire fuse utilizes a rapidly increasing resistance to act as an opening switch and transfer energy to the load after operation of the FCG. The fuse consisted of an array of angled, silver-plated copper wires packed in fine glass beads. The fuse initially presented a low impedance to the energy source. Upon vaporization of the fuse wires at the end of generator operation, the fuse resistance rapidly increases in a time on the order of nanoseconds to tens of nanoseconds. The fuse used in this investigation consistently interrupted currents from 20 kA to over 40 kA in 150-400 ns. The fuse, after being packaged, was 15.24 cm in diameter and approximately 31 cm long. Numerical modeling of the fuse resistance in the full system circuit was developed. While investigating the use of the exploding wire fuse, problems with the established standard for fuse length design were discovered. Although the convention was to assume that longer fuses with greater initial resistances resulted in higher final resistance, numerical modeling of the circuit and fuse equations confirmed that shorter fuses actually rise to higher resistance than longer fuses in the same system. A flawed basis for the derivation of the fuse length prompted a new proposal for the optimal fuse length. The newly developed equations for fuse length design calculate the minimum length of the fuse, resulting in the highest fuse resistance, based upon the specific energy dissipated in the fuse. The length of the fuse in many high voltage systems will likely need to be longer

than the optimal minimum fuse length to prevent arc breakdown of the fuse and restrike in the system, but the new design technique provides the length for optimum fuse performance.

In early full system experiments, higher voltages than those predicted appeared across the fuse when there was stray inductance in the primary circuit. The stray inductance was in the circuit of the FCG simulator or in the stator of the FCG when the coil had not fully been shorted. The high voltages generated across the stray inductance could result in arc breakdown of the fuse and degradation of the system performance. A crowbar switch was implemented to short the stray inductance if it were high enough to substantially increase the voltage across the fuse. Numerical modeling was provided for the analysis of the negative effects of stray inductance on system performance. The analysis revealed that relatively small stray inductances can result in significantly higher fuse voltages, possibly leading to fuse restrike. Also, when stray inductance is non-negligible, the efficiency of energy delivery to the load can be lowered significantly. The analysis shows that stray inductance is a critical factor in fuse performance and must be minimized. Implementation of a crowbar switch ensures any remaining stray inductance has a minimal negative effect.

The RF load was developed on the foundation of using compact high voltage capacitors and the shunt inductance of a closing switch to form a high power oscillator. The most critical design of the RF load was high voltage holdoff of hundreds of kilovolts in a compact capacitor geometry. The tri-plate capacitor provided a proof of principle for the RF load. The 275 pF capacitor was repeatedly tested at voltages greater than 180 kV, and one test recorded capacitor voltages of greater than 700 kV. The frequency of RF

oscillations for the tri-plate capacitor had a wide content of several 10s of MHz up to 250 MHz. A rolled compact cylindrical capacitor used similar design and construction techniques to the spiral-strip transformer. The spiral-strip capacitor had a capacitance in oil of 730 pF in a package with a 15.24 cm diameter and 30.5 cm length. The spiral-strip capacitor was pulse charged up to 190 kV, and the oscillation frequencies had significant content in the 30-75 MHz range with additional content around 200 MHz. Finally, the most compact high voltage capacitor was the coaxial cylinder capacitor. It was constructed with insulating pipes with conducting coverings, with an outermost pipe diameter of only 8.26 cm. The capacitor was 30.5 cm long, and the capacitance in oil was 459 pF. The coaxial cylinder capacitor was pulse charged to 180 kV, and the RF oscillations had significant content from 40-70 MHz.

Extensive experimental testing was conducted of the integrated system with power conditioning components and the RF source. Tests of the full system with a tri-plate RF system on the FCG simulator resulted in peak charging voltages of 200 kV, corresponding to 130 MW RF power. The frequency content extended up to 250 MHz. Further testing of the tri-plate system recorded load capacitor voltages corresponding to more than 250 MW. Experiments with the cylindrical spiral-strip RF system produced a peak charging voltage of 190 kV, a peak RF power of 90 MW, and significant frequency content from 30 to 75 MHz and around 200 MHz. Additionally, experiments with the spiral-strip RF system were driven by lower energies, thus demonstrating the system compatibility with smaller energy sources. Two failure modes were observed in separate tests when the oil spark gap does not close and when the capacitor dielectric breaks down. Interestingly, both of these failure situations still form an oscillating circuit that

produces high frequency load voltage oscillations, and both could be acceptable modes of operation in single shot devices. Finally, the coaxial cylinder RF system was tested. In this very compact geometry, a peak charging voltage of 180 kV was reached, corresponding to a load power of 70 MW. Significant load voltage oscillations were observed in the band from 40 MHz to 70 MHz. Experiments with FCGs were conducted with TTU using the MU power conditioning system and tri-plate RF system. Tests with a resistive load in parallel with the RF system resulted in a peak voltage spike of 200 kV, corresponding to 120 MW. Experiments were also conducted with a dipole antenna in place of the dummy resistive load. Peak charging voltages greater than 700 kV were recorded, and an electric field of 6 kV/m peak-to-peak was recorded at 5.5 m from the test stand. The received frequency content had frequency bands extending up to 250 MHz.

Finally, in the appendices, circuit equations are derived and numerical techniques are detailed to simulate the circuit behavior with the dynamic resistance of the fuse. Computer codes were developed that allow for simulations of the full system with varied circuit or fuse parameters, making complicated system analyses possible and improving insight into system operation.

The power conditioning and RF components investigated in this study have proven to be viable options for application with flux compression generators as a compact high power RF source. Additionally, the power conditioning system has potential for application with several other high power RF and HPM systems. The future study of this system could further reduce the size of the power conditioning and RF components, including the reduction of the fuse length towards the optimal minimum. Simulations

show the power conditioning system is capable of charging the secondary capacitor to greater than 1 MV if the capacitor were able to withstand voltages of that magnitude. Improvements in the high voltage holdoff of the compact capacitors could allow scaling of the system to peak powers of several hundred megawatts.

APPENDIX A: Equations for Dynamic Resistance Modeling

For the numerical analyses implemented throughout this thesis, the circuit equations for the FCG, power conditioning system, and loads are required. The equations are derived in this appendix for the two stages of operation with a resistive load and one stage of operation for the RF source. The resistive load approximates the impedance of an HPM source. Description of the implementation of these equations for a dynamic fuse resistance is included in Appendix B.

A.1 Power Conditioning System with a Resistive Load

A.1.1 Resistive Load During FCG Operation

Figure 90 shows the equivalent circuit for s-domain analysis of the power conditioning circuit with a resistive load during FCG operation. The current from the FCG or FCG simulator is represented as a current source. There are no initial currents through the inductors. The transformer is represented by its T-equivalent, and the secondary components are referred to the primary [1]. Equations A1-A4 give the relationships of the circuit inductors.

$$L_{mp} = kL_p \quad \text{A1.}$$

The symbol L_p [H] is the primary self-inductance, and the symbol L_{mp} [H] is the magnetizing inductance referred to the primary. The coupling factor is represented by the symbol k . The primary leakage inductance and secondary leakage inductance are represented respectfully as L_{lp} [H] and L_{ls} [H].

$$L_{lp} = L_p(1 - k) = \frac{L_s(1 - k)}{n^2} \quad \text{A2.}$$

$$L_{ls} = n^2 L_p (1 - k) = L_s (1 - k) \quad \text{A3.}$$

$$n = \sqrt{\frac{L_s}{L_p}} \quad \text{A4.}$$

The turn ratio is denoted by n , and the symbol L_s [H] is the secondary self-inductance.

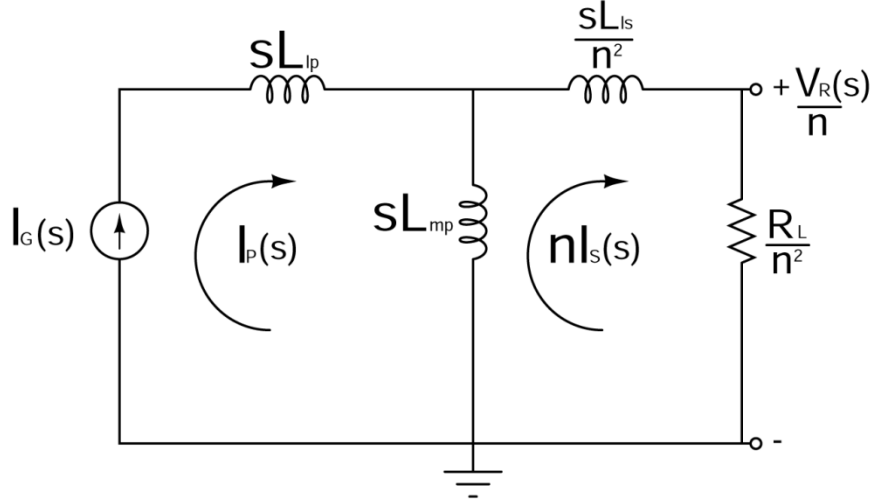


Figure 90. Equivalent s-domain circuit for an HPM load during FCG operation

The secondary circuit current, $nI_s(s)$ [A], can be written in terms of the current input from the FCG based on impedance current division.

$$nI_s(s) = I_p(s) \left[\frac{sL_{mp}}{sL_{mp} + \frac{sL_{ls}}{n^2} + \frac{R_L}{n^2}} \right] \quad \text{A5.}$$

After factoring and arranging terms, the equation simplifies to the form of equation A6.

$$nI_s(s) = I_p(s) \left(\frac{L_{mp}}{L_{mp} + \frac{L_{ls}}{n^2}} \right) \left[\frac{s}{s + \frac{R_L}{n^2 L_{mp} + L_{ls}}} \right] \quad \text{A6.}$$

All of the inductor terms can be put in terms of L_s by using equations A1-A4.

$$nI_s(s) = I_p(s) k \left[\frac{s}{s + \frac{R_L}{L_s}} \right] \quad \text{A7.}$$

The expected input from the FCG or FCG simulator is nearly exponential. An equation developed from experimental data for numerical modeling of FCGs takes the form of equation (42), as presented in Chapter 4 [2]. A generator exponential constant, c_g [s^{-1}], is defined here as ε/t_r . Transforming equation (42) into the s -domain requires taking the Laplace transform, and the inverse Laplace transform is required for later conversions. Several useful inverse transform techniques can be found in [3]. The inverse transform can also be found with an internet application [4]. Taking the Laplace transform of equation (42) gives $I_p(s)$ in the s -domain.

$$I_p(s) = \frac{I_f}{e^1 - 1} \left(\frac{1}{(s - c_g)} - \frac{1}{s} \right) \quad \text{A8.}$$

Substituting equation A8 into equation A7 results in a final equation for $I_s(s)$.

$$I_s(s) = \frac{I_f k}{(e^1 - 1)n} \left[\frac{s}{(s - c_g) \left(s + \frac{R_L}{L_s} \right)} - \frac{1}{\left(s + \frac{R_L}{L_s} \right)} \right] \quad \text{A9.}$$

The inverse Laplace transform can be applied to equation A9 to solve for $i_s(t)$ [A].

$$i_s(t) = \frac{I_f k}{(e^1 - 1)n} \left[\frac{1}{\left(c_g + \frac{R_L}{L_s} \right)} \left(c_g e^{c_g t} + \frac{R_L}{L_s} e^{-\frac{R_L}{L_s} t} \right) - e^{-\frac{R_L}{L_s} t} \right] \quad \text{A10.}$$

Equation A10 can be used to predict the current in the load during FCG operation for an exponential current input from the FCG. Since the load is resistive, the load voltage can simply be calculated as the product of the secondary current and the load resistance.

Equations A10 and A11 apply for $0 \leq t < t_r$, where t_r [s] is the runtime of the FCG.

$$v_r(t) = \frac{I_f k R_L}{(e^1 - 1)n} \left[\frac{1}{\left(c_g + \frac{R_L}{L_s} \right)} \left(c_g e^{c_g t} + \frac{R_L}{L_s} e^{-\frac{R_L}{L_s} t} \right) - e^{-\frac{R_L}{L_s} t} \right] \quad \text{A11.}$$

For all the sections in which the primary and secondary currents are derived, the magnetizing current, $i_m(t)$ [A], can be found by the following simple relation.

$$i_m(t) = i_p(t) - ni_s(t) \quad \text{A12.}$$

A.1.2 Resistive Load After FCG Operation

At the completion of the operation of the FCG or FCG simulator, the current source is ideally a short circuit. Figure 91 shows the equivalent circuit for s-domain analysis of the power conditioning circuit with a resistive load after FCG operation. The current source that represented the input from the FCG is now represented simply as a short circuit. The voltage sources account for the initial currents in the inductors, and I_{p0} , I_{m0} , and nI_{s0} represent, respectfully, the currents after generator operation in the primary circuit, magnetizing inductance, and secondary circuit.

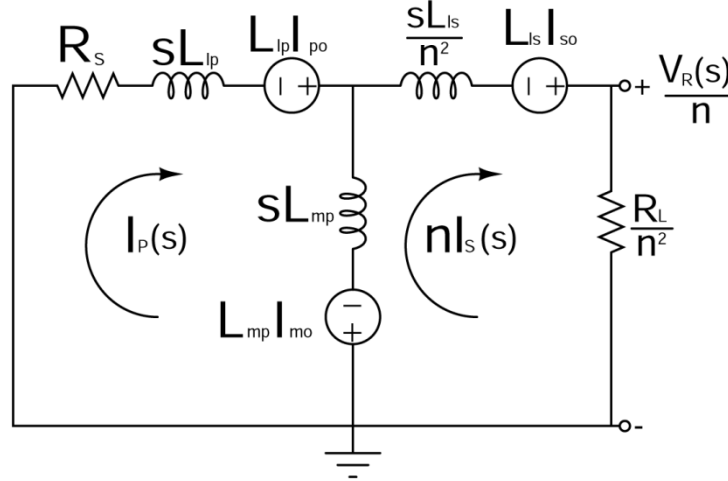


Figure 91. Equivalent s-domain circuit for an HPM load after FCG operation

Implementing the KVL procedure around the outer and right-hand loops results in equations A13 and A14.

$$I_p(s)[R_s + sL_{lp}] - L_{lp}I_{po} + nI_s(s)\left[\frac{sL_{ls}}{n^2} + \frac{R_L}{n^2}\right] - \frac{L_{ls}(nI_{so})}{n^2} = 0 \quad \text{A13.}$$

$$L_{mp}I_{mo} - sI_p(s)L_{mp} + nI_s(s) \left[sL_{mp} + \frac{sL_{ls}}{n^2} + \frac{R_L}{n^2} \right] - \frac{L_{ls}(nI_{so})}{n^2} = 0 \quad A14.$$

Solving equation A14 for $I_p(s)$ and substituting into equation A13 results in equation

A15.

$$\begin{aligned} \frac{I_{mo}R_s}{s} + I_{mo}L_{lp} - I_{po}L_{lp} - \frac{R_L L_{ls} I_{so}}{sn^2 L_{mp}} - \frac{L_{ls} L_{lp} (nI_{so})}{n^2 L_{mp}} - \frac{L_{ls} (nI_{so})}{n^2} \\ + nI_s(s) \left[R_s + sL_{lp} + \frac{R_s L_{ls}}{n^2 L_{mp}} + \frac{sL_{lp} L_{ls}}{n^2 L_{mp}} + \frac{R_L R_s}{sL_{mp} n^2} + \frac{R_L L_{lp}}{n^2 L_{mp}} + \frac{sL_{ls}}{n^2} + \frac{R_L}{n^2} \right] = 0 \end{aligned} \quad A15.$$

Multiplying by s and collecting terms results in equation A16.

$$\begin{aligned} nI_s(s) \left[s^2 \left(L_{lp} + \frac{L_{ls}}{n^2} + \frac{L_{lp} L_{ls}}{n^2 L_{mp}} \right) + s \left(R_s + \frac{R_s L_{ls}}{n^2 L_{mp}} + \frac{R_L L_{lp}}{n^2 L_{mp}} + \frac{R_L}{n^2} \right) + \frac{R_L R_s}{L_{mp} n^2} \right] \\ + s \left(I_{mo} L_{lp} - I_{po} L_{lp} - \frac{L_{ls} L_{lp} (nI_{so})}{n^2 L_{mp}} - \frac{L_{ls} (nI_{so})}{n^2} \right) + I_{mo} R_s - \frac{R_L L_{ls} (nI_{so})}{n^2 L_{mp}} = 0 \end{aligned} \quad A16.$$

Equation A17 is obtained by substituting each inductive term by its equivalent in terms of L_s , multiplying both sides of the equation by $n^2 k L_s$, and simplifying terms.

$$\begin{aligned} nI_s(s) \left[s^2 L_s^2 (1 - k^2) + s(L_s(R_s n^2 + R_L)) + R_L R_s n^2 \right] \\ = s[L_s^2 (1 - k^2)(nI_{so})] - k R_s L_s n^2 \left(I_{po} - \frac{(nI_{so})}{k} \right) \end{aligned} \quad A17.$$

Isolating $I_s(s)$ on the left-hand side of the equation and dividing the top and bottom of the right-hand side by $L_s^2(1-k^2)$ results in equation A18.

$$I_s(s) = \frac{sI_{so} - \frac{kR_s n}{L_s(1-k^2)} \left(I_{po} - \frac{I_{so}(nI_{so})}{k} \right)}{s^2 + s \left(\frac{R_s n^2 + R_L}{L_s(1-k^2)} \right) + \frac{R_L R_s n^2}{L_s^2(1-k^2)}} \quad A18.$$

The denominator of equation A18 can be factored using equations A19-A22.

$$I_s(s) = \frac{sI_{so}}{(s-s_1)(s-s_2)} + \frac{\frac{-kR_s n}{L_s(1-k^2)} \left(I_{po} - \frac{(nI_{so})}{k} \right)}{(s-s_1)(s-s_2)} \quad A19.$$

$$s_1 = -\frac{R_L + n^2 R_s}{2L_s(1-k^2)} (1 + \gamma_1) \quad A20.$$

$$s_2 = -\frac{R_L + n^2 R_s}{2L_s(1 - k^2)}(1 - \gamma_1) \quad \text{A21.}$$

$$\gamma_1 = \sqrt{1 - \frac{4R_L(1 - k^2)}{R_s n^2 \left(1 + \frac{R_L}{n^2 R_s}\right)^2}} \quad \text{A22.}$$

Taking the inverse Laplace transform of equation A18 and collecting terms, equation A23 is arrived at for the secondary load current in the time domain.

$$i_s(t) = \left(\frac{I_{so}(1 + \gamma_1)}{2\gamma_1} + \frac{kR_s n \left(I_{po} - \frac{(nI_{so})}{k} \right)}{(R_L + R_s n^2)\gamma_1} \right) e^{-\frac{R_L + n^2 R_s}{2L_s(1 - k^2)}(1 + \gamma_1)(t - t_r)} - \left(\frac{I_{so}(1 - \gamma_1)}{2\gamma_1} + \frac{kR_s n \left(I_{po} - \frac{(nI_{so})}{k} \right)}{(R_L + R_s n^2)\gamma_1} \right) e^{-\frac{R_L + n^2 R_s}{2L_s(1 - k^2)}(1 - \gamma_1)(t - t_r)} \quad \text{A23.}$$

The derivation of equation A23 was set up such that if I_s , I_p , and R_s are known at a point in time, the derivative of $i_s(t)$ can be taken with $(t - t_r) = 0$ in the above equation. As is described in Appendix B, the process of taking the derivative with the time term equal to zero can be performed at each time step. Although the notation in the following derivatives shows the time term as t_r , the equation for the derivative can be applied at any time step for $t > t_r$. The variables R_s , i_p , i_s , i_m , v_c , γ , and β are shown in the derivatives at their values at t_r . However, this should be interpreted as the notation for the values at any time step and not the values at the end of generator operation. Equation A24 is the result and can be applied at each time step in a numerical computation to determine the change in current for the next time step. The values of s_1 , s_2 , and γ can still be determined by equations A20, A21, and A22, respectively, with the value of R_s at that time step.

$$\begin{aligned} \frac{d(i_s(t_r))}{dt} = & s_1(t_r) \left(\frac{i_s(t_r)(1 + \gamma_1(t_r))}{2\gamma_1(t_r)} + \frac{kR_s(t_r)n \left(i_p(t_r) - \frac{(ni_s(t_r))}{k} \right)}{(R_L + R_s(t_r)n^2)\gamma_1(t_r)} \right) \\ & - s_2(t_r) \left(\frac{i_s(t_r)(1 - \gamma_1(t_r))}{2\gamma_1(t_r)} + \frac{kR_s(t_r)n \left(i_p(t_r) - \frac{(ni_s(t_r))}{k} \right)}{(R_L + R_s(t_r)n^2)\gamma_1(t_r)} \right) \end{aligned} \quad \text{A24.}$$

The load voltage is a desired parameter and is simply the secondary current multiplied by the load resistance.

$$\begin{aligned} v_r(t) = R_L \left[\left(\frac{I_{s0}(1 + \gamma_1)}{2\gamma_1} + \frac{kR_s n \left(I_{p0} - \frac{(nI_{s0})}{k} \right)}{(R_L + R_s n^2)\gamma_1} \right) e^{-\frac{R_L + n^2 R_s}{2L_s(1-k^2)}(1+\gamma_1)(t-t_r)} \right. \\ \left. - \left(\frac{I_{s0}(1 - \gamma_1)}{2\gamma_1} + \frac{kR_s n \left(I_{p0} - \frac{(nI_{s0})}{k} \right)}{(R_L + R_s n^2)\gamma_1} \right) e^{-\frac{R_L + n^2 R_s}{2L_s(1-k^2)}(1-\gamma_1)(t-t_r)} \right] \end{aligned} \quad \text{A25.}$$

Again, the derivative can be taken such that the current and resistance values at a given time can be used to calculate the change in load voltage for the next time step in a numerical analysis.

$$\begin{aligned} \frac{d(v(t_r))}{dt} = R_L \left[s_1(t_r) \left(\frac{i_s(t_r)(1 + \gamma_1(t_r))}{2\gamma_1(t_r)} + \frac{kR_s(t_r)n \left(i_p(t_r) - \frac{(ni_s(t_r))}{k} \right)}{(R_L + R_s(t_r)n^2)\gamma_1(t_r)} \right) \right. \\ \left. - s_2(t_r) \left(\frac{i_s(t_r)(1 - \gamma_1(t_r))}{2\gamma_1(t_r)} + \frac{kR_s(t_r)n \left(i_p(t_r) - \frac{(ni_s(t_r))}{k} \right)}{(R_L + R_s(t_r)n^2)\gamma_1(t_r)} \right) \right] \end{aligned} \quad \text{A26.}$$

A beneficial simplifying assumption is to consider I_{s0} to be negligibly small. I_{s0} is zero for the case in which a peaking switch is placed at the output to the load. Neglecting I_{s0} simplifies equations A23 and A25.

$$i_s(t) = \left(\frac{kR_s n I_{p0}}{(R_L + R_s n^2)\gamma_1} \right) \left(e^{-\frac{R_L + n^2 R_s}{2L_s(1-k^2)}(1+\gamma_1)(t-t_r)} - e^{-\frac{R_L + n^2 R_s}{2L_s(1-k^2)}(1-\gamma_1)(t-t_r)} \right) \quad \text{A27.}$$

$$v_r(t) = \left(\frac{kR_s R_L n I_{po}}{(R_L + R_s n^2) \gamma_1} \right) \left(e^{-\frac{R_L + n^2 R_s}{2L_s(1-k^2)}(1+\gamma_1)(t-t_r)} - e^{-\frac{R_L + n^2 R_s}{2L_s(1-k^2)}(1-\gamma_1)(t-t_r)} \right) \quad \text{A28.}$$

Equations A27 and A28 are mathematically equivalent to those discussed by Reinovsky [5]. These equations apply for the load current and voltage after FCG operation, $t > t_r$. The derivatives of equations A27 and A28 can then be taken to obtain the equations to calculate the change in secondary current and load voltage at small time steps in a numerical analysis.

$$\frac{d(i_s(t_r))}{dt} = \left(\frac{kR_s(t_r) n i_p(t_r)}{(R_L + R_s(t_r) n^2) \gamma_1(t_r)} \right) (s_1(t_r) - s_2(t_r)) \quad \text{A29.}$$

$$\frac{d(v_r(t_r))}{dt} = \left(\frac{kR_s(t_r) R_L n i_p(t_r)}{(R_L + R_s(t_r) n^2) \gamma_1(t_r)} \right) (s_1(t_r) - s_2(t_r)) \quad \text{A30.}$$

It is also useful to monitor the primary current after the FCG runtime. To predict the behavior of the primary current, equations A13 and A14 can be combined to isolate $I_p(s)$. Combining equations, multiplying both sides by s , and collection terms of the same order results in equation A31.

$$\begin{aligned} I_p(s) & \left[s^2 \left(L_{lp} + \frac{L_{ls} L_{lp}}{n^2 L_{mp}} + \frac{L_{ls}}{n^2} \right) + s \left(R_s + \frac{R_s L_{ls}}{n^2 L_{mp}} + \frac{R_L L_{lp}}{n^2 L_{mp}} + \frac{R_L}{n^2} \right) + \frac{R_L R_s}{n^2 L_{mp}} \right] \\ & = s \left(I_{po} L_{lp} + \frac{L_{ls} I_{so}}{n^2} + \frac{L_{ls} I_{po} L_{lp}}{n^2 L_{mp}} + \frac{L_{ls} I_{mo}}{n^2} \right) + \frac{R_L L_{lp} I_{po}}{n^2 L_{mp}} + \frac{R_L I_{mo}}{n^2} \end{aligned} \quad \text{A31.}$$

Equations A1-A4 are used to put all transformer terms in relation to L_s . The resulting equation is then multiplied by $kL_s n^2$, and common terms are collected to result in equation A32.

$$I_p(s) = \frac{s I_{po} + \frac{R_L (I_{po} (1-k) + k I_{mo})}{L_s (1-k^2)}}{s^2 + s \left(\frac{R_s n^2 + R_L}{L_s (1-k^2)} \right) + \frac{R_L R_s n^2}{L_s^2 (1-k^2)}} \quad \text{A32.}$$

Taking the inverse Laplace transform of equation A32 and simplifying provides an equation for the time-domain primary current after generator operation.

$$i_p(t) = \frac{1}{2\gamma_1} \left[\left(I_{po}(1 + \gamma_1) + \frac{2R_L(I_{po}(1 - k) + kI_{mo})}{R_s n^2 + R_L} \right) e^{s_1(t-t_r)} - \left(I_{po}(1 - \gamma_1) + \frac{2R_L(I_{po}(1 - k) + kI_{mo})}{R_s n^2 + R_L} \right) e^{s_2(t-t_r)} \right] \quad \text{A33.}$$

Taking the derivative of equation A33 at any point with known current and resistance values can give the change in primary current for a small time step.

$$\frac{d(i_p(t_r))}{dt} = \frac{1}{2\gamma_1(t_r)} \left[s_1(t_r) \left(i_p(t_r)(1 + \gamma_1(t_r)) + \frac{2R_L(i_p(t_r)(1 - k) + ki_m(t_r))}{R_s(t_r)n^2 + R_L} \right) - s_2(t_r) \left(i_p(t_r)(1 - \gamma_1(t_r)) + \frac{2R_L(i_p(t_r)(1 - k) + ki_m(t_r))}{R_s(t_r)n^2 + R_L} \right) \right] \quad \text{A34.}$$

Assuming again that I_{s0} is negligibly small or zero, as in the case when there is a load peaking switch, equation A33 simplifies to equation A35, and equation A34 becomes equation A36.

$$i_p(t) = \frac{1}{2\gamma_1(R_s n^2 + R_L)} \left[(I_{po}(1 + \gamma_1)(R_s n^2 + R_L) + 2R_L I_{po}) e^{s_1(t-t_r)} - (I_{po}(1 - \gamma_1)(R_s n^2 + R_L) + 2R_L I_{po}) e^{s_2(t-t_r)} \right] \quad \text{A35.}$$

$$\frac{d(i_p(t_r))}{dt} = \frac{1}{2\gamma_1(t_r)(R_s(t_r)n^2 + R_L)} \left[s_1(t_r) (i_p(t_r)(1 + \gamma_1(t_r))(R_s(t_r)n^2 + R_L) + 2R_L i_p(t_r)) - s_2(t_r) (i_p(t_r)(1 - \gamma_1(t_r))(R_s(t_r)n^2 + R_L) + 2R_L i_p(t_r)) \right] \quad \text{A36.}$$

A.1.3 Resistive Load with Stray Inductance After FCG Operation

Equation (67) of Chapter 4 defined the stray inductance as a factor x multiplied by the primary leakage inductance, so the amount of stray inductance can be analyzed in terms of a factor increase above the primary leakage inductance. Substituting the new term of equation (67) into equation A32 for the primary current with an HPM load, simplifying, and taking the inverse Laplace transform results in equation A37. Equation A37 is a

modified version of equation A33. The symbols s_3 , s_4 , and γ_2 are now modified versions of the previous definitions.

$$i_p(t) = \frac{1}{2\gamma_2} \left[\left(I_{po}(1 + \gamma_2) + \frac{2R_L(I_{po}(1 - k)(1 + x) + kI_{mo})}{R_s n^2 + R_L(1 + x(1 - k))} \right) e^{s_3(t-t_r)} - \left(I_{po}(1 - \gamma_2) + \frac{2R_L(I_{po}(1 - k)(1 + x) + kI_{mo})}{R_s n^2 + R_L(1 + x(1 - k))} \right) e^{s_4(t-t_r)} \right] \quad \text{A37.}$$

$$s_3 = -\frac{R_s n^2 + R_L(1 + x(1 - k))}{2L_s(1 - k)(1 + x + k)}(1 + \gamma_2) \quad \text{A38.}$$

$$s_4 = -\frac{R_s n^2 + R_L(1 + x(1 - k))}{2L_s(1 - k)(1 + x + k)}(1 - \gamma_2) \quad \text{A39.}$$

$$\gamma_2 = \sqrt{1 - \frac{4R_L(1 - k)(1 + x + k)}{R_s n^2 \left(1 + \frac{R_L}{R_s n^2} (1 + x(1 - k)) \right)^2}} \quad \text{A40.}$$

The derivative of the primary current can then be computed as the following.

$$\frac{d(i_p(t_r))}{dt} = \frac{1}{2\gamma_2(t_r)} \left[s_3(t_r) \left(i_p(t_r)(1 + \gamma_2(t_r)) + \frac{2R_L(i_p(t_r)(1 - k)(1 + x) + ki_m(t_r))}{R_s(t_r)n^2 + R_L(1 + x(1 - k))} \right) - s_4(t_r) \left(i_p(t_r)(1 - \gamma_2(t_r)) + \frac{2R_L(i_p(t_r)(1 - k)(1 + x) + ki_m(t_r))}{R_s(t_r)n^2 + R_L(1 + x(1 - k))} \right) \right] \quad \text{A41.}$$

The secondary current with stray inductance is given by the following equation.

$$i_s(t) = \left(\frac{I_{so}(1 + \gamma_2)}{2\gamma_2} + \frac{kR_s n \left(I_{po} - \frac{(nI_{so})}{k} \right)}{(R_L(1 + x(1 - k)) + R_s n^2)\gamma_2} \right) e^{-\frac{R_L + n^2 R_s}{2L_s(1 - k^2)}(1 + \gamma_2)(t - t_r)} \quad \text{A42.}$$

$$- \left(\frac{I_{so}(1 - \gamma_2)}{2\gamma_2} + \frac{kR_s n \left(I_{po} - \frac{(nI_{so})}{k} \right)}{(R_L(1 + x(1 - k)) + R_s n^2)\gamma_2} \right) e^{-\frac{R_L + n^2 R_s}{2L_s(1 - k^2)}(1 - \gamma_2)(t - t_r)}$$

$$\frac{d(i_s(t_r))}{dt} = s_3(t_r) \left(\frac{i_s(t_r)(1 + \gamma_2(t_r))}{2\gamma_2(t_r)} + \frac{kR_s(t_r)n \left(i_p(t_r) - \frac{(ni_s(t_r))}{k} \right)}{(R_L(1 + x(1 - k)) + R_s(t_r)n^2)\gamma_2(t_r)} \right) \quad \text{A43.}$$

$$- s_4(t_r) \left(\frac{i_s(t_r)(1 - \gamma_2(t_r))}{2\gamma_2(t_r)} + \frac{kR_s(t_r)n \left(i_p(t_r) - \frac{(ni_s(t_r))}{k} \right)}{(R_L(1 + x(1 - k)) + R_s(t_r)n^2)\gamma_2(t_r)} \right)$$

A.2 Power Conditioning System with an RF Source

The power conditioning system with an RF source can be solved in all three stages of operation. However, as shown in this section, the full solutions are only available when ideal transformer coupling is assumed. Since numerical simulations with the RF source during FCG operation are not included in the thesis, the equations have been limited to times after FCG operation. The equations developed in this section were utilized for a numerical analysis on the optimal transformer turn ratio. These equations are valid until the secondary switch closes.

Figure 92 shows the circuit for s-domain analysis of an RF source after FCG operation. Again the current source representing the FCG or FCG simulator input is replaced with a short circuit. The voltage sources represent the initial conditions of currents through the inductors and voltage on the secondary capacitor. Performing KVL on the outer and right-hand loops results in equations A44 and A45.

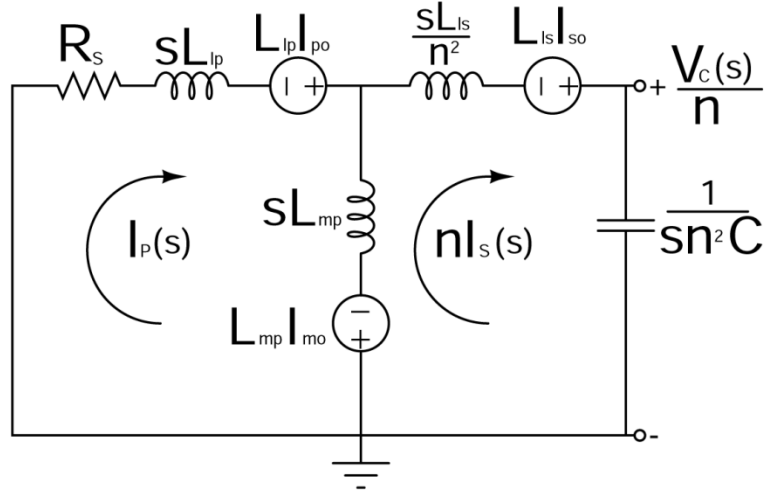


Figure 92. Equivalent s-domain circuit for an RF load after FCG operation

$$I_p(s)[R_s + sL_{lp}] - L_{lp}I_{po} + nI_s(s) \left[\frac{sL_{ls}}{n^2} + \frac{1}{sn^2C} \right] - \frac{L_{ls}(nI_{so})}{n^2} + \frac{V_{co}}{ns} = 0 \quad \text{A44.}$$

$$I_{mo}L_{mp} - sI_p(s)L_{mp} + nI_s(s) \left[sL_{mp} + \frac{sL_{ls}}{n^2} + \frac{1}{sn^2C} \right] - \frac{L_{ls}(nI_{so})}{n^2} + \frac{V_{co}}{ns} = 0 \quad A45.$$

Solving equation A45 for $I_p(s)$ and substituting into equation A44 will result in an equation with only $I_s(s)$ dependent on s . Multiplying both sides of the equation by s^2 and arranging terms of like order will result in equation A46.

$$\begin{aligned} nI_s(s) & \left[s^3 \left(\frac{L_{lp}L_{ls}}{n^2L_{mp}} + L_{lp} + \frac{L_{ls}}{n^2} \right) + s^2 \left(R_s + \frac{R_sL_{ls}}{n^2L_{mp}} \right) + s \left(\frac{L_{lp}}{L_{mp}n^2C} + \frac{1}{n^2C} \right) + \frac{R_s}{L_{mp}n^2C} \right] \\ & = s^2 \left(\frac{R_sL_{ls}L_{lp}(nI_{so})}{n^2L_{mp}} + \frac{L_{ls}(nI_{so})}{n^2} + L_{lp}(I_{mo} - I_{po}) \right) \\ & - s \left(I_{mo}R_s + \frac{R_sL_{ls}(nI_{so})}{n^2L_{mp}} + \frac{V_{co}L_{lp}}{nL_{mp}} + \frac{V_{co}}{n} \right) - \frac{V_{co}R_s}{nL_{mp}} \end{aligned} \quad A46.$$

Equation A46 can be simplified by putting all inductor terms in relation to L_s and collecting terms. The equation can then be solved for $nI_s(s)$.

$$\begin{aligned} nI_s(s) & = \frac{s^2 \left(L_s(1-k) \left[\frac{R_s(nI_{so})(1-k)}{k} + \frac{R_s(nI_{so}) + I_{mo} - I_{po}}{n^2} \right] \right)}{s^3 \left(\frac{L_s(1-k^2)}{n^2k} \right) + s^2 \left(\frac{R_s}{k} \right) + s \left(\frac{1}{kn^2C} \right) + \frac{R_s}{kL_sC}} \\ & + \frac{-s \left(I_{mo}R_s + \frac{R_s(1-k)(nI_{so})}{k} + \frac{V_{co}}{n} \left[\frac{(1-k)n^2}{k} + 1 \right] \right) - \frac{V_{co}R_s n}{kL_s}}{s^3 \left(\frac{L_s(1-k^2)}{n^2k} \right) + s^2 \left(\frac{R_s}{k} \right) + s \left(\frac{1}{kn^2C} \right) + \frac{R_s}{kL_sC}} \end{aligned} \quad A47.$$

With $nI_s(s)$ known according to equation A47, the voltage at the load can then be calculated.

$$\frac{V_c(s)}{n} = nI_s(s) \left(\frac{1}{sn^2C} \right) + \frac{V_{co}}{sn} \quad A48.$$

Substituting equation A47 into equation A48 allows one to solve for $V_c(s)$.

$$\begin{aligned} V_c(s) & = \frac{1}{s} \left[\frac{1}{nC} \left[\frac{s^2 \left(L_s(1-k) \left[\frac{R_s(nI_{so})(1-k)}{k} + \frac{R_s(nI_{so}) + I_{mo} - I_{po}}{n^2} \right] \right)}{s^3 \left(\frac{L_s(1-k^2)}{n^2k} \right) + s^2 \left(\frac{R_s}{k} \right) + s \left(\frac{1}{kn^2C} \right) + \frac{R_s}{kL_sC}} \right. \right. \\ & \left. \left. + \frac{-s \left(I_{mo}R_s + \frac{R_s(1-k)(nI_{so})}{k} + \frac{V_{co}}{n} \left[\frac{(1-k)n^2}{k} + 1 \right] \right) - \frac{V_{co}R_s n}{kL_s}}{s^3 \left(\frac{L_s(1-k^2)}{n^2k} \right) + s^2 \left(\frac{R_s}{k} \right) + s \left(\frac{1}{kn^2C} \right) + \frac{R_s}{kL_sC}} \right] + V_{co} \right] \end{aligned} \quad A49.$$

To solve for $v_c(t)$, the denominator of equation A49 should be factored and the inverse Laplace transform applied. However, the inverse Laplace transform of equation A49 is unknown. Therefore, a simplifying assumption must be made. When k is one, equation A49 simplifies to the following equation.

$$V_c(s) = \frac{1}{nC} \left[\frac{-s \left(I_{mo} R_s + \frac{V_{co}}{n} \right)}{s^2 R_s + s \left(\frac{1}{n^2 C} \right) + \frac{R_s}{L_s C}} + \frac{-\frac{V_{co} R_s n}{L_s}}{s \left(s^2 R_s + s \left(\frac{1}{n^2 C} \right) + \frac{R_s}{L_s C} \right)} \right] + \frac{V_{co}}{s} \quad A50.$$

The denominator of the first two terms can be factored with the following three equations.

$$s^2 R_s + s \left(\frac{1}{n^2 C} \right) + \frac{R_s}{L_s C} = (s - s_5)(s - s_6) \quad A51.$$

$$s_{5,6} = \frac{-1}{2R_s n^2 C} (1 \pm \beta) \quad A52.$$

$$\beta = \sqrt{1 - \frac{4R_s^2 n^4 C}{L_s}} \quad A53.$$

The inverse Laplace transform can then be solved for $v_c(t)$.

$$v_c(t) = \left(\frac{V_{co}(1 + \beta) + 2I_{mo}R_s n}{2\beta} \right) e^{\frac{-(1+\beta)}{2R_s n^2 C}(t-t_r)} - \left(\frac{V_{co}(1 - \beta) + 2I_{mo}R_s n}{2\beta} \right) e^{\frac{-(1-\beta)}{2R_s n^2 C}(t-t_r)} \quad A54.$$

The derivative of the capacitor voltage can be determined for any point with fully known circuit values as the following.

$$\frac{d(v_c(t_r))}{dt} = s_5(t_r) \left(\frac{v_c(t_r)(1 + \beta(t_r)) + 2i_m(t_r)R_s(t_r)n}{2\beta(t_r)} \right) - s_6(t_r) \left(\frac{v_c(t_r)(1 - \beta(t_r)) + 2i_m(t_r)R_s(t_r)n}{2\beta(t_r)} \right) \quad A55.$$

Since the assumption of ideal unity had to be made, the solution for $i_s(t)$ is unnecessary for numerical simulations of the RF load. The secondary current can, however, be obtained, as it is product of the load capacitance and the derivative of the load voltage.

$$i_s(t) = C \left[s_5 \left(\frac{V_{co}(1 + \beta) + 2I_{mo}R_s n}{2\beta} \right) e^{\frac{-(1+\beta)}{2R_s n^2 C}(t-t_r)} - s_6 \left(\frac{V_{co}(1 - \beta) + 2I_{mo}R_s n}{2\beta} \right) e^{\frac{-(1-\beta)}{2R_s n^2 C}(t-t_r)} \right] \quad A56.$$

The derivative of the secondary current can then be found by the following equation.

$$\frac{d(i_s(t_r))}{dt} = C \left[s_5^2(t_r) \left(\frac{v_c(t_r)(1 + \beta(t_r)) + 2i_m(t_r)R_s(t_r)n}{2\beta(t_r)} \right) - s_6^2(t_r) \left(\frac{v_c(t_r)(1 - \beta(t_r)) + 2i_m(t_r)R_s(t_r)n}{2\beta(t_r)} \right) \right] \quad A57.$$

Since the differential equations in this analysis of an RF load were only solved for the second order case, when $k=1$, the assumption of a unity coupling factor will hold for finding the primary current. The current can be found by equation A58. Equation A58 is obtained by the isolation of $i_p(t)$ through KVL around the outer circuit loop of the time-domain equivalent of Figure 92 with ideal coupling.

$$i_p(t) = \frac{-v_c(t)}{R_s n} \quad A58.$$

Substituting equation A54 for $v_c(t)$ results in equation A59.

$$i_p(t) = \left(\frac{V_{co}(1 - \beta) + 2I_{mo}R_s n}{2\beta R_s n} \right) e^{\frac{-(1-\beta)}{2R_s n^2 C}(t-t_r)} - \left(\frac{V_{co}(1 + \beta) + 2I_{mo}R_s n}{2\beta R_s n} \right) e^{\frac{-(1+\beta)}{2R_s n^2 C}(t-t_r)} \quad A59.$$

Again, the derivative of the primary current with the time terms equal to zero can be used for numerical analyses with a dynamic fuse resistance.

$$\begin{aligned} \frac{d(i_p(t_r))}{dt} = & s_5(t_r) \left(\frac{v_c(t_r)(1 - \beta(t_r)) + 2i_m(t_r)R_s(t_r)n}{2\beta(t_r)R_s(t_r)n} \right) \\ & - s_6(t_r) \left(\frac{v_c(t_r)(1 + \beta(t_r)) + 2i_m(t_r)R_s(t_r)n}{2\beta(t_r)R_s(t_r)n} \right) \end{aligned} \quad \text{A60.}$$

These equations are valid up until the capacitor voltage reaches its peak value. At this point, the output switch of Figure 1 closes to create an underdamped oscillator with the high voltage capacitor and shunt inductance.

References for Appendix A

- [1] P. W. Smith, *Transient Electronics: Pulsed Circuit Technology*. West Sussex, England: Wiley, 2002.
- [2] A. A. Neuber, "Explosively Driven Pulsed Power," Berlin: Springer-Verlag, 2005.
- [3] G. V. Lago and D. L. Waidelich, *Transients in Electrical Circuits*. New York, NY: The Ronald Press Company, 1958.
- [4] X. Gang (Access Confirmed Nov. 2008). Fourier-Laplace. [Online]. Available: http://wims.unice.fr/wims/en_tool~analysis~fourierlaplace.en.html.
- [5] R. E. Reinovsky, I. R. Lindemuth, and J. E. Vorthman, "High voltage power condition systems powered by flux compression generators," in *Proc. 7th Pulsed Power Conference*, R. White and B. Bernstein, Eds. Monterey, CA, 1989.

APPENDIX B: Computer Code for Numerical Analyses

To implement the equations derived in Appendix A with a dynamic fuse resistance, numerical techniques are used. The circuit currents during FCG operation are determined by the equation describing the FCG output and the relative impedances of the circuit paths, as derived in Appendix A. The circuit voltages, the integral of current action, the fuse resistance, component power dissipation, and component energy dissipation can all be determined from knowledge of the circuit currents, derivatives of the currents, and time history of the currents along with the component parameters. The fuse resistance is calculated at each time step during the simulation based upon the computed integral of current action up to that time and the fuse resistivity equations of Chapter 4.

After FCG operation, the circuit currents are found by applying the equations derived in Appendix A. Since the circuit equations are derived for the general case with initial conditions for all inductances and capacitances, knowledge of the circuit currents, fuse resistance, and capacitor voltage, when applicable, at any time can be used to determine the circuit parameters at the next time step. The derivatives of the circuit currents can thus be calculated with the time term, $t-t_r$, equal to zero. The time term of the equations for the current derivatives can be set equal to zero at each point in the simulation since the circuit is completely described at each time step. The circuit values at any time in the simulation can be considered the initial conditions for a new transient response with that time set to zero. With the current derivatives calculated, the new current values can be calculated by calculating the current change in a very small time step. The new current values and the change in current can be used to calculate new circuit voltages, the new integral of current action, the new fuse resistance, and new component power and energy

dissipation at the new time step. Thus the circuit is completely described at the new time, and the process can repeat through the end of the simulation.

This numerical analysis technique can be used with great accuracy. A check of energy conservation is performed for each time step to ensure accuracy. A time step of 0.5 ns is most often used. Longer time steps can be used to reduce simulation run time, but too long of a time step will result in a message reporting an energy conservation error. The MATLAB program will simulate the full system with a resistive load during and after FCG operation. The program will automatically output the peak load voltage, peak load power, and five plots of interest. The interested user of the program can obtain much more information from the program data than the automatically-produced output. Variations and extensions of this program are the foundation for many of the previously presented analyses.

Note: If the program is copied and pasted from an electronic version of this document, the user must ensure that the ellipsis (...) at the end of some statements is formed by three periods and not automatically converted to the ASCII character formed by the hexadecimal number 2026.

Copyright statement: The program, as a part of the thesis, is the copyright of Kevin A. O'Connor. Use of the program by researchers is welcomed as long as credit for program authorship is appropriately noted.

```
%%%%%%%%%%%%%%%%%%%%%%%%%%%%%%%%%%%%%%%%%%%%%%%%%%%%%%%%%%  
% The following program is the copyright of Kevin A. O'Connor. Use of the program by researchers is  
% welcomed as long as credit for authorship is appropriately noted.  
%%%%%%%%%%%%%%%%%%%%%%%%%%%%%%%%%%%%%%%%%%%%%%%%%%%%%%%%%%  
% The program will execute in Matlab to simulate the power conditioning system with an HPM load.  
% The user-controlled inputs are the first section of 22 parameters and the fuse wire length, if minimum  
% length is inappropriate or undesired. Comments describe each.  
%%%%%%%%%%%%%%%%%%%%%%%%%%%%%%%%%%%%%%%%%%%%%%%%%%%%%%%%%%  
outputoptions= [1 1 1 1]; % Automatic plot selection: 1 for plot. 0 for no plot.  
% 1.Primary Current 2.Fuse Resistance 3.Load Voltage 4.Inductively-stored energy distribution
```

```

% after action limit 5. Cumulative fuse and load energy dissipation
Ip0=40000; % Peak primary current from FCG
Rl=18; % Load impedance [Ohm]
Lp=1E-6; % Transformer primary self-inductance
k=.8; % Transformer coupling factor. For ideal coupling, use k=.99
n=3; % Transformer turn ratio
x=0; % Coefficient for calculation of stray circuit inductance
tr=10E-6; % FCG operation run time [s]
tfinal=12E-6; % Time value for end of simulation [s]
tstep=.5E-9; % Time step for numerical calculations [s]
singlewirearea=4.87E-9; % Area of single fuse wire [m^2]
wiremassdensity=8690; % Wire mass density [kg/(m^3)]
initialwireresistivity=1.725E-8; % Room temperature wire resistivity [Ohm-m]
Esp1=1409000; % Specific energy at action limit [J/kg]
Esp2=5909000; % Specific energy at burst [J/kg]
fusebreakdownstrength=600000; % Breakdown level for fuse vapor [V/m]
f=.55; % Fraction of inductively-stored energy to be dissipated in fuse after action limit
A=23.9; % Fuse resistivity curve-fitting parameter
B=2.3; % Fuse resistivity curve-fitting parameter
C=118; % Fuse resistivity curve-fitting parameter
eps=1; % FCG output parameter
alpha=2.8E-9; % Fuse material parameter [(m^2)/A/(s^.5)]
%%%%%%%%%%%%%%%%%%%%%%%%%%%%%%%%%%%%%%%%%%%%%%%%%%%%%%%%%%%%%%%%%%%%%%%%
% The following values are not to be set by the user, with the exception of fuse wire length.
Ls=Lp*n*n;
cg=eps/tr;
Is0=((Ip0*k)/((exp(1)-1)*n))*(((1/(cg+(Rl/Ls)))*((cg*exp(eps))+((Rl/Ls)*exp(-Rl*tr/Ls)))-...
    exp(-Rl*tr/Ls)));
Im0=Ip0-(n*Is0);
Eise0c=(.5*Ip0*Ip0*(Lp*(1-k)*(1+x)))+(Im0*Im0*(Lp*(k)))+(n*Is0)^2*Lp*(1-k);
he(1,1)=((Ip0*Ip0*tr)/(eps*((exp(1)-1)^2)))*((.5*(exp(2*eps)))-(2*(exp(eps)))+2.5);
totalfusearea=alpha*(sqrt(he));
approxfusewires=round(totalfusearea/singlewirearea);
%%%%%%%%%%%%%%%%%%%%%%%%%%%%%%%%%%%%%%%%%%%%%%%%%%%%%%%%%%%%%%%%%%%%%%%%
% Fuse wire length can be increased by user if simulation of minimum length
% results in output saying arc breakdown is possible.
fusewirelength=f*Eise0c/(wiremassdensity*totalfusearea*(Esp2-Esp1)); % [m]
%%%%%%%%%%%%%%%%%%%%%%%%%%%%%%%%%%%%%%%%%%%%%%%%%%%%%%%%%%%%%%%%%%%%%%%%
R0=initialwireresistivity*fusewirelength/totalfusearea;
fusemass=wiremassdensity*fusewirelength*totalfusearea;
tinitial=0;
y1=(tr-tinitial)/tstep;
y2=((tfinal-tinitial)/tstep)+1;
z=0;
while z < (y2);
t(1,z+1)=tinitial+(tstep*z);
z=z+1;
end;
Rf(1,1)=R0;
Ip(1,1)=0;
Is(1,1)=0;
Im(1,1)=0;
Ip2(1,1)=0;
h(1,1)=0;
Vf(1,1)=0;
Pf(1,1)=0;

```

```

Ef(1,1)=0;
Vl(1,1)=0;
Pl(1,1)=0;
El(1,1)=0;
Eise(1,1)=0;
specificenergy(1,1)=0;
Econservedtest(1,1)=0;
i=2;
while t(1,i) <= tr;
Ip(1,i)=(Ip0/(exp(1)-1))*((exp(eps*t(1,i)/tr))-1);
Ip2(1,i)=Ip(1,i)*Ip(1,i);
Is(1,i)=(Ip0*k/(n*(exp(1)-1)))*((1/(cg+(Rl/Ls)))*((cg*exp(cg...
*t(1,i)))+(Rl/Ls)*exp(-t(1,i)*Rl/Ls)))-exp(-t(1,i)*Rl/Ls));
Im(1,i)=Ip(1,i)-(n*Is(1,i));
h(1,i)=h(1,i-1)+(Ip2(1,i-1)*tstep)+((.5*(Ip2(1,i)-Ip2(1,i-1))*tstep));
Rf(1,i)=R0*(1+(A*((h(1,i)/he)^B));
Vf(1,i)=Rf(1,i)*Ip(1,i);
Pf(1,i)=Vf(1,i)*Ip(1,i);
Ef(1,i)=Ef(1,i-1)+(Pf(1,i-1)*tstep)+((.5*(Pf(1,i)-Pf(1,i-1))*tstep));
Vl(1,i)=Rl*Is(1,i);
Pl(1,i)=Vl(1,i)*Is(1,i);
El(1,i)=El(1,i-1)+(Pl(1,i-1)*tstep)+((.5*(Pl(1,i)-Pl(1,i-1))*tstep));
Eise(1,i)=(.5*Ip(1,i)*Ip(1,i)*(Lp*(1-k)*(1+x)))+(.5*Im(1,i)...
*Im(1,i)*(Lp*(k)))+(Lp*(n*Is(1,i)^2)*Lp*(1-k));
Econservedtest(1,i)=0;
specificenergy(1,i)=specificenergy(1,i-1)+((Ef(1,i)-Ef(1,i-1))/fusemass);
i=i+1;
end;
i=i-1;
Effcgop=Ef(1,i);
Elfcgop=El(1,i);
Eise0=Eise(1,i);
E0=Eise0+Effcgop+Elfcgop;
p(1,i)=(Rl*((Ip(1,i)*(1-k)*(1+x)))+(k*Im(1,i)))/(Lp*n*n*(1-k)*(1+x+k));
g(1,i)=sqrt(1-((4*Rl*(1-k)*(1+x+k))/(Rf(1,i)*n*n*((1+(Rl/(n*n*Rf(1,i)))*(1+x*(1-...
k))))^2));
s1(1,i)=-(((Rl*(1+x*(1-k)))+(n*n*Rf(1,i)))/(2*Lp*n*n*(1-k)*(1+x+k)))*(1+g(1,i));
s2(1,i)=-(((Rl*(1+x*(1-k)))+(n*n*Rf(1,i)))/(2*Lp*n*n*(1-k)*(1+x+k)))*(1-g(1,i));
dipdt(1,i)=(1/(s1(1,i)-s2(1,i)))*((s1(1,i)*((Ip(1,i)*s1(1,i))+p(1,i)))-...
(s2(1,i)*((Ip(1,i)*s2(1,i))+p(1,i))));
disdt(1,i)=(s1(1,i)*(((Is(1,i)*(1+g(1,i)))/(2*g(1,i)))+(k*Rf(1,i)*n*(Ip(1,i)-...
(n*Is(1,i)/k)))/(g(1,i)*((Rl*(1+x*(1-k)))+(Rf(1,i)*n*n))))-(s2(1,i)*...
(((Is(1,i)*(1-g(1,i)))/(2*g(1,i)))+(k*Rf(1,i)*n*(Ip(1,i)-(n*Is(1,i)/k)))/...
(g(1,i)*((Rl*(1+x*(1-k)))+(Rf(1,i)*n*n)))));
i=i+1;
while i <= y2;
Ip(1,i)=Ip(1,i-1)+(tstep*dipdt(1,i-1));
Ip2(1,i)=Ip(1,i)*Ip(1,i);
Is(1,i)=Is(1,i-1)+(tstep*disdt(1,i-1));
Im(1,i)=Ip(1,i)-(n*Is(1,i));
h(1,i)=h(1,i-1)+(Ip2(1,i-1)*tstep)+((.5*(Ip2(1,i)-Ip2(1,i-1))*tstep));
if specificenergy(1,i-1) < Esp2;
Rf(1,i)=R0*(A+exp(((h(1,i)-he(1,1))/he(1,1))*C));
hburst=h(1,i);
elseif specificenergy(1,i-1) < ((2*Esp2)-Esp1);
Rf(1,i)=R0*(A+exp((hburst-he)/he*C))*exp((hburst-h(1,i))/he*C));

```

```

else;
Rf(1,i)=R0*A;
end;
Vf(1,i)=Rf(1,i)*Ip(1,i);
Pf(1,i)=Vf(1,i)*Ip(1,i);
Ef(1,i)=Ef(1,i-1)+(Pf(1,i-1)*tstep)+((.5*(Pf(1,i)-Pf(1,i-1))*tstep));
Vl(1,i)=Rl*Is(1,i);
Pl(1,i)=Vl(1,i)*Is(1,i);
El(1,i)=El(1,i-1)+(Pl(1,i-1)*tstep)+((.5*(Pl(1,i)-Pl(1,i-1))*tstep));
Eise(1,i)=(.5*Ip(1,i)*Ip(1,i)*(Lp*(1-k)*(1+x)))+(.5*Im(1,i)...
    *Im(1,i)*(Lp*(k)))+(.5*((n*Is(1,i))^2)*Lp*(1-k));
Econservedtest(1,i)=100*abs((Eise(1,i)+El(1,i)+Ef(1,i)-E0)/E0);
specificenergy(1,i)=specificenergy(1,i-1)+((Ef(1,i)-Ef(1,i-1))/fusemass);
p(1,i)=(Rl*((Ip(1,i)*(1-k)*(1+x))+k*Im(1,i)))/(Lp*n*n*(1-k)*(1+x+k));
g(1,i)=sqrt(1-((4*Rl*(1-k)*(1+x+k))/(Rf(1,i)*n*n*((1+(Rl/(n*n*Rf(1,i))))*(1+x*(1-...
    k))))^2));
s1(1,i)=-(((Rl*(1+x*(1-k)))+(n*n*Rf(1,i)))/(2*Lp*n*n*(1-k)*(1+x+k)))*(1+g(1,i));
s2(1,i)=-(((Rl*(1+x*(1-k)))+(n*n*Rf(1,i)))/(2*Lp*n*n*(1-k)*(1+x+k)))*(1-g(1,i));
dipdt(1,i)=(1/(s1(1,i)-s2(1,i)))*((s1(1,i)*((Ip(1,i)*s1(1,i))+p(1,i)))-...
    (s2(1,i)*((Ip(1,i)*s2(1,i))+p(1,i))));
disdt(1,i)=(s1(1,i)*(((Is(1,i)*(1+g(1,i)))/(2*g(1,i)))+((k*Rf(1,i)*n*(Ip(1,i)-...
    (n*Is(1,i)/k))/(g(1,i)*((Rl*(1+x*(1-k)))+(Rf(1,i)*n*n))))))-s2(1,i)*...
    (((Is(1,i)*(1-g(1,i)))/(2*g(1,i)))+((k*Rf(1,i)*n*(Ip(1,i)-(n*Is(1,i)/k))/...
    (g(1,i)*((Rl*(1+x*(1-k)))+(Rf(1,i)*n*n))))));
i=i+1;
end;
i=y1;
while i < y2;
if Econservedtest(1,i) < .5;
i=i+1;
else;
Attention='Program was changed such that energy was not conserved. Change time step or check variables.'
i=y2;
end;
end;
Vfmax=max(abs(Vf(1,1:floor(y2))));
if (Vfmax/fusewirelength) > fusebreakdownstrength;
Attention='Possible restrike due to high electric field prior to full vaporization. Consider lengthening fuse.'
end;
if specificenergy(1, floor(y2)) > (1.1*Esp2);
Attention='Possible restrike due to excessive specific energy. Consider lengthening fuse.'
end;
Rfmax=max(Rf);
Vlmax=max(abs(Vl));
Plmax=max(Pl);
FusePerEConsumedFinal(1,1)=Ef(1, floor(y2))/E0*100;
IsePerEStoredFinal(1,1)=100*Eise(1, floor(y2))/E0;
LoadPerEConsumedFinal(1,1)=100*El(1, floor(y2))/E0;
sprintf('Peak load voltage is %.1f kV. \n Peak load power is %.1f MW.', Vlmax/1000, Plmax/1E6)
if outputoptions (1,1) == 1;
plot(t*1E6, Ip/1000, 'k');
xlabel('Time (\mus)');
ylabel('Fuse Current (kA)');
end;
if outputoptions (1,2) == 1;
figure;

```

```

plot(t*1E6,Rf,'k');
xlabel('Time (\mus)');
ylabel('Fuse Resistance (\Omega)');
end;
if outputoptions (1,3) == 1;
figure;
plot(t*1E6,Vl/1000,'k');
xlabel('Time (\mus)');
ylabel('Load Voltage (kV)');
end;
if outputoptions (1,4) == 1;
figure;
plot(t*1E6,(El-El(1,floor(y1)))/Eise0,'k--',t*1E6,(Ef-Ef(1,floor(y1)))/Eise0,'k:',t*1E6,Eise/Eise0,'k');
axis([tr*1E6, tfinal*1E6, 0, 1])
xlabel('Time (\mus)');
ylabel('Normalized Transfer ofInductively-Stored Energy After Action Limit');
legend('Load', 'Fuse', 'Inductors');
end;
if outputoptions (1,5) == 1;
figure;
plot(t*1E6,El,'k--',t*1E6,Ef,'k:');
xlabel('Time (\mus)');
ylabel('Cumulative Energy Dissipated in Fuse and Load (J)');
legend('Load', 'Fuse',2);
end;
%%%%%%%%%%%%%%%%%%%%%%%%%%%%%%%%%%%%%%%%%%%%%%%%%%%%%%%%%%%%%%%%%%%%%%%%

```